Author:
Hofer, Stefan

Title:
Clouds over Greenland

The influence of clouds on contemporary and future Greenland Ice Sheet surface melt

Clouds over Greenland: The influence of clouds on contemporary and future Greenland Ice Sheet surface melt

University of Bristol

School of Geographical Sciences

Stefan Hofer

A dissertation submitted to the University of Bristol in accordance with the requirements of the degree of DOCTOR OF PHILOSOPHY in the Faculty of Science.

January 29, 2020

Word Count: 45000

Abstract

The Greenland Ice Sheet (GrIS) has become the largest single mass contributor to global sea level. Since the mid-1990s the mass loss has been accelerating. The current consensus on the main drivers behind the shift in Greenland climate dynamics are: (1) A state change of the North Atlantic Oscillation towards an anticyclonic phase, (2) an above average temperature increase due to Arctic amplification and (3) an increase in absorbed shortwave radiation due to the melt-albedo feedback.

However, thus far very few studies attempted to partition the GrIS surface energy budget (SEB) to find the main energy source behind the observed increase in surface melt. Furthermore, little is known about how much clouds have and will contribute to the recent and projected future GrIS melt increase.

In this thesis we find, that downwelling solar radiation has been the main driver of the recent changes in the SEB over the GrIS. Furthermore, we establish a connection between the observed increase in high-pressure frequency, an unreported reduction in summer cloud cover and the recent mass loss acceleration over the GrIS. Additionally, we also show that cloud microphysics are the leading source of uncertainties in future projections of GrIS melt. Our analysis suggests that differences in cloud water phase distribution can add similar or larger uncertainties to projected Greenland melt than the choice of greenhous gas emission scenario.

Because our analysis identifies a great sensitivity of the GrIS to cloud conditions, we mark three key areas to increase our ability to model the Greenland sea level rise contribution: (1) Increasing the amount of cloud (microphysical) observations in the Arctic. (2) Improving the representation of clouds in (regional) climate models. (3) Considering the dynamic nature of the Greenland cloud radiative effect and its transient response in a warming climate.

Author's Declaration

Acknowledgments

This thesis is dedicated to my parents and my partner Marianne, for their love, support, encouragement... and especially their patience.

The joy of my 3.5 years at the University of Bristol has also been greatly influenced by the wonderful new friends I've made.

Amy, thanks for explaining the complex British Mail service to me in a way that even I could follow. Guillaume, thanks for sharing your amazing barrista skills with me. Coffee is what has kept me going. Tim, thanks for supporting me in the aftermath of my first full English breakfast. Mike, thanks for never getting bored talking sourdough and fermentation. Andrew, thanks for giving me the opportunity to witness a "hurricane" on the Greenland Ice Sheet. Nina, thanks for always laughing at my "jokes". Laurence, thanks for selecting me for the famous "Athletico Geography" midfield, even when my first touch could often be described as slightly "heavy". Claire, thanks for always chatting about skiing with me when I missed the snow. Chris W., thanks for introducing me to the "British way" of rock climbing. Jon H., thanks for your "friendly reminders" and for letting me join the Camp Doom expedition.
Martyn, thanks for believing in my abilities as a researcher and for letting me taste your famous but rather spicy field work cuisine.
Jonathan, thanks for giving me the chance to prove myself as a researcher and for your guidance throughout the last 3.5 years.

My PhD would not have been half as enjoyable without you. I hope that our paths will cross again.

Contents

List of Figures

List of Tables

Chapter 1

Context and research objectives

The Greenland Ice Sheet (GrIS), which contains ice mass equivalent to 7.4 m of potential global sea level rise (Morlighem et al. 2017), has been undergoing significant changes since the mid-1990s. During most of the 20th century, the GrIS was stable, and a positive surface mass balance (SMB) was offset by calving of ice into the ocean ("ice discharge") (Van den Broeke et al. 2016). However, since the mid-1990s the GrIS has started to lose mass (Enderlin et al. 2014; Mouginot et al. 2019; Van den Broeke et al. 2016; Rignot et al. 2011). This shift in GrIS climate dynamics has been attributed to a state change of the large-scale atmospheric circulation over Greenland during the melt season (JJA), leading to persistent anticyclonic conditions and more frequent warm-air advection (Hanna et al. 2016; Hanna et al. 2018; Fettweis et al. 2013a). Therefore, the Greenland Ice Sheet is now considered to be out of equilibrium.

The Greenland Ice Sheet is not only losing mass, but the mass loss is also accelerating (Rignot et al. 2011; Wouters et al. 2013; Enderlin et al. 2014; Van den Broeke et al. 2016). Depending on the methodological approach, the reference period used and the length of the observational data, the GrIS mass loss is accelerating at a pace between 16.8 ± 2.8 Gt/yr^2 (Van den Broeke et al. (2016)), 21.9 ± 9 Gt/yr^2 (Rignot et al. (2011)), 25 ± 9 Gt/yr^2 (Wouters et al. (2013)) and 27 ± 9.0 Gt/yr^2 (Enderlin et al. (2014)). Mouginot et al. (2019) find a total mass loss of 286 ± 20 Gt/yr (2010-2018), while Van den Broeke et al. (2016) report a 2003-2014 average mass loss of 270 ± 4 Gt/yr using the Gravity Recovery and Climate Experiment dataset (GRACE) and 294 ± 5 Gt/yr from the mass budget method. The recent increase in mass loss from the GrIS since 1991 has been dominated by decreasing surface mass balance and increasing meltwater runoff into the ocean (Van den Broeke et al. 2016). Roughly 60% of GrIS mass loss has come from these surface mass balance anomalies between 1991-2015, while ice discharge into the ocean has contributed around 40% (Van den Broeke et al. 2016). Between 2009 and 2012, an even greater share of 68% of the mass balance anomalies were due to a reduction in surface mass balance (Enderlin et al. 2014). However, Mouginot et al.

(2019) find that between 1972 and 2018 (the whole Landsat observational time series), ice discharge has dominated the cumulative mass anomalies. By using the mass budget method, Mouginot et al. (2019) find that $66 \pm 8\%$ of the long-term mass balance anomalies are due to iceberg calving, twice as much as the $34 \pm 8\%$ from the surface mass balance. Therefore, surface mass loss has only become the dominant contributor to GrIS total mass loss during the last two decades.

Partitioning the recent surface mass balance anomalies shows that an increase in surface melt is the main contributing factor to GrIS mass loss (Van den Broeke et al. 2016; Van den Broeke et al. 2017). However, exact quantifications of which part of the energy budget has contributed the greatest share to the recent melt increase are sparse. The most widely used explanation is that a temperature increase is the main cause of surface melt anomalies (Box et al. 2012; Van den Broeke et al. 2017; Hanna et al. 2012), enhancing the melt albedo feedback (Box et al. 2012). However, if increased temperature were the main cause of the recent melt increase, then the surface energy budget changes would be dominated by an increase in downwelling longwave (infrared) radiation. Conversely, over the ablation zone, where most of the GrIS surface melt occurs, observational studies clearly show that absorbed solar radiation is the primary source of melt variability (Van de Wal et al. 2005; Van den Broeke et al. 2011). Therefore, there is a slight contradiction in the argument of what part of the surface energy budget is the most important driver of changes in the surface melt dynamics of the Greenland Ice Sheet.

Furthermore, Box et al. (2012) find, using a regional climate model and albedo remote sensing data, that there is a clear signal of increasing downwelling solar radiation partly driving the melt-albedo feedback. Spatially, the signal of increased solar radiation is particularly pronounced over the NW and SW parts of the GrIS. That increasing solar radiation might drive the GrIS melt is contradictory to the statement that Greenland melt is driven by higher temperatures alone (e.g. Tedesco et al. 2011; Van den Broeke et al. 2017).

Additionally, the only way in which the downwelling solar radiation can increase over decadal time scales is an increase in atmospheric transmissivity. Furthermore, the amount solar energy transmitted through the troposphere is mainly controlled by the cloud amount and cloud optical thickness (Bintanja et al. 1996). Clouds have been shown to be highly important drivers of the climate sensitivity in a global context (Tan et al. 2016; Tan et al. 2019), mainly because they strongly modulate the surface energy budget. Conversely, the role of clouds in the Greenland Ice Sheet melt acceleration has not been investigated in great detail, despite significant advances in high-resolution GrIS climate models over the last decades (Delhasse et al. 2018; Noël et al. 2018; Fettweis et al. 2017). Together with more than 30 yrs. of satellite remote sensing data of clouds over Greenland by polar orbiting satellites, our ability to monitor and model the Arctic now make it possible to directly address these gaps in knowledge about what is driving the surface energy budget changes over the Greenland

Ice Sheet. (Noël et al. 2018; Fettweis et al. 2017).

In summary, this thesis aims to advance our understanding of how regional climate models can be used to study the impact of clouds on GrIS melt. While it will briefly describe the current literature on the overall mass balance of the Greenland Ice Sheet, it will otherwise only address processes relevant to the surface melt and surface mass balance dynamics. Additionally, it will also particularly focus on how clouds have influenced recent Greenland melt increases by amending the surface energy budget and how cloud microphysics can explain significant parts of uncertainties in future GrIS melt projections.

1.1 About this thesis

Overarching research objective: To constrain the contemporary and future impact of cloud dynamics upon recent Greenland Ice Sheet melt. Validation of a regional climate model (MAR) to study the impacts of clouds on the Greenland surface energy budget and meltwater production, using satellite remote sensing data (AVHRR, MODIS), in-situ observations (PROMICE) and a second regional climate model (RACMO) as reference tools.

1.1.1 A validation of clouds and radiation in two state-of-the-art regional climate models

Research objective 1: To validate two commonly used regional climate models (MAR, RACMO) against in-situ radiation observations and satellite remote sensing data of clouds over the entire Greenland Ice Sheet.

The first results chapter, entitled "A validation of radiative fluxes and clouds in two state-of-the-art regional climate models over the Greenland Ice Sheet", tries to establish the skills and shortcomings of two regional climate models when modelling the surface enery budget and clouds over the GrIS. The comparison with 23 weather stations reporting shortwave and longwave radiation shows that polar regional climate models have significant biases of up to 10 W/m^2 when compared to the measured absolute values of daily observations. However, when looking at temporal changes then both regional climate models simulate very similar anomalies in the surface energy budget over the last 20 years. Additionally, the two regional climate models are also able to accurately reproduce temporal trends in cloud cover compared to satellite observations.

1.1.2 Decreasing cloud cover drives the recent mass loss on the Greenland Ice Sheet

Research objective 2: To analyse the influence of recent circulation anomalies upon melt season cloud cover trends. Furthermore, this chapter will quantify the impact of the recent decrease in melt season cloud cover on the surface energy budget of the Greenland Ice Sheet and how much energy the increase in downwelling shortwave radiation has contributed to the recently accelerating mass loss and surface melt over Greenland.

The second results chapter, entitled "Decreasing cloud cover drives the recent mass loss on the Greenland Ice Sheet" focuses on the impact of recent anticyclonic circulation anomalies on cloud cover reductions and subsequent changes in the radiation budget at the surface of the GrIS (Hofer et al. 2017). It establishes a direct link between reductions in cloud cover of more than 10% since the mid-1990s over the southern GrIS, an increase in downwelling solar radiation and significant increases in melt over the low albedo ablation zone. Furthermore, our results show that despite GrIS wide increases in atmospheric temperature during a period of sustained global warming and Arctic amplification, downwelling longwave fluxes have contributed less to the increases in the surface energy budget of the GrIS than downwelling shortwave fluxes due to cloud cover reductions (Hofer et al. 2017).

1.1.3 Cloud microphysics and circulation anomalies control differences in future Greenland melt

Research objective 3: To analyse uncertainties in high-emission future projections of Greenland Ice Sheet melt. We will especially focus on the role of differences in cloud microphysics, cloud liquid water path and optical thickness, to explore the divergence in 21st century melt projections due to differences in atmospheric longwave emissivity.

The third and last results chapter, entitled "Cloud microphysics and circulation anomalies control differences in future Greenland Ice Sheet melt", focuses on the role that cloud microphsics play in uncertainties in future GrIS sea level contribution (Hofer et al. 2019). It also addresses how uncertainties due to cloud microphysics compare to uncertainties due to potentially missing circulation anomalies. We demonstrate that discrepancies in modelled cloud optical thickness and cloud water phase can double the differences in 21st centure GrIS sea level contribution within the high-emission scenario RCP8.5 (Hofer et al. 2019). Furthermore, we highlight that the uncertainties due to cloud microphysics, as well as differences due to synoptic scale atmospheric circulation are very sensitive to the amount of future GrIS warming (Hofer et al. 2019). In the current climate, anticyclonic circulation, as observed over the last two decades, is more efficient at enhancing GrIS melt. However,

in a +2°C warmer climate, differences in cloud microphysical properties have a greater impact on GrIS melt than uncertainties connected to the synoptic-scale circulation (Hofer et al. 2019).

1.1.4 Thesis structure

This thesis especially focuses on the contribution of clouds to the recent increase in surface melt over the Greenland Ice Sheet. Its focus lies entirely on processes that occur at the surface of the Greenland Ice Sheet, namely the influence of clouds on the (1) surface energy budget, (2) surface melt and (3) on the resulting reduction in the Greenland Ice Sheet surface mass balance. Temporally, there are two focal points: (a) the influence of clouds on the contemporary increase in Greenland melt and (b) the impact of differences in cloud microphysics upon uncertainties in future Greenland melt projections.

Chapter 2 provides an in-depth review of the literature concerned with the Greenland Ice Sheet climate system. It synthesizes the broader literature about the magnitude of mass loss from the Greenland Ice Sheet and its underlying causes. Chapter 3 introduces the concept of downscaling within polar regional climate models, but also highlights the importance and development of in-situ and satellite observations of Greenland.

The three results chapters, chapters 4, 5 and 6 explore in detail the research questions briefly outlined above. Chapter 7 presents a short summary of the main findings and discusses their importance within the current Greenland climate research focal points. Furthermore, chapter 7 also outlines potential cloud related future research incentives which could directly increase the accuracy of future projections of the Greenland Ice Sheet sea level contribution.

1.2 Publications

- Hofer, S., Tedstone, A. J., Fettweis, X., & Bamber, J. L. (2017). Decreasing cloud cover drives the recent mass loss on the Greenland Ice Sheet. Science Advances, 3(6), e1700584.
- Hofer, S., Tedstone, A. J., Fettweis, X., & Bamber, J. L. (2019). Cloud microphysics and circulation anomalies control differences in future Greenland melt. Nature Climate Change, 9(7), 523.

Chapter 2

Background

2.1 Preface

This section will highlight the most important background information from the Greenland Ice Sheet literature. We will explore the state-of-the-art in scientific knowledge, starting with the contemporary state of the Greenland Ice Sheet mass balance and surface mass balance. Additionally, this chapter will show that the underlying climatological causes of the recent acceleration of the Greenland Ice Sheet melt are less well understood than the overall magnitude of the recent mass imbalance. This background chapter will show, that previous to this dissertation, the surface energy budget has not been partitioned into its contributing components, leaving a gap in knowledge about the external drivers of the Greenland Ice Sheet surface melt and decrease in surface mass balance. Therefore, this chapter will provide the starting point to explore the Greenland Ice Sheet surface energy budget and its connection to clouds in more detail in the three results chapters of this thesis.

2.2 Components of ice sheet mass balance

2.2.1 Mass balance

To describe the changes in the physical state of Greenland Ice Sheet, especially changes in its overall mass, we need to consider four different budgets. First, the mass balance (MB, Eq.(2.1)) of an ice sheet is described by the temporal changes in its total mass. Physically, the mass balance is obtained by taking the difference between the surface mass balance (SMB) and the ice discharge into the ocean (D) of marine terminating glaciers (Van den Broeke et al. 2017). The surface mass balance is defined by the accumulation of snow, minus all

the mass sinks such as meltwater runoff and the sublimation of snow and ice particles. Ice discharge into the ocean is mainly controlled by iceberg calving at the terminus of the outlet glaciers (Howat et al. 2007).

Overall, there are three different approaches being used in the literature to constrain the mass balance of polar ice sheets, (i) the mass budget method or input-output method (i.e. the difference between the surface mass balance and the grounding line fluxes), (ii) quantifying changes in ice volume using remote sensing altimetry data and (iii) and quantifying time-variable changes in the gravitational acceleration using the GRACE remote sensing data (Hanna et al. 2013; Enderlin et al. 2014; Van den Broeke et al. 2016; Mouginot et al. 2019), where differences in the gravitational pull of the Earth due to the redistribution of mass (e.g. meltwater runoff from the Greenland Ice Sheet into the ocean) can be inferred by precisely measuring the distance between two satellites, roughly 220 km apart (Wahr et al. 2006).

$$MB = \frac{dM}{dt} = SMB - D \quad [Gt/yr] \tag{2.1}$$

2.2.2 Surface mass balance

The surface mass balance of glaciers and ice sheets is defined as the difference between all the water input at the surface (i.e. solid and liquid precipitation) and the combined surface mass loss terms (Fettweis et al. 2013a; Fettweis et al. 2017; Noël et al. 2018). On the left side of equation (2.2) is the total surface mass balance of the ice sheet. The only factor that is contributing mass to a given body of ice is the precipitation (P). Conversely, sublimation (SU), erosion of snow by the wind (ER) and meltwater runoff (RU) are decreasing the overall SMB. In this work the term precipitation refers to the deposition of solid or liquid hydrometeors onto the GrIS surface, sublimation refers to mass loss due to ice particles changing their phase from solid to gaseous, at the surface or when suspended in the air (Van den Broeke et al. 2017). This process requires 2838 kJ/kg of energy to break up the bonds between the ice molecules (Datt 2011), mostly coming from downwelling energy fluxes or by extracting heat from the environment and therefore cooling the near surface ice or atmosphere. A net erosion of snow by the wind (ER) is achieved when the divergence of the drifting snow vector field is greater than zero (Schmidt 1982).

While multiple remote sensing datasets can be combined to yield a value of the total mass balance of ice sheets using changes in ice volume or of gravitational potential (Eq.(2.1)), the mass budget method requires input from a regional climate model to constrain the SMB in equation (2.1) (Mouginot et al. 2019; Fettweis et al. 2013a; Fettweis et al. 2017; Noël et al. 2018). Furthermore, the individual magnitude of each SMB term in equation (2.2) is hard to constrain using satellite remote sensing data. Therefore, polar regional climate models are extensively used as a tool to dynamically downscale reanalysis datasets or future

projections over the GrIS to obtain 2-D maps of the SMB and its components (Fettweis 2007; Noël et al. 2018; Box et al. 2012; Fettweis et al. 2013a; Fettweis et al. 2017; Franco et al. 2013).

$$SMB = P - SU - ER - RU \quad [Gt/yr] \tag{2.2}$$

2.2.3 Liquid water balance

Furthermore, to obtain the runoff (RU) term in the SMB equation (2.2) we need to constrain the terms of the liquid water balance (Eq.(2.3)). Sources of liquid water are rain (RA), aggregation of liquid water particles at the ice sheet surface (condensation, CO) and melt-water production (ME) due to a positive net energy input towards the ice surface. Hereby, the heat input (heat of fusion) required for melting the equivalent of 1 kg of ice at 0°C is $H_f = 333.55\ kJ/kg$. Sinks of liquid water in the liquid water balance are the retention of water within porous ice, snow or firn (RT) and the refreezing of water either at the surface of the ice sheet or within the snow or ice. Refreezing of liquid water releases the latent heat of fusion of $H_f = 333.55\ kJ/kg$ towards the snowpack, and therefore has the potential to transport heat from the surface to deep within the firn/snow or ice.

$$RU = RA + CO + ME - RT - RF \qquad [Gt/yr] \tag{2.3}$$

2.2.4 Surface energy budget

Out of all the terms of equations (2.1)-(2.3) sublimation (SU), runoff (RU) and melt (ME) depend strongly on the surface energy budget (SEB, Eq.(2.4)), but also the fraction of melt-water that refreezes (RF) at the ice sheet surface. The SEB determines the amount of energy that is available for melt (M in eq.(2.4)), warming of the surface (SEB $>$ 0 but T $<$ 0°C) or that is lost during periods of low energy input (SEB $<$ 0) leading to surface and as a further consequence near-atmospheric cooling. The SEB is the sum of all energy fluxes towards the surface (defined as positive fluxes in this study) and away from the surface (negative).

The SEB can be further divided into radiative and non-radiative energy fluxes, with a further division based on the spectrum of the radiation into shortwave (SW) and longwave (LW) fluxes. The net shortwave radiation is defined as the absorbed fraction of the incident solar fluxes at the surface ($SWD \cdot (1-\alpha)$), directly determined by the atmospheric transmissivity and the surface albedo (α). In the longwave part of the spectrum the surface is usually approximated as a black body, in which case the surface emissivity, ϵ, is set to unity and the outgoing longwave radiation becomes a function of the surface temperature only ($\epsilon \cdot \sigma \cdot T^4 = \sigma \cdot T^4$). For outgoing longwave radiation (LWU), σ refers to the Stefan-Boltzmann

constant $\sigma = 5.67 \cdot 10^{-8} \quad Wm^{-2}K^{-4}$. The non-radiative energy fluxes towards the surface are determined by the sensible (turbulent) heat flux (SHF), latent heat flux (LHF) and the sub-surface heat flux (G_s). The SHF is directly proportional to the near-surface temperature gradient and the atmospheric turbulence, while the LHF refers to energy losses or gains through to phase changes of water at the ice sheet surface.

$$\begin{aligned} M &= SWD - SWU + LWD - LWU + SHF + LHF + G_s \quad [W/m^2] \\ M &= SWD \cdot (1-\alpha) + LWD - \epsilon \cdot \sigma \cdot T^4 + SHF + LHF + G_s \quad [W/m^2] \end{aligned} \tag{2.4}$$

2.3 The state of the Greenland Ice Sheet

2.3.1 Recent changes in the GrIS mass balance

The Greenland Ice Sheet is undergoing significant changes. Over the last five decades, the GrIS has been losing mass equivalent to 13.7±1.1 mm of global sea level rise (Mouginot et al. 2019), confirmed in principle by other independent studies (Hanna et al. 2013; Enderlin et al. 2014). The GrIS is now the largest single mass contributor to global sea level, with a peak contribution of 1.2 mm in 2012 alone (Van den Broeke et al. 2016). Sustained and rapid increases in the near surface temperature of the GrIS have been identified as the main source of this increase in surface melt and ice discharge into the ocean. The recent temperature rise since the early 1990s is greatest in winter (up to ≈5°C), but also during summer there has been a significant surge in GrIS temperature of ≈2°C, named as the primary source of recent runoff and mass balance anomalies (Van den Broeke et al. 2017; Box et al. 2012; Hanna et al. 2012). However, so far only very limited analysis exists wkether the main driver of the surface energy budget is in fact temperature driven (i.e. downwelling longwave radiation) or also due to changes in other parts of the spectrum (i.e. downwelling solar radiation).

The GrIS has been losing mass since the 1990s, however the exact quantification remains closely linked to the reference period used, the length of the observational data and the scientific method (Mouginot et al. 2019). The latest estimate from Mouginot et al. (2019) with longest available time series suggests that Greenland is currently losing 286 ± 20 Gt/yr (2010-2018). Other studies find similar magnitudes of GrIS mass imbalance; Van den Broeke et al. (2016) estimate a mass loss (2003-2014) of 294±5 Gt/yr from the mass budget method and 270 ± 4 Gt/yr using the Gravity Recovery and Climate Experiment (GRACE) data, while Enderlin et al. (2014) find an average mass loss of 227 ± 25 (2000-2012).

There is also a consensus in the current literature that the GrIS has been experiencing an acceleration of mass loss. However, the exact values vary as well, based on the data length, reference period and methodological approach. Rignot et al. (2011) estimate an accelerating mass loss at a rate of 21.9 ± 1 Gt/yr^2 (1992-2010, mass budget method (MB) + GRACE),

Wouters et al. (2013) at 25 ± 9 Gt/yr^2 (2003-2012, GRACE), Enderlin et al. (2014) at 27.0 ± 9.0 Gt/yr^2 (2000-2012, MB) and at an accelerating rate of 16.8 ± 2.8 Gt/yr^2 by Van den Broeke et al. (2016) (1991-2015, MB + GRACE). However, Wouters et al. (2013) find that in order to be able to constrain mass loss acceleration within ±10 Gt/yr^2 from GRACE remote sensing data the observational period would need to span 20 years or more. Therefore, it is imperative to keep these limitations in mind when trying to separate GrIS mass loss trends from internal variability of the GrIS climate system.

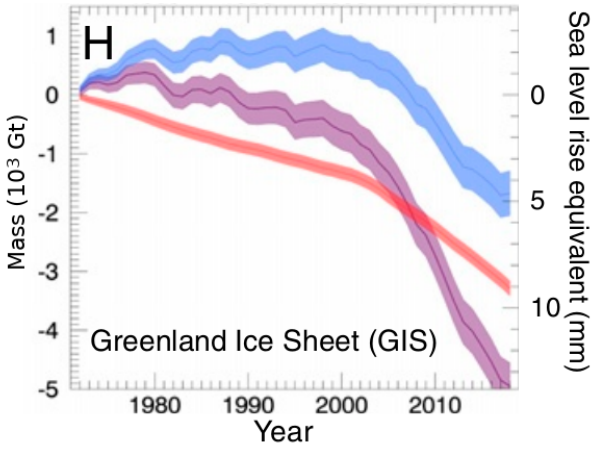

Figure 2.1: **Cumulative mass balance component anomalies (Mouginot et al. (2019), p.4)** Cumulative anomalies of GrIS mass balance components: SMB (blue), ice discharge (red) and total mass balance anomalies (purple) during 1972-2018.

The partitioning of the recent mass loss into SMB and ice discharge contribution (D) is sensitive to the reference period. Mouginot et al. (2019) extend the mass budget method to the start of the Landsat data archive in 1972. Within their study, the authors constrain 85% of all glacial ice discharge directly and 15% indirectly using a combination of ice thickness, surface elevation, velocity and SMB (Mouginot et al. 2019). This methodological approach yields that between 1972-2018 ice discharge into the ocean has dominated cumulative Greenland mass loss and sea level rise contribution. By partitioning the mass balance anomalies, the authors find that ice discharge has contributed 66 ± 8% to the the mass anomalies and only 34 ± 8% came from surface melt and SMB between 1972 and 2018 (see Fig.2.1). However, the exact value of anomalies in D in this study might be sensitive to the way the steady state value of the ice discharge is computed.

When focusing on the recent trends since 1996 and setting the 1958-1995 value of D constant to the 1996 values due to a lack of observations, Van den Broeke et al. (2016) conclude that 60% of total mass loss since 1991 is due to surface melt (see Fig.2.2). This drastic shift of recent GrIS mass loss towards surface melt has been confirmed by other studies; Enderlin et al. (2014) found that between 2009 and 2012 68% of total recent mass loss are due to SMB processes. This recent change of the GrIS mass loss to being dominated by surface

melt and therefore a decreasing SMB underlines the dynamic nature of recent changes in the Arctic near surface climate. It also highlights the need to constrain the individual surface energy budget contributions to the surface mass balance anomalies.

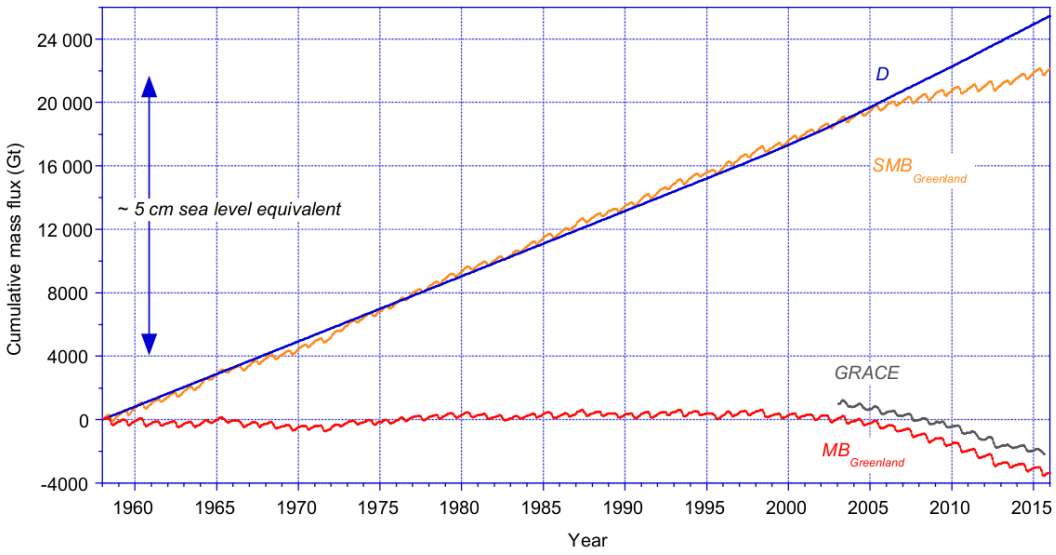

Figure 2.2: **Greenland Ice Sheet mass balance and its components (Van den Broeke et al. (2016), p.1943)**. Cumulative anomalies of GrIS mass balance (red), GRACE satellite gravimetry (grey, offset by 1000 Gt for better visibility), ice discharge into the ocean (D) and surface mass balance (SMB) from RACMO2.3 (Van den Broeke et al. 2016)

2.3.2 Contemporary distribution of the GrIS SMB

Spatial SMB variability: The ablation zone

The GrIS is separated into two distinct regions. In the interior, where mass gains through precipitation are greater than summer mass loss, lies the accumulation zone (i.e. SMB $>$ 0). The accumulation zone is characterized by thick layers of multi-year snow ("firn") and therefore a comparatively high albedo which reflects most of the incoming solar radiation back into space, leading to a surface energy budget controlled by longwave radiation variability. Conversely, near the edges of the GrIS adjacent to the tundra lies a narrow band where surface melt and runoff are greater than winter accumulation (i.e. SMB $<$ 0, Fig.(2.3),(Box et al. 2012)). Therefore, in the ablation zone during the summer melt season bare ice is exposed. In contrast to the accumulation zone, melt dynamics in the ablation zone are controlled by the variability in shortwave radiation due to the greater absorption of solar radiation (Van de Wal et al. 2005; Van den Broeke et al. 2011).

Most of the Greenland surface melt occurs in this narrow ablation zone. Towards the southwestern edges of the GrIS, bare ice ablation rates can reach more than 4 m of water equiv-

alent per melt season (average 2000-2011) according to a regional climate model study by Box et al. (2012). Observation-based studies have found even greater ablation rates in the ablation zone for single years, reaching values of almost 6 m water equivalent during the 2009-2010 melt season (Van de Wal et al. 2005; Van de Wal et al. 2012). However, the extent of the ablation zone itself is highly variable and depends strongly on the local geographical (i.e. surface slope) and climatological conditions (i.e. snow accumulation rates). While the ablation zone spans up to 100 km in width in the SW of the GrIS, steep slopes and high accumulation rates can narrow it down to a few kilometers or less in the east and southeast of the ice sheet (Fig.(2.3)). Because most of the surface melt and subsequent meltwater runoff into the ocean is concentrated in a very narrow ablation zone around the GrIS, it is imperative that models used to study the GrIS contribution to sea level rise are able to accurately resolve dynamics in the ablation zone. Therefore, regional climate models, which have a much higher resolution than general circulation models, are a useful tool to study the regional dynamics of the Greenland Ice Sheet melt.

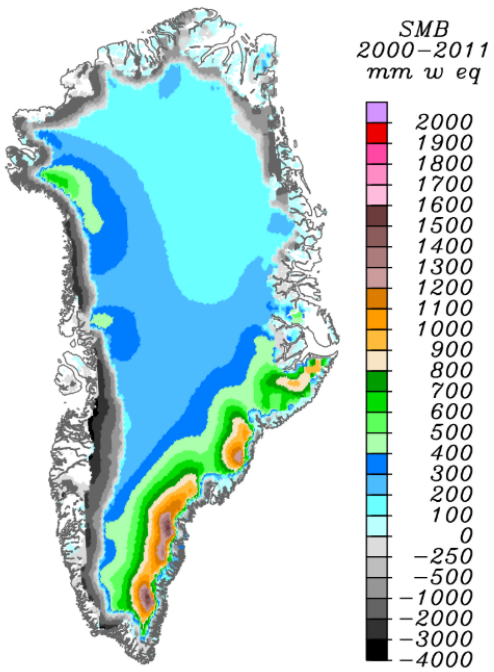

Figure 2.3: **Average annual surface mass balance over the GrIS (Box et al. (2012), p.825)** Average annual surface mass balance over the GrIS between 2000 and 2011 in mm water equivalent (mmwe).

Spatial SMB variability: The influence of the North Atlantic storm track

However, the GrIS is further separated into distinctive climatological areas based on its synoptic-scale features (e.g. precipitation, temperature). Figure (2.3) also highlights a distinct difference in annual mean precipitation, influencing the overall surface mass balance

(Box et al. 2012). Overall, the SE and E of the GrIS experiences the highest annual SMB with values up to 1500 mm w.e. (Box et al. 2012). The high SMB due to great precpitation amounts in the SE to E sector of the GrIS are likely due to the influence of the North Atlantic storm track, with low-pressure systems usually forming near Newfoundland and subsequently tracking eastwards towards Iceland or the British Isles (Rogers 1997). At the edge of this path, the SE and E parts of the GrIS receive the highest precipitation amounts, leading to the highest snow accumulation rates and SMB values (Ettema 2010).

Conversely, Figure (2.3) also shows a very sharp SMB gradient towards the North of the GrIS, where very cold and dry air, paired with only very infrequent low-pressure influence leads to very low precipitation amounts. This low annual snow accumulation (annual precipitation $<$ 200 mm (Ettema 2010)) subsequently leads to very low SMB values in the N and NW sector of the GrIS, even in the higher accumulation zone where little melt occurs (Van de Wal et al. 2012). This separation in distinct climatological areas has to be taken into account when discussing the recent increase in melt and the underlying causes, especially when discussing the influence of clouds on the surface energy budget and melt.

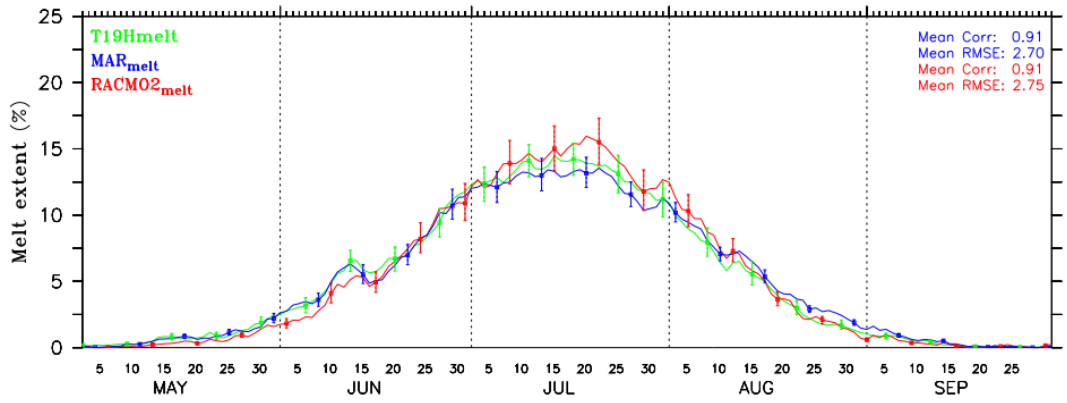

Figure 2.4: **May-September melt extent in % of total GrIS area from passive remote sensing and regional climate model data (Fettweis et al. (2011), p.367).** GrIS melt extent (%) from MAR (blue), RACMOv2 (red) and passive remote sensing data (green) between May and September.

Temporal SMB variability: The summer melt season

However, additional to the spatial patterns of SMB, also the temporal characteristics of melt and SMB are highly important. Over nine months of the year, the GrIS experiences little or no melt, due to the lack of incoming solar radiation and subsequent surface cooling. On the other hand, basically all of the GrIS surface melt occurs within the three summer months June, July and August (JJA, Fig.(2.4)), which is spatially concentrated over the ablation zone (Fig.(2.3) and (2.7))(Box et al. 2012; Fettweis et al. 2011).

Figure (2.4) shows that the melt season, which is defined as three consecutive days with more than 5% of the GrIS area melting, usually starts in early to mid-June according to MAR and RACMO (Fettweis et al. 2011). The melt season usually reaches its peak in mid-July (±15%) and fully vanishes by mid-September. Because the ablation zone usually experiences a ten times greater melt intensity than the accumulation zone (Fig.(2.7), (Box et al. 2012)) and due to its short temporal focus on JJA it is imperative to partition any analysis of the SMB, melt and the underlying drivers of the GrIS surface energy budget into its different spatial and temporal characteristics. Especially the effect of clouds on the SMB and melt has so far not been tested, taking into account the spatial heterogenity (most melt in the ablation zone) and the temporal focus of melt to the summer months with almost 24h of solar radiation per day.

2.3.3 Recent changes in GrIS SMB

Over the last two decades a reduction in the surface mass balance has become the most significant contributor to GrIS mass loss (Enderlin et al. 2014; Van den Broeke et al. 2009; Van den Broeke et al. 2016; Van den Broeke et al. 2017; Mouginot et al. 2019). Depending on the period of study, an increase in summer melt and the subsequent decrease in SMB has contributed up to 68% of total mass balance anomalies (Enderlin et al. 2014). Over the period of of 1991-2015 the GrIS SMB has decreased at a rate of 3.3% per year, while it was stable during the 30 preceeding years (1961-1990) (Van den Broeke et al. 2016). Van den Broeke et al. (2016) found, using the regional climate model RACMO, that surface melt and subsequent runoff of water into the ocean is the main contributor to the contemporary SMB decrease. By comparing the regional climate models MAR and RACMO with passive remote sensing data, Fettweis et al. (2011) found an increase in melt area over the GrIS during 1979-2009 between $26 \pm 14 \cdot 10^4$ km^2/yr in RACMO and $33 \pm 13 \cdot 10^4$ km^2/yr in MAR, which both agree well with remote sensing data (Fettweis et al. 2011; Van den Broeke et al. 2016). The total precipitation amount (snow+rain, Fig.(2.5)) shows a slight but statistically insignificant decrease during the same period of 1991-2015. Additionally, the fraction of precipitation falling as rain has increased slightly, from 3.3% during 1961-1990 to 3.9% during 1991-2015 (Van den Broeke et al. 2016). Furthermore, also the refreezing fraction of the liquid water on the surface of the GrIS (rain and meltwater) has decreased slightly, from 44% between 1961-1990 to 41% between 1991-2015 (Van den Broeke et al. 2016), slightly enhancing GrIS runoff efficiency. In conclusion, the largest proportion of the recent GrIS SMB decrease can be attributed to an increase in surface melt and subsequent meltwater runoff, while the influence of changes in precipitation and refreezing of water in the snowpack are limited.

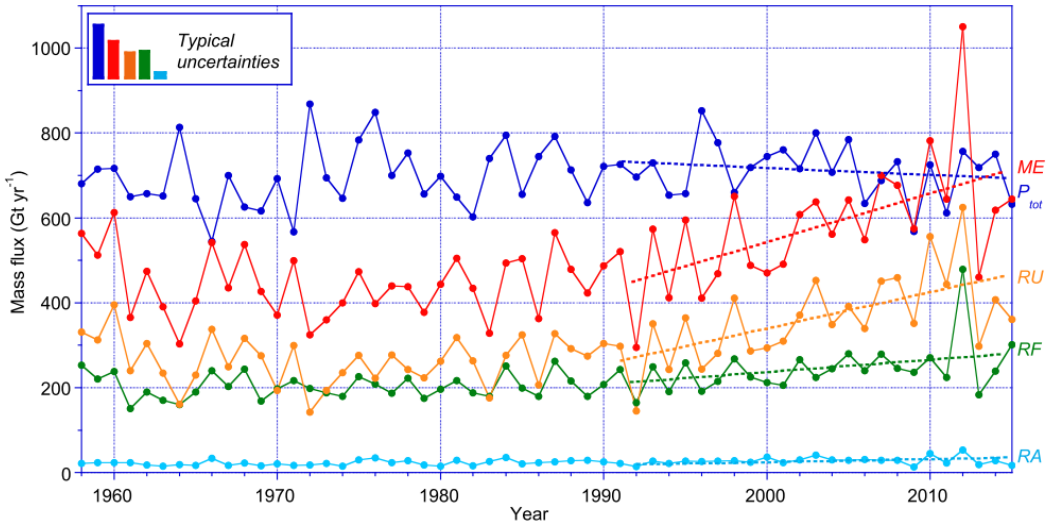

Figure 2.5: **Time series of GrIS surface mass balance components (Van den Broeke et al. (2016), p.1937).** Time series of 1958-2015 Surface mass balance components (Gt/yr) from the regional climate model RACMO over the Greenland Ice Sheet (Van den Broeke et al. 2016). Dotted lines represent the linear trend (i.e. first-order linear fit) during the period 1991-2015. P_{tot} is the total precipitation, ME is surface melt, RU is meltwater runoff, RF is the amount of refrozen water and RA stands for the total amount of liquid precipitation (i.e. rain).

2.3.4 Causes of recent trends in GrIS surface mass balance

Surface energy budget and the melt-albedo feedback

While the mass balance and surface mass balance have both been partitioned into its contributing factors (e.g.(Van den Broeke et al. 2016; Mouginot et al. 2019)), before this study this has not been done in a similar fashion for the GrIS surface energy budget. However, to identify the main changes in the SEB of the GrIS and the underlying physical changes (e.g. changes in temperature, cloud cover, etc.) a similar partitioning approach of the surface energy budget would be needed. Van den Broeke et al. (2016) name the increasing temperatures as the main cause of the recent SMB decrease and melt increase. This statement has also been named as the primary cause of contemporary GrIS melt inducing the melt-albedo feedback in other studies (Fettweis 2007; Fettweis et al. 2011; Hanna et al. 2008; Tedesco et al. 2011). If increasing tropospheric temperature levels were the main cause of the recent GrIS melt increase, then the primary driver of the surface energy budget anomalies would have to come from downwelling longwave radiation, because emitted longwave radiation is directly proportional to the atmospheric temperature (Eq.(2.5)). However, this statement has so far not been thouroughly investigated in the literature.

On the contrary, observational studies clearly show that over the ablation zone, where most

of the melt occurs, absorbed shortwave radiation is the primary driver of surface melt and ice ablation (Van den Broeke et al. 2011; Van de Wal et al. 2005). Furthermore, Van de Wal et al. (2005) also show that 84% of all the energy for melt along the K-transect in SW Greenland stems from net radiation, highlighting the importance of the radiative components of the SEB. Furthermore, Van den Broeke et al. (2011) argue that absorbed shortwave radiation is the main driver of meltwater production and melt variability. Over parts of the GrIS that are close to the tundra, the sensible heat flux provides the second most energy (Van den Broeke et al. 2011). This is mainly due to the fact that the tundra can heat up signficantly during summer (Van den Broeke et al. 2011). Figure (2.6) illustrates clearly how the interplay between the inter-annual variability of longwave and shortwave fluxes creates a very brief and well-defined melt season during JJA only, when solar radiation reches its peak together with a slight increase in downwelling longwave radiation (LWD) (Fettweis et al. 2011). Because absorbed shortwave radiation during melt season (JJA) is the main driver of melt variability, it is surprising that prior to this study it has not been tested whether or not is plausible to assume that temperature and longwave radiation anomalies are the main drivers of the recent melt anomalies.

$$LW = \epsilon \cdot \sigma \cdot T^4 \tag{2.5}$$

However, there is one study that tries to identify the main changes in the surface energy budget driving the melt-albedo feedback. Box et al. (2012) find, there is a clear signal of increasing downwelling shortwave radiation (SWD) over the GrIS, especially over the NW and SW parts. Using the regional climate model MAR and satellite data to constrain the GrIS albedo, they find that a combination of increasing SWD and a decrease of the albedo (α) have contributed $45 \cdot 10^{18}$ J of extra absorbed SW energy (SWnet) to the GrIS surface energy budget. This increase of SWnet over the ablation zone accounts for more than 80% of the melt increase between 2000 and 2011, of which 93% occurs during JJA and 81% over the ablation zone (Box et al. 2012). Figure (2.7) also shows that there has been an increase of +5.4 W/m^2 in SWD and an increase of +11.0 W/m^2 in SWnet over the ablation zone, due to an overlapping decrease in the surface albedo (i.e. melt-albedo feedback) (Box et al. 2012; Tedstone et al. 2017; Alexander et al. 2014).

Interestingly, despite the fact the period of 2000-2011 lies within a time of sustained Arctic warming, Box et al. (2012) actually find a decrease in LWD of -1.3 W/m^2. However, the LWD reduction is less than the increase in SWD and SWnet, leading to a combined positive radiation increase of +8.3 W/m^2. The fact that LWD anomalies are negative (i.e. less longwave energy reaching the surface) during a period of atmospheric warming is somewhat contradictory to most other literature. Combining the results that SWD and SWnet have increased while LWD has decreased during a period of atmospheric warming however, could point towards a change in cloud properties enhancing SWD (i.e. cloud microphysics or temporal and spatial cloud cover reductions) while simultaneously decreasing LWD by a

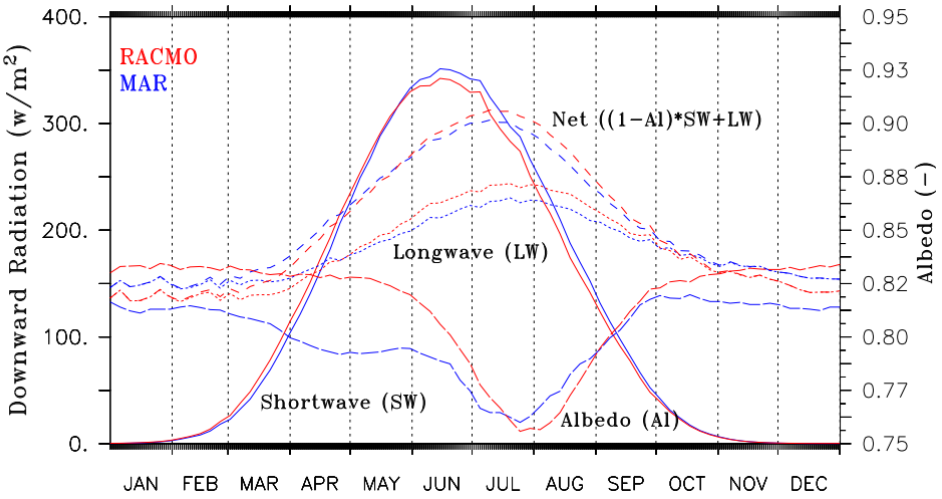

Figure 2.6: **Mean annual cycle of surface energy budget components (Fettweis et al. (2011), p.370).**

		Ablation Area			Accumulation Area		
Parameter	Units	Average	Linear change of average	St. dev. residuals	Average	Linear change of average	St. dev. residuals
T_{air}	°C	−1.6	0.5	0.4	−8.8	0.5	0.5
Snow	mm w.e.	15.9	−6.9	2.1	28.2	−7.3	3.4
Rain	mm w.e.	39.3	−10.4	10.4	6.0	−2	1.5
Rain/Snow	none	2.5	0.4	0.7	0.2	0.0	0.0
$S\downarrow$	W m^{-2}	280.9	5.4	3.8	296.3	3.4	3.0
S_{net}	W m^{-2}	110.8	11.0	7.4	60.5	2.3	1.6
$L\downarrow$	W m^{-2}	242.1	−1.3	3.5	209.4	0.6	4.1
L_{net}	W m^{-2}	−64.6	−2.7	3.1	−61.0	−1.5	2.1
$S\downarrow + L\downarrow$	W m^{-2}	523.0	4.2	1.5	505.8	4.0	1.9
R_{net}	W m^{-2}	46.2	8.3	6.2	−0.5	0.8	0.7
Q_{SH}	W m^{-2}	17.7	3.2	2.1	5.0	0.1	0.5
Q_{LH}	W m^{-2}	−4.5	0.3	0.8	−0.6	0.1	0.2
$Q_{SH} + Q_{LH}$	W m^{-2}	13.1	3.4	1.9	4.4	0.2	0.4
$\alpha_{MOD10A1}$	none	0.673	−0.091	0.021	0.809	−0.046	0.006
Melt	mm w.e.	1257.9	261.5	158.0	123.9	18.1	18.2

Figure 2.7: **Trends in near-surface climate variables over the GrIS during 2000–2011 from the regional climate model MAR and satellite data (Box et al. (2012), p.831).**

reduction in the atmospheric emissivity (ϵ, Eq.(2.5)).

Circulation changes

Recent studies clearly show that circulation anomalies have played a pivotal role in the GrIS melt increase over the last two decades (Box et al. 2012; Mattingly et al. 2018; Hanna et al. 2016; Hanna et al. 2018; Fettweis et al. 2013a; Tedesco et al. 2016). Fettweis et al. (2013a) show that an increase in negative North Atlantic Oscillation (NAO) phases over Greenland has led to an increase in anticyclonic circulation over the GrIS. The frequency of anticyclonic conditions has increased from about 15% of all melt season days to 40%, equivalent to a 2.66 times higher frequency (Fettweis et al. 2013a). This change of the NAO to a negative state has also been highlighted using a different circulation metric, the Greenland Blocking Index (GBI), which has switched to a positive state, indicating a higher than normal 500 hPa geopotential over Greenland (Hanna et al. 2016). Furthermore, the state change of the NAO and GBI has increased the advection of warm-air especially along the western half of Greenland, but also increased drier conditions due to synoptic-scale subsidence over the GrIS (Box et al. 2012; Fettweis et al. 2013a; Hanna et al. 2016).

Circulation anomalies have also been shown to be very important for future Greenland Ice Sheet melt projections (Delhasse et al. 2018; Hanna et al. 2018). Delhasse et al. (2018) report that mainly through an increase in surface melt, the Greenland Ice Sheet surface mass balane reduction could potentially double if the recent anticyclonic circulation anomalies were to persist during the 21st century (Delhasse et al. 2018). This study finds, that there are two main reasons behind this doubling of surface melt: (1) An increase in downwelling shortwave radiation through a reduction in clouds and (2) an overlapping increase in downwelling longwave radiation through more frequent warm-air advection events (Delhasse et al. 2018). Delhasse et al. (2018) and Hanna et al. (2018) conclude that using projections that do not capture the recent increase in atmospheric blocking events over Greenland will lead to significant uncertainties in future Greenland melt and sea level rise projections (Delhasse et al. 2018).

However, despite the apparent importance of circulation anomalies for future Greenland Ice Sheet melt, currently none of the state-of-the-art general circulation models are able to model them (Hanna et al. 2018). Hanna et al. (2018) show, by analysing all of the available CMIP5 (Climate Model Intercomparison Project 5th Phase) models, that the observed changes in the Greenland Blocking Index (GBI) lies outside of the variability of the models' historic reconstructions but also outside of their variability in future projections (until 2100, see Fig.(2.8)). Additionally, the authors also show that the GBI is decreasing in future projections, instead of increasing as observed over the last two decades (Hanna et al. 2018). It is not clear whether the observed increase in GBI over the last 20 years is due

to natural variability, or a long-term response to changes in the Arctic climate system due to global warming (Hanna et al. 2018). However, Fig.(2.8) clearly shows that the CMIP5 models in the RCP4.5 and 8.5 scenarios are at least unable to depict the internal variability in atmospheric circulation over Greenland. Therefore, we also have to question their ability to accurately predict the future evolution of the Greenland Ice Sheet surface mass balance.

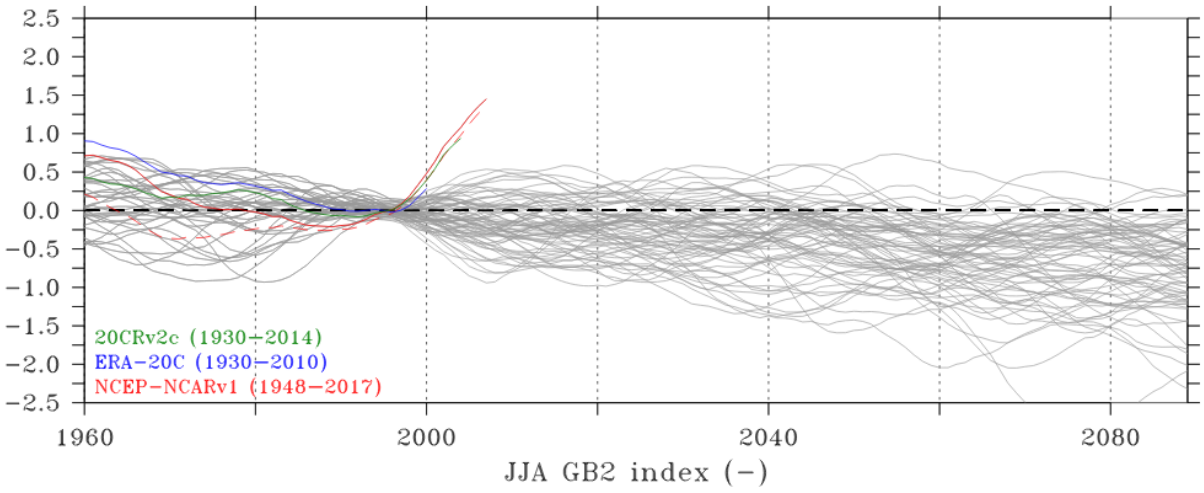

Figure 2.8: **Future projections of the Greenland Blocking Index 1950-2100 (Hanna et al. (2018), p.3289).** Time series of the observed Greenland Blocking Index (GBI) from two slightly different computational methods (solid and dashed red lines, for Methods see Hanna et al. (2018)). The green line is the GBI computed from 20CRv2c reanalysis data and the blue line is from ERA-20C reanalysis. The GBI time series from all the CMIP5 GCMs is shown in grey (Hanna et al. 2018).

The drivers behind the recent circulation anomalies are manifold. Screen et al. (2013) and Screen et al. (2010) show that these circulation anomalies are closely connected to the vanishing Arctic sea ice, which directly increases the exchange of heat between the ocean and the troposphere, weakens near-surface temperature inversions and therefore likely has a controlling influence on the atmospheric circulation and on the polar vortex. However, also a connection to the slowing of the Atlantic Meridional Overturning Circulation (AMOC) has been suggested (Rahmstorf et al. 2015; Caesar et al. 2018), which is mainly caused by the increase in Arctic freshwater input into the ocean (Bamber et al. 2012; Bamber et al. 2018). Furthermore, downstream of the more frequently occuring atmospheric ridge over Greenland, Svalbard has experienced more northwesterly airmass advection during summer, leading to cooler and cloudier conditions, surpressing a similar melt increase as observed over the GrIS (Lang et al. 2015). This leads to the conclusion that the recent increase in GrIS melt and runoff and its contribution to barystatic global sea level rise is more a result of regional atmospheric circulation conditions, than a direct effect of global temperature rise (Fettweis et al. 2013a; Hahn et al. 2018).

Influence of cloud cover

On average, the Arctic is covered by clouds 70% of the time, making it one of the cloudiest places on Earth (Wang et al. 2005). Depending on the various surface types found in the Arctic (tundra, sea ice, open ocean, land ice), clouds in the Arctic show a huge variability, ranging from persistent stratiform clouds over the Arctic Ocean ("sea fog") to very thin ice clouds at the top of the Arctic atmosphere ("cirrus").

Clouds have a profound effect on the surface energy budget of polar regions (Shupe et al. 2004; Miller et al. 2015; Miller et al. 2017; Warren 1982; Bintanja et al. 1996; Wang et al. 2018; Wang et al. 2019; Perovich 2018; Cesana et al. 2017). Depending on their height, temperature, water phase and water/ice content, clouds can either enhance or decrease the radiative fluxes towards the surface (Bintanja et al. 1996). Given the usually cold and relatively dry climate of the interior of the GrIS, it is somewhat surprising that even at Summit Station (3000 m a.s.l.) in the middle of the GrIS, clouds occur around 80% of the time throughout the year (Shupe et al. 2013; Miller et al. 2015; Miller et al. 2017). Over these dry regions of the Arctic, the longwave warming usually dominates shortwave cooling (Shupe et al. 2004). Normally, the atmospheric emissivity (ϵ, eq.(2.5)) here is very low and the bright snow surface reflects great proportions of the incoming solar radiation. Therefore, in these dry and cold climates, clouds normally enhance the downwelling longwave fluxes more than they reduce the absorbed solar radiation (i.e. clouds warm the surface) (Shupe et al. 2004).

However, in parts of the Arctic where clouds are usually thicker due to higher temperatures and where the surface is darker (bare-ice ablation zone, tundra, open sea water) clouds have been found to act as a cooling influence on the surface energy budget, especially during summer (Shupe et al. 2004; Wang et al. 2018; Wang et al. 2019).

In the extreme melt year of 2012, 97% of the GrIS area melted simultaneously (Bennartz et al. 2013; Nghiem et al. 2012). Low-level liquid clouds have exacerbated these melting records (Bennartz et al. 2013), by enhancing the LW warming of the surface, while being transparent enough to allow solar radiation to penetrate down to the surface. Conversely, clouds in the Arctic can also cool the surface. Over open sea water for example, high-pressure systems and reduced cloud cover have contributed 32 W/m^2 to the SEB over the Western Arctic Ocean, equivalent to 0.3 m of sea ice melt or potentially warming the ocean by 2.4 K (Kay et al. 2008). Over Greenland, the recent melt increase since the mid-1990s has been caused by a shift in the North Atlantic Oscillation (NAO) towards a more anticyclonic and sunny state (Hanna et al. 2014; Hanna et al. 2016; Box et al. 2012; Fettweis et al. 2013a). The influence of clouds on GrIS melt however and its connection to the recent state shift in the NAO has not been thoroughly investigated.

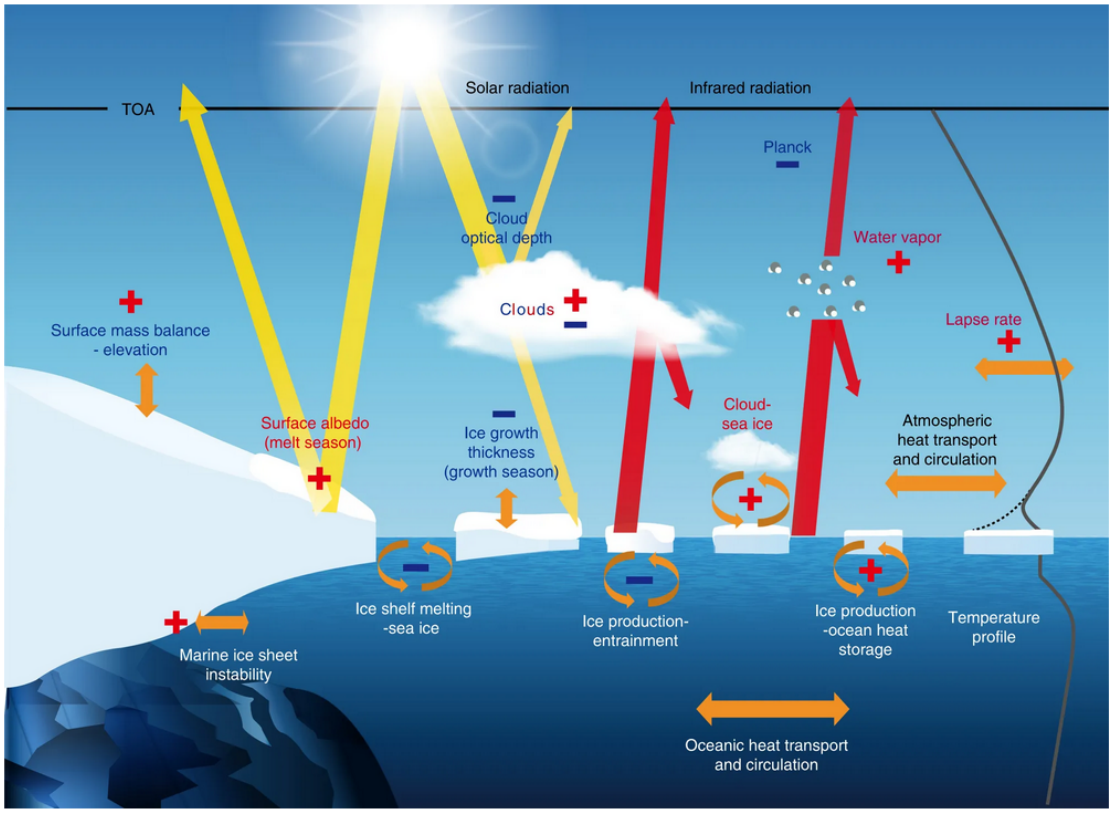

Figure 2.9: **Feedback loops over polar ice sheets and sea ice (Goosse et al. (2018)).**

Clouds over the GrIS have competing influences in the shortwave (solar) and longwave fluxes (Bintanja et al. 1996; Perovich 2018; Wang et al. 2018; Wang et al. 2019; Shupe et al. 2004; Miller et al. 2015; Miller et al. 2017). Clouds can enhance the amount of LW radiation reaching the surface by increasing the atmospheric emissivity (ϵ, eq.(2.5)) and decrease the amount of solar radiation reaching the surface (Bintanja et al. 1996). Whether clouds are warming or cooling the surface is determined by the cloud radiative effect (CRE, eq.(2.6)) (Ramanathan et al. 1989; Perovich 2018). In this thesis a positive CRE marks areas and times when clouds warm the surface and a negative CRE where clouds cool the surface (i.e. more SW reduction than LW increase).

There is a multitude of environmental (e.g. surface albedo) and cloud microphysical properties (e.g. cloud water phase) that are playing a role in determining the CRE (Bintanja et al. 1996; Curry et al. 1992). Important cloud (microphysical) properties influencing the CRE are the spatial and temporal cloud cover, the water phase of the cloud particles (liquid, mixed-phase or ice clouds), the cloud particle size and shape distribution and the total amount of water mass in the clouds (liquid/ice water path) (Bintanja et al. 1996).

However, also the environmental conditions play a major role. The solar zenith angle (SZA), vertial temperature profile, cloud (base) height, surface type/albedo and the suspended par-

ticles in the clouds (i.e. aerosols) all influence the CRE from the environmental perspective (Curry et al. 1992; Bintanja et al. 1996; Shupe et al. 2004; Ramanathan et al. 1989). Furthermore, environmental conditions are also influenced by clouds. Because clouds filter out parts of the near-infrared spectrum where the ice and snow albedo is particularly low, the presence of clouds increases the albedo of the underlying surface (Warren 1982; Bintanja et al. 1996). The SZA also plays a crucial rule in the SW CRE, because the albedo of the clouds and the underlying surface is directly related to the angle of the incident radiation - 90° between sun and surface would lead to the minimum albedo. This effect is a direct consequence of the fact that photons don't penetrate as deep in the snowpack when the angle is acute, because they are more likely to interact with the snow closer to the surface (Warren 1982). Therefore, the SW CRE not only has a strong seasonal cycle over polar regions, but also a significant diurnal component (Wang et al. 2019; Wang et al. 2018), while it also varies significantly spatially. In conclusion, physically constraining the CRE (eq.(2.6)) can prove to be a very challenging task.

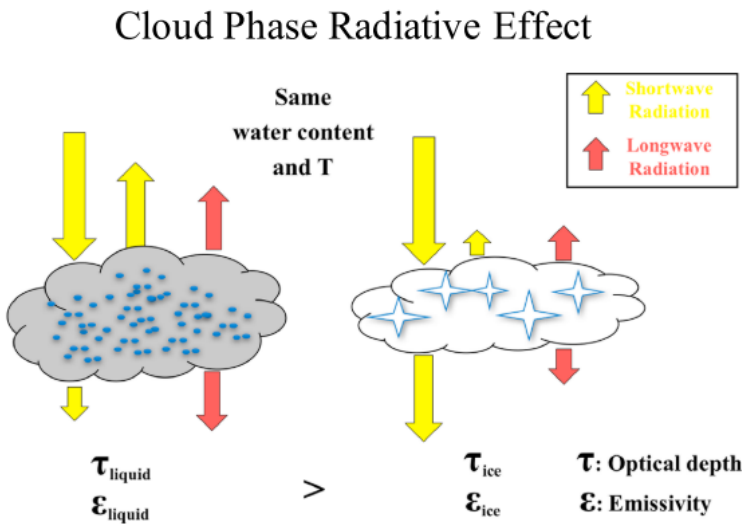

Figure 2.10: **Impacts of cloud water phase on the shortwave and longwave energy budget (Cesana et al. (2017)).** ε stands for the cloud longwave emissivity, while τ stands for the cloud optical depth/thickness.

This combination of environmental and internal factors related to cloud properties and their radiative impacts leads to a very complex patterns of the CRE over the Arctic and the GrIS in particular. Figure (2.9) tries to schematically explain these complex interactions between glacial ice, sea ice, open ocean water and clouds, which are often hard to constrain. For example, in the shortwave spectrum, the cloud optical thickness, $\tau = ln(SW_{in}/SW_{transm})$, exerts a cooling influence, which can directly influence sea ice growth below. Thicker sea ice in turn has a higher albedo and also suppresses the sensible heat exchange from the ocean towards the atmosphere, both exerting a cooling influence on the atmosphere. However, the

extent of sea ice also has an influence on the cloud-sea ice feedback in the longwave part. Sea ice, because it reflects most of the incoming solar radiation, usually creates near-surface temperature inversions, enhancing the formation of low-level liquid clouds. However, this formation of low-level liquid clouds in turn enhances the warming in the longwave part of the spectrum. This example illustrates how complex the interactions in the shortwave and longwave part of the spectrum can be in high-latitudes, given the complicated environmental conditions.

$$CRE = R^{\uparrow\downarrow}_{SW,all-sky} + R^{\uparrow\downarrow}_{LW,all-sky} - R^{\uparrow\downarrow}_{SW,clear} - R^{\uparrow\downarrow}_{SW,clear} \tag{2.6}$$

Due to the complex nature, there is also a complex, although slightly limited, set of research studies about the cloud radiative effect in the Arctic and Greenland. Shupe et al. (2004) found that the Arctic CRE is positive throughout large parts of the year. However, Shupe et al. (2004) also found that clouds cool the surface during a brief period in summer, when cloud shading effects are larger than their longwave greenhouse effect (Shupe et al. 2004), when the ice albedo is lowest due to surface melt and snow grain metamorphism (Warren 1982; Bintanja et al. 1996). Due to the frequent presence of boundary layer temperature inversions over the GrIS, clouds often emit longwave radiation at higher temperatures than the snow and ice surface below, resulting in a net longwave warming (Shupe et al. 2004). This effect is especially relevant over the interior of the GrIS, where low-level liquid clouds over a bright snow-covered surface have been found to frequently warm the surface (Bennartz et al. 2013; Miller et al. 2015; Miller et al. 2017; Wang et al. 2018; Wang et al. 2019).

The first in-depth analysis of the GrIS CRE over the whole ice sheet, combining observations and reanalysis, has only very recently been published: Wang et al. (2019) found a warm-center CRE over the GrIS, but also indicate that clouds warm the interior but cool the darker ablation zone. These results are in stark contrast to a previous study by Van Tricht et al. (2016) who find, by a combination of regional climate model output and satellite observations, the strongest cloud warming effect over the dark ablation zone, likely because the authors use a model of insufficient spatial resolution to resolve the ablation zone at 2°x 2°. Conversely, using all available in-situ radiation measurements, Wang et al. (2018) and Wang et al. (2019) take into account the spatial heterogenity of the GrIS surface albedo, as well as the temporally varying insolation conditions to arrive at the conclusion that clouds can cool the surface during JJA in the ablation zone, and warm the surface all year in the accumulation zone.

2.3.5 Future projections of the GrIS SMB

The future Greenland Ice Sheet surface mass balance will decrease with global warming (Church et al. 2013; Fettweis et al. 2013b). On one side, most projections simulate an increase in precipitation of roughly 5% for every degree of warming over Greenland (Church et al. 2013). On the other side however, meltwater runoff will increase faster with rising temperatures and is projected to outweigh the increase in precipitation (Church et al. 2013; Fettweis et al. 2013b). The great increase in meltwater runoff from the GrIS will lead to a sustained contribution of the GrIS surface mass balance to global sea level rise during the 21st century (Fettweis et al. 2013b; Church et al. 2013). Overall, the IPCC AR5 report reports a projected contribution of the GrIS surface mass balance to future global sea level rise between 0 and 0.13 m (Church et al. 2013). However, the IPCC AR5 only uses middle-range emission scenarios RCP4.5 and SRES scenario A1B (similar to RCP6.0) and does not provide estimates of GrIS SMB contribution to sea level rise from the high-emission scenario RCP8.5 (Church et al. 2013).

Greenland is projected to undergo significant changes during the 21st century, mainly due to the modification of the GrIS surface mass balance (Fettweis et al. 2013b; Franco et al. 2013; Church et al. 2013). Fettweis et al. (2013b) show, using an ensemble of CMIP5 GCM forced regional Greenland climate projections, that the Greenland Ice Sheet will contribute up to 13 cm to global sea level rise in the 21st century. Additionally, the same authors also show that the beginning of irreversible ice sheet loss (i.e. time when SMB < 0) will occur in 2070 based on the mean of their 30 member ensemble in the high-emission scenario (Fettweis et al. 2013b). The same high-resolution climate model ensemble also shows that snowfall will increase in the accumulation zone but it highlights a rapid melt acceleration over the ablation zone (Fettweis et al. 2013b). This combination of factors will initially lead to thickening of the ice sheet in the interior but also rapid ice sheet thinning along its periphery (Fettweis et al. 2013b). Additionally, Fettweis et al. (2013b) also show that an increasing fraction of the overall precipitation will be falling as rain (Fettweis et al. 2013b). However, most of this surplus of rainwater will fall over the bare-ice ablation zone and will therefore only be a limited contributor to the albedo-melt feedback (Fettweis et al. 2013b).

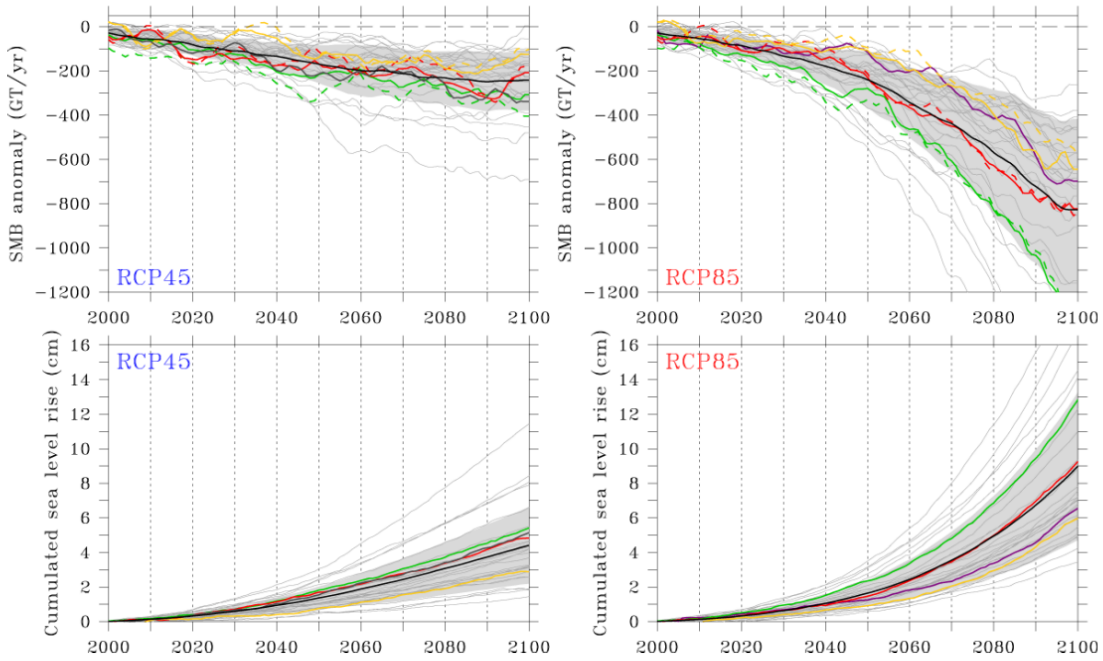

Figure 2.11: **Future Greenland sea level rise and surface mass balance projections for the 21st century (Fettweis et al. (2013b), p.484).** The top row shows the 30 GCM ensemble prediction of RCP4.5 surface mass balance anomalies (top left) and the same analysis for RCP8.5 (top right). The bottom row shows the cumulative sea level rise through meltwater runoff into the ocean from the same 30 member ensemble.

However, Greenland Ice Sheet melt projections for the 21st century show great uncertainties, even within one prescribed emission scenario (Fettweis et al. 2013b; Franco et al. 2013; Hofer et al. 2019; Delhasse et al. 2018; Church et al. 2013). Fettweis et al. (2013b) show using the regional climate model MAR and a subset of downscaled CMIP5 GCM simulations, that even within one emission scenario the anomalies in the surface mass balance at the end of the 21st century can vary by more than a factor of three (RCP8.5 Minimum SMB anomaly: -324 Gt/yr, Maximum SMB anomaly: -1050 Gt/yr). However, when applying a statistical downscaling based on the temperature anomalies of all the GCMs, the same authors show that the SMB anomalies can show even greater uncertainties: In RCP4.5 the SMB anomalies can potentially vary between 0 Gt/yr and -700 Gt/yr and in RCP8.5 roughly between -300 Gt/yr and more than -1400 Gt/yr in 2100 (Fig.(2.11), top row) (Fettweis et al. 2013b). Subsequently, this difference in project GrIS SMB also leads to uncertainties in GrIS sea level rise contribution of a similar magnitude (Fig.(2.11), bottom row). Unfortunately, so far very little is known what the underlying causes are on a physical process-level that cause such significant differences in projecting the future GrIS sea level contribution of individual ensemble members.

One approach to identify the underlying causes of uncertainties in future Greenland melt projections is to look at the differences in the projected surface energy fluxes (Franco et al.

2013). Franco et al. (2013) used multiple CMIP5 model projections and a regional climate model to partition the surface energy budget changes over the Greenland Ice Sheet at a high resolution and for multiple forcing fields. The study shows, that in a warming climate the incoming shortwave radiation will decrease due to an increase in cloudiness, while the sensible heat flux and downwelling longwave radiation will increase (Franco et al. 2013). Additionally, Franco et al. (2013) also highlight significant differences in the contribution of the different radiative components to the GrIS melt increase between the CMIP5 forced simulations. The authors conclude that the overlapping increase in downwelling longwave and reduction in incoming shortwave radiation might be due to an increase in cloud cover. This might be a problematic assumption, given that not only a change in spatial and temporal cloud coverage, but also in cloud microphysics without a change in cloud coverage might lead to a similar increase in longwave and decrease shortwave radiation (i.e. an increase in cloud optical depth) (Franco et al. 2013). Furthermore, the authors also do not show how much of the differences in the projected melt amounts might be due to differences in modelled cloud properties (Franco et al. 2013). Therefore, this thesis will use the shortcomings of this study as a starting point, by identifying the underlying causes of the discrepancies in projected Greenland melt and how much of these differences in melt are due to differences in modelled cloud properties.

2.4 Summary

In this chapter we have explored the state-of-the-art in Greenland (surface) mass balance and climate research and the associated gaps in knowledge. The mass balance and surface mass balance have been partitioned in their contributing components using multiple independent approaches (e.g. (Van den Broeke et al. 2016; Enderlin et al. 2014; Mouginot et al. 2019; Van den Broeke et al. 2009). However, this chapter also highlights a distinct lack in knowledge about the source of the surplus of surface energy fluxes required to produce such a strong melting signal over the Greenland Ice Sheet as observed over the last two decades. Furthermore, given the direct and strong influence of clouds on the Greenland Ice Sheet surface energy budget, it is somewhat surprising that only a very limited set of literature has been published on this topic prior to this thesis. Furthermore, we have also explored that within these few research projects, some have distinct issues with the dynamic nature of the cloud radiative effect and neglect the spatial (ablation vs. accumulation zone) and temporal (melt-season) variability (Van Tricht et al. 2016). Furthermore, a wealth of research exists on the topic of uncertainties due to clouds in future global climate projections (e.g. (Tan et al. 2016; Tan et al. 2019; Storelvmo 2017)). However, there is a distinct gap in knowledge about the influence of clouds on more regional uncertainties in future Greenland sea level contribution using high-resolution regional climate models.

Therefore, in this thesis I (1) try to the establish the accuracy of regional climate models when modelling changes in cloud properties and the surface energy budget over Greenland, (2) partition the recent surface energy budget anomalies over the last two decades and identify the contribution from a surplus in solar radiation due to a reduction in cloud cover as significant and (3) examine the contribution of cloud microphysics to the uncertainties in future Greenland melt projections. In conclusion, with this thesis I hope to address at least some of the shortcomings highlighted above and to initiate additional studies based on the presented results.

Chapter 3

Models and remote sensing data

3.1 Preface

This chapter will establish the most important tools and data used throughout this thesis. We will start by exploring the main advantages and shortcomings of global and regional climate models. Furthermore, this chapter will highlight the main scientific methods behind the "magnifying glass" approach used in (polar) regional climate models, leading to a detailed description of the polar regional climate model MAR, on which this thesis relies heavily. Towards the end of this chapter, we will focus on observations of the Greenland Ice Sheet climate system. We will explore the PROMICE in-situ weather station network, as well as satellite remote sensing data from the MODIS and AVHRR sensors. Due to the challenging environment in high-latitudes and the bright background surface when observed from space, one needs to consider carefully the shortcomings of these observational methods.

3.2 (Polar) Regional climate models

Regional climate models (RCMs) are an important research tool to study the climate at the regional to local scale (Giorgi et al. 1989; Dickinson et al. 1989; Laprise 2008; Rummukainen 2010). RCMs bridge the gap between coarse climate simulations from global climate models (GCMs) and regional scale climate impacts. The core of most RCMs is built on limited area models (LAMs), extensively used in meteorological weather forecasting (Skamarock et al. 2008). In meteorological applications these LAMs are used on the timescale from hours (e.g. thunderstorm development) to one week (e.g. local impacts of global weather predictions). When we run these LAMs over climatic timescales (years to centuries), they effectively become RCMs (Rummukainen 2010). NCAR conducted the first RCM studies in 1989. Since then RCMs have become very popular in climate studies and are run effectively

over most parts of the Earth (Rummukainen 2010; Giorgi et al. 1989; Dickinson et al. 1989).

Figure (3.1) shows a general overview of regional climate model domains embedded within a larger scale general circulation model or reanalysis field (Rummukainen 2010). The RCMs in Figure (3.1) are employed at the continental spatial scale, however, RCM domains can be chosen to be much smaller. Over the polar regions, the most widely used RCMs are RACMO (Noël et al. 2018), MAR and HIRHAM (Mottram et al. 2017; Fettweis et al. 2013a), but also other groups are developing polar RCMs, sometimes directly taken from LAMs (e.g. Polar-WRF (Hines et al. 2008)). One of the main advantages of developing an RCM for a specific region is that the physical core of the model can be adapted to the specific region. Over polar regions, RCMs are often coupled to snow models and surface schemes to simulate a realistic ice sheet surface mass balance (Noël et al. 2018; Mottram et al. 2017; Fettweis et al. 2013a). The latest development of RCMs, coupled with ocean, ice sheet and vegetations schemes, can transform RCMs into regional Earth system models. Conversely, GCMs cannot be tuned for specific sub-regions of the Earth, because their main purpose is study the large-scale climate dynamics at the scale of multiple 1000 km.

The main method of RCMs is called "downscaling" (Rummukainen 2010; Laprise 2008). The primary advantage of it is to extract local to regional details from sparse and heterogenously spaced in-situ observations (e.g. weather stations on the GrIS) or from model simulations on a coarse grid. Overall, there are two approaches for downscaling of coarse climate data: statistical and dynamical downscaling.

Statistical downscaling uses large-scale variables (e.g. sea level pressure) and its correlation to other parameters to produce local-scale climate variables (e.g. precipitation on a more realistic topography) (Rummukainen 2010). However, this only works well for areas and variables which have a clear correlation with other large-scale parameters (e.g. a strong height dependency). If, for example, temperature has a strong height dependency, the knowledge about the temperature gradient with height can be used to downscale the temperature information on a higher resolution topography (Noël et al. 2016).

Conversely, RCMs use an approach called dynamical downscaling. Hereby, RCMs are a physical based interpolator (a "magnifying glass") using similarly or more complex physics than GCMs (Rummukainen 2010). Using these complex model physics, RCMs create climate variables at a much higher spatial resolution and over a more realistic topography by solving the main physical principles of the atmosphere at a higher spatial resolution. However, a similar approach has only very recently also been proposed for GCMs over polar ice sheets (Van Kampenhout et al. 2019). Modelling groups have recently started to develop GCMs with a variable grid-spacing with higher resolution over the area of interest to effectively mimick the RCMs downscaling technique (Rummukainen 2010; Van Kampenhout et al. 2019). However, normally the computational costs of GCMs with variable grid spacing are higher than running a normal GCM followed by an RCM (Rummukainen 2010). Whether it is in-

dicated to employ statistical or dynamical downscaling strongly depends on the scientific question, the computational resources available, the considered time frame and the data availability."

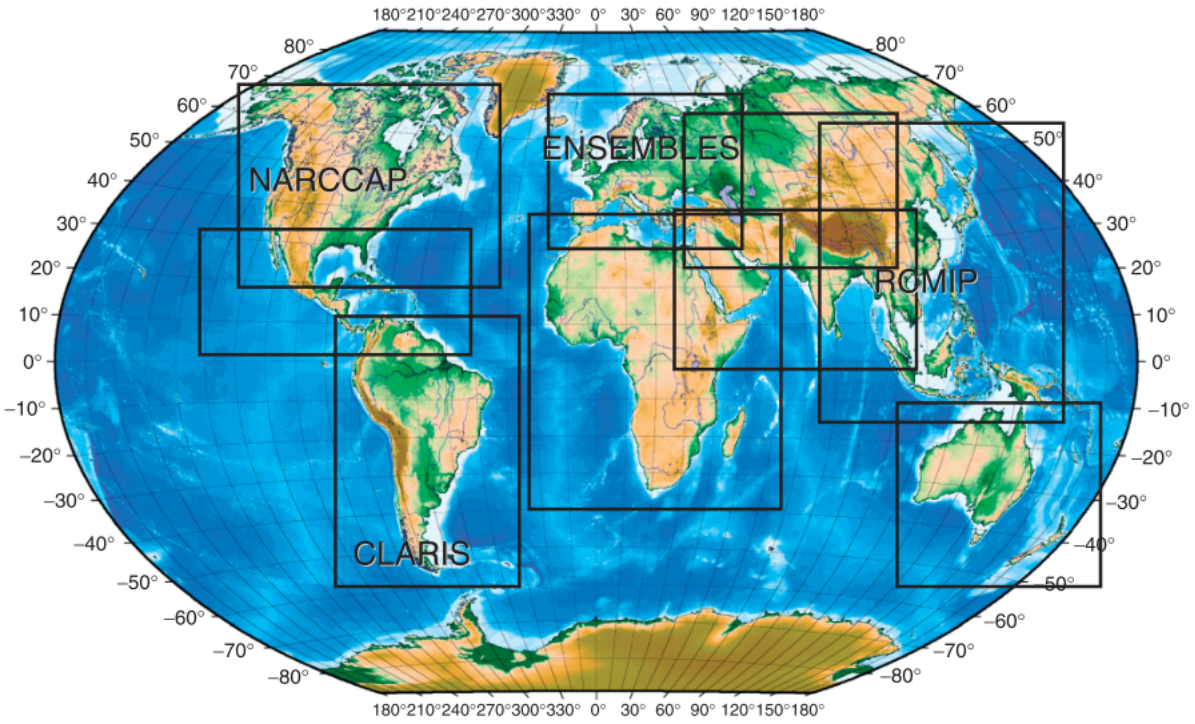

Figure 3.1: **Nesting of regional climate models within a global climate model used as lateral boundary conditions (Rummukainen (2010), p.84).**

The data used for downscaling with an RCM can come from observations, GCMs (historical and future projections), reanalysis datasets (hindcasts) or from coarser RCM simulations ("nesting"). The driving input is prescribed as lateral boundary conditions and often also at the sea surface-atmosphere interface (Rummukainen 2010). The lateral forcing fields for an RCM usually include temperature, moisture, wind and atmospheric pressure, and in the polar RCM case also sea ice concentration and sea surface temperature.

RCMs ability for dynamical downscaling is usually validated with "perfect simulations", where the RCM is forced in hindcast mode with reanalysis datasets, which contain observations from most available sources (Dee et al. 2011; Rummukainen 2010). These perfect simulations are then compared to (independent) observations to allow for efficient tuning of the RCM's model physics.

RCMs usually downscale their forcing fields to a resolution between 10-50 km, but recently also higher-resolution non-hydrostatic RCMs have been developed (Rummukainen 2010). However, there is a limit to the difference in resolution between input and output grid of the RCM. This difference is usually a 6-8 times higher resolution than the prescribed lateral

boundary conditions, at higher resolutions the RCM can become mathematically unstable (Rummukainen 2010). Over the polar regions one new approach is to dynamically downscale large-scale atmospheric input (e.g. to 11 km), and then to apply statistical downscaling techniques (e.g. height dependency of temperature) to create output on a 1 km resolution topography (Noël et al. 2016).

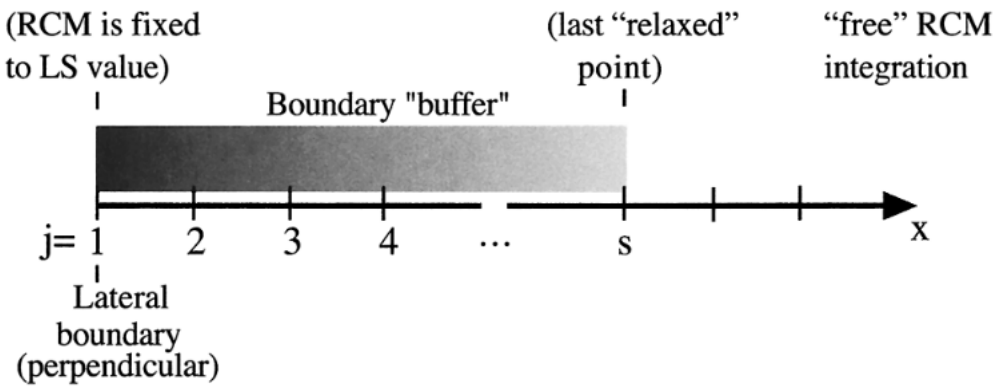

Figure 3.2: **The relaxation zone approach between large scale forcing fields and free regional climate model integration domain (Marbaix et al. (2003))**

An important factor for accurate RCM simulations is the choice of model domain. Depending on the general synoptic circulation, information from the lateral boundary conditions can be advected into the RCM domain from downstream, or transported out of the domain upstream of the main area of interest. To avoid numerical instabilities, most RCMs usually contain a relaxation or sponge zone at the boundaries, which adjusts the weighting of the meteorological input from the forcing fields to the RCMs own solution from 100% to 0% and vice versa (Fig.(3.2)) (Rummukainen 2010). In most RCMs these relaxation zones are 4-10 pixels wide (Rummukainen 2010). The weighting function between the large scale forcing fields at j=1 in Figure (3.2) and the last relaxed point (j=s) can be of various complexity, starting at a simple linear equation (Marbaix et al. 2003; Rummukainen 2010).

Additionally, model domains are chosen in a way that there are no or little topographic features around the lateral boundaries, leading to an undisturbed and uniform synoptic-scale inflow into the integration domain (Rummukainen 2010). The domain extent should be large enough to create an adaptation of meteorological features to local topography (e.g. precipitation along mountain range), but small enough that the synoptic-scale circulation patterns don't deviate from the underlying climate input (Rummukainen 2010; Leduc et al. 2009).

Over polar and often ice-covered regions the domain size can become a problem, especially over Antarctica if the RCM is run over the entire continent (Agosta et al. 2019; Kittel et al. 2018). In these cases, the RCM runs are performed at a much lower resolution than the input grid spacing would allow due to computational costs (Kittel et al. 2018). Furthermore,

over such a large domain, the forcing fields can also be prescribed inside the model domain (Agosta et al. 2019; Kittel et al. 2018), often done as a "spectral nudging" (Rummukainen 2010; Storch et al. 2000). Nudging prevents the RCM solution from diverging from the input circulation state, but can also introduce new biases, so the strength and parameters of the nudging need to be carefully evaluated (Storch et al. 2000; Rummukainen 2010). All these factors mean that chosing a model domain is an important step in the development of a (polar) RCM.

RCMs can offer a wealth of potentials but also face some problems that need to be considered. The main benefit compared to general circulation models is the higher model resolution. Therefore, RCMs represent the interaction between the atmospheric flow and topographic features in greater detail, leading to more realistic precipitation patterns and extremes, but also enhance the accuracy of temperature and wind patterns (Rummukainen 2010). But the smaller domain size and computational costs also allow the implementation of more realistic physics.

Polar RCMs offer the benefit of a realistic snow and surface vegetation scheme, leading to improved snowpack properties (albedo, snow accumulation, melt, runoff). RCMs over the polar regions have two main applications: (1) The downscaling of coarse reanalysis fields to create a physically accurate representation of the current climate of the major ice sheets. (2) The regional downscaling of future projections from GCMs (RCP scenarios (Knutti et al. 2013)) to assess the contribution of the GrIS and the Antarctic Ice Sheet to future sea level rise (e.g.(Fettweis et al. 2013b; Fettweis 2007)). However, especially over Antarctica, RCMs have great computational costs when run at high resolution and are therefore not yet being implemented at the same resolution as GrIS RCM simulations (Fettweis et al. 2017; Noël et al. 2018; Agosta et al. 2019).

Furthermore, RCMs are highly dependent on the quality of their input fields (Rummukainen 2010). Therefore, it might be advisable to only consider thouroughly validated reanalysis data in hindcast mode (e.g. ERA-Interim(Dee et al. 2011)). For the downscaling of future projections over the GrIS and AIS, the most succesful approach might be to use multiple GCM simulations to cover the whole range of climate variability, similar to a "Poor Man's ensemble" approach in numerical weather prediction (Ebert 2001; Fettweis et al. 2013b).

3.3 The regional climate model MAR

3.3.1 General setup

The polar RCM used throughout this thesis is called MAR (Modèle Atmosphérique Régional). MAR consists of two main components: A three-dimensional atmospheric model described

and developed by Gallée et al. (1994), and a one-dimensional surface and vegetation model called SISVAT (Soil Ice Snow Vegetation Atmosphere Transfer), which is interactively coupled to the atmospheric model component (Fettweis et al. 2017; Fettweis et al. 2013a; Hofer et al. 2017). Recently, MAR has been coupled to the ocean model NEMO (Madec et al. 2015) for first test simulations, and will furthermore be coupled to the ice sheet model GISM (Goelzer et al. 2018), with the aim of creating a fully-coupled regional earth system model.

The atmospheric model in MAR itself consists of multipe components to describe the radiative fluxes, boundary layer turbulence, clouds and aerosols. The main atmospheric component to model the large-scale atmospheric dynamics was developed by Gallée et al. (1994), Gallée (1995), and Gallée et al. (2014). The first description of MAR in the literature was only five years after the first historical RCM studies in 1989 (Dickinson et al. 1989; Giorgi et al. 1989). While initially it was mainly used over polar regions (Gallée et al. 1994), it is now widely adopted over Africa and Europe as well (e.g. (Wyard et al. 2018)).

The atmospheric component is a hydrostatic model that solves the primitive equation set (Gallée et al. 1994), while the vertical coordinates are terrain-following sigma coordinates, obtained by normalizing between the top and surface pressure of the model (see eq.(3.1)). Note however, given the distribution of the sigma layers in MAR, the model does not resolve the stratosphere and is therefore considered to be a "low top" model.

$$\sigma = \frac{p - p_t}{p_s - p_t} \tag{3.1}$$

The radiative fluxes in the shortwave and longwave part are based on the ECMWF ERA-40 radiative scheme, partly described by Morcrette (2002). This radiative scheme uses time-varying atmospheric aerosol concentrations from monthly means, using the input data described in Tegen et al. (1997). However, given that the output of MAR is on a daily timestep, using monthly aerosol loads in the radiative scheme likely leads to the omission of radiatively important shorter aerosol advection events towards the GrIS (e.g. wildfires in Canadian Arctic). The near-surface turbulence, essential for the turbulent heat transfer, is modelled following the turbulence closure model of Duynkerke (1988).

SISVAT

The component to model the exchange between the atmosphere and the surface in MAR is called SISVAT (Soil Ice Snow Vegetation Atmosphere Transfer). It is a one-dimensional, multi-layered surface module, subdivided into a soil-vegetation module and a snow-ice module (SISVAT is described in De Ridder et al. (1998)).

The vegetation module consists of 12 different plant types, characterized by their main physical properties such as height, roughness length, root fraction and stomatal resistance. The vegetation module also consists of four different soil types which differ for example by their water content at saturation and water retention properties. Every pixel in the MAR SISVAT module can have three sub-pixels, land, sea or ice/snow. Based on all of these physical properties, SISVAT computes the heat and moisture fluxes between the troposphere and the surface.

More important for studying polar climates however is the snow-ice module in SISVAT, which is based on the snow model CROCUS (Brun et al. 1992; Vionnet et al. 2012). The snow model CROCUS itself defines the main snow properties and its temporal evolution, which are highlighted in Figure (3.3). Prognostic variables in CROCUS are related to the snow grain metamorphism, where the size, dendricity, sphericity and grain size are explicitly modelled (Vionnet et al. 2012). Additionally, CROCUS also forecasts the evolution of the snow heat content, temperature and the liquid water content stored within the snowpack. MAR is interactively coupled to the snow scheme and therefore allows for a direct, two-way feedback between atmospheric variables and the snowpack properties (Vionnet et al. 2012; Brun et al. 1992).

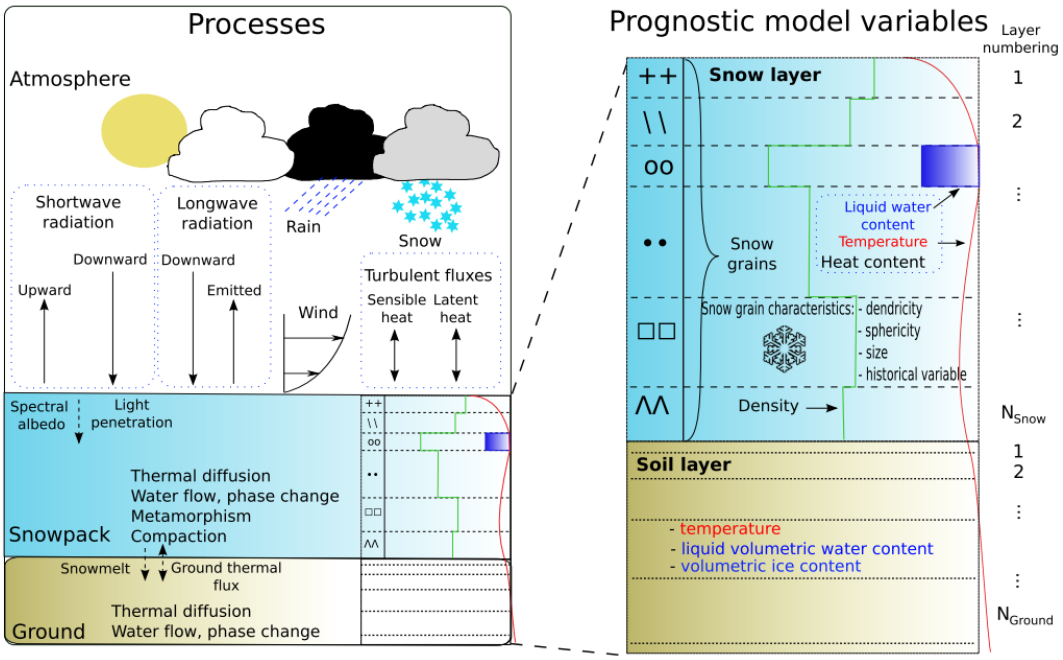

Figure 3.3: **Main physical processes and prognostic variables within the snow model CROCUS (Vionnet et al. (2012), p.774).**

Cloud microphysical scheme

Cloud microphysical schemes have great control over the accuracy of regional climate models. They describe the complete hydrological cycle, from water vapour to the formation of falling precipitation (Gallée 1995). Additionally, due to the interaction of dispensed particles with shortwave and longwave radiation, cloud microphysical schemes are also one of the most essential physical schemes for controlling the surface energy budget (Morrison et al. 2005a).

Additionally, the hydrometeors (liquid or solid water particles suspended in the atmosphere) parameterized by the cloud microphysics scheme also act as an essential component in the non-radiative atmospheric energy fluxes. During condensation of water vapour to (cloud) droplets latent heat is released, warming the surrounding atmosphere and decreasing the atmospheric temperature lapse rate (Morrison et al. 2005a). Conversely, when falling precipitation (snow/rain/graupel) evaporates or sublimates, energy from the surrounding atmosphere is used to break up the bonds between H_2O molecules, effectively cooling the surrounding air.

Therefore, the representation of hydrometeors in climate models not only highly influences the surface energy budget, but also the vertical temperature distribution and therefore the vertical stability and subsequent vertical motion in the atmosphere (Lee et al. 2018). Lastly, due to the interaction of hydrometeors with their surroundings (e.g. surface energy budget, precipitation, temperature distribution) the circulation from the micro- and mesoscale to the synoptic scale can be influenced by differences in the modelling of water in the atmosphere (Morrison et al. 2005a; Lee et al. 2018).

Most climate models parameterize the cloud microphysics with either one- or two-moment microphysical schemes. One-moment schemes solve one microphysical equation prognostically (one moment of the particle size distribution, mostly the mixing ratio), while two-moment schemes solve two equations prognostically (mostly mixing ratios and number concentration).

One- and two-moment schemes both use similar numerical equations (see equations (3.2)-(3.4)) to predict the temporal evolution of the overall mixing ratios (g/kg or kg/kg) for up to 6 species of water and ice particles in the air, in addition to the conservation of specific humidity (Morrison et al. 2005a; Morrison et al. 2005b; Morrison et al. 2009; Morrison et al. 2011; Lee et al. 2018; Gallée 1995). The species for which the temporal evolution of their mixing ratio is predicted may contain snow, rain, cloud droplets, cloud ice, graupel and hail (Morrison et al. 2005a; Lee et al. 2018; Gallée 1995). However, one-moment schemes assume an underlying shape of the distribution of the particle size distribution (similar to Fig.(3.4)) for which they mainly solve analytical equations (Morrison et al. 2005a; Morrison

et al. 2005b; Morrison et al. 2009; Morrison et al. 2011; Lee et al. 2018). Two-moment schemes on the other hand predict two "moments" of the particle size distribution, mostly adding the number concentration (particles/m^3) to the predicted variables. Therefore, two-moment schemes are adding a second degree of freedom to the particle size distribution, potentially adding higher accuracy to the size distribution of cloud and precipitation particles (Morrison et al. 2005a).

However, most microphysical schemes in current climate models are "bulk" schemes, meaning that both one- and two- moment schemes have to assume an underlying functional relationship for the particle size distribution (Morrison et al. 2009). Fig.(3.4) right column shows such an assumption, where the particle size distribution function (N(D) is the number of given diameter (D) per volume (m^3)) is assumed to have the shape of an inverse exponential function.

Some research models employ "bin" microphysical schemes that allow for a different parameterization for each "bin" of potential particle sizes (Fig.(3.4), left), theoretically allowing models to capture more arbitrary particle size distributions (Lee et al. 2018). However, bin models are not used in many operational weather forecasting and climate models, because of their higher computational costs (Morrison et al. 2005a; Lee et al. 2018).

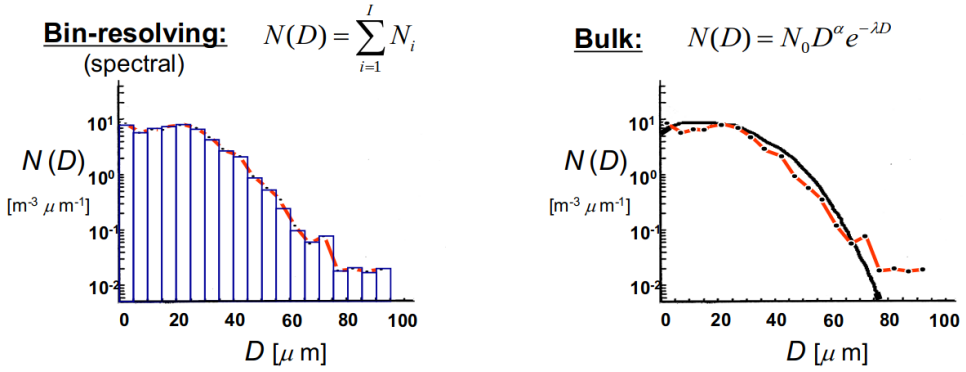

Figure 3.4: **Difference in particle size distribution between bin and bulk microphysical schemes (Milbrandt et al. (2015))**. Particle size distrbution in bin-resolving microphysical schemes (left) and bulk microphysical schemes (right).

The hydrological cycle in MAR is parameterized as a single-moment microphysical scheme, fully descibed in Gallée (1995). The cloud microphysical scheme in MAR is based on the pioneering work of Kessler (1995), dating back to the 1960s, but also on more recent studies by Lin et al. (1983), Meyers et al. (1992) and Levkov et al. (1992). It solves the prognostic mass conservation equations (Eq.(3.2)) for four different water and ice particle species, in addition to the conservation of the specific humidity (i.e. water vapour) (Gallée 1995). The prognostic equations numerically forecast the mixing ratio for cloud droplets (q_l), cloud ice (q_i), rain (q_r) and for snow (q_s) (Gallée 1995). For the mixing ratio of the specific humidity,

liquid cloud droplets and ice cloud crystals, the conservation equations have the form of

$$\frac{\delta q_\alpha}{\delta t} + \vec{v} \cdot \nabla q_\alpha = F_{q\alpha} + P_{q\alpha}, \tag{3.2}$$

where α can be cloud ice (i), cloud liquid water droplets (l) or water vapour (v), F is the divergence of the turbulent flux of the specific humidity or cloud droplet concentration and P is a source term (Gallée 1995). In addition, the nabla operator, the 3-dimensional vector differential operator, can be extended to yield the common form of the advection of one of the cloud species (l, i and water vapour) by the 3-D wind vector given as

$$\frac{\delta q_\alpha}{\delta t} = -u \cdot \frac{\delta q_\alpha}{\delta x} - v \cdot \frac{\delta q_\alpha}{\delta y} + \dot{\sigma} \cdot \frac{\delta q_\alpha}{\delta \sigma} + F_{q\alpha} + P_{q\alpha}, \tag{3.3}$$

with the slight amendment to express the vertical velocity on the terrain following σ-coordinates as $\dot{\sigma}$ (Gallée 1995). For the precipitating hydrometeors, i.e. rain and snow, a source/sink term due to the terminal velocity related falling speed of the species (sedimentation, P_{sed}), yielding a conservation equation of the form

$$\frac{\delta q_\alpha}{\delta t} = -u \cdot \frac{\delta q_\alpha}{\delta x} - v \cdot \frac{\delta q_\alpha}{\delta y} + \dot{\sigma} \cdot \frac{\delta q_\alpha}{\delta \sigma} + F_{q\alpha} + P_{q\alpha} + P_{sed}. \tag{3.4}$$

The MAR models solves these conservation equations of the microphysics scheme on every x and y point (horizontal plane) and for every vertical σ-layer (Gallée 1995).

The microphysical scheme equations describe the base set of the mathematical formulation prescribed in the model physics (Gallée et al. 1994; Gallée 1995). However, since the development of the MAR model in the 1990s (Gallée et al. 1994), the model parameters have been modified and tuned, such that observations of radiation and clouds over polar regions are accurately reproduced (Fettweis et al. 2011; Fettweis et al. 2013a; Hofer et al. 2017). For example, one of the most efficient ways of tuning the surface energy budget and the precipitation patterns is by modifying the lifetime of clouds. Additionally, more subtle tuning can be achieved by enhancing or reducing the efficiency of the Bergeron-Findeisen process, which describes the rate at which ice particles grow at the expense of liquid particles.

The cloud microphysical scheme in MAR is closely connected to the radiative scheme. The MAR cloud microphysical scheme computes the cloud optical thickness at each grid point and for every vertical sigma level, which it then passes on to the radiative scheme to compute the radiative fluxes in the shortwave and longwave part. The cloud optical thickness in MAR is defined as

$$\tau = \frac{3}{2} \cdot \frac{W}{r_e}, \tag{3.5}$$

where W is the total water path ($W_{ice} + W_{water}$) and r_e are the effective radii of the suspended

water or ice particles (Gallée 1995). In MAR, the effective radius is defined as

$$r_e = x \cdot r_w + (1-x) \cdot r_i \,, \tag{3.6}$$

where x is the liquid water path divided by the total water path (ice+liquid), defined as $x = W_w/W$. In the earliest development of MAR (Gallée et al. 1994; Gallée 1995), the effective radii for water and ice, r_i and r_l, were prescribed at r_i=40 μm and r_w=20 μm. However, in the latest versions these parameters are used as one of the many tuning parameters in the model to most closely match observations of the surface energy budget, melt and surface mass balance.

Furthermore, the cloud emissivity in MAR is parameterized by the following equation

$$\epsilon = 1 - exp(-C_e \cdot W), \tag{3.7}$$

where C_e is equal to

$$C_e = 0.13 \cdot x + 0.05 \cdot (1-x) \tag{3.8}$$

and W is the total water path ($W_{ice} + W_{water}$) and x is the fraction between liquid water path and total water path, $x = W_w/W$.

One part of MAR's cloud microphysics scheme that might have to be improved in the future is its treatment of aerosols as cloud condensation nuclei. The cloud microphysical scheme in MAR uses constant aerosols loads, neglecting the interannual variability in aerosol impacts upon cloud lifetime and albedo (Ackerman et al. 2000; Stevens et al. 2009). Therefore, the feedback between changes in aerosol concentration and clouds is not accounted for in MAR.

3.3.2 MAR Greenland setup

The MAR model setup in this thesis is in parts adapted to the Greenland Ice Sheet (grid extent, projection and resolution), but the model physics remain unchanged. The GrIS integration domain is shown in Fig.(3.5), together with the surface height above sea level in meters. The integration domain covers an area of 6.75 mio. km^2, between -88.4°W and 5.1°E (longitudinal extent) and 54.89°N and 85.92°N (latitudinal extent).

Two different horizontal grid spacings were used: 25 km and 15 km. The 25 km resolution domain covers 80 pixels in the east-west direction and 135 in the north-south direction (10800 gridpoints), while the finer 15 km resolution has an extent of 115 (E-W) and 210 (N-S) pixels (24150 pixels). The integration time step for the numerical approximations of the differential equations in MAR depends on the resolution. Therefore, we set the time step to 150s at 25 km and to 90s at 15 km grid spacing. We ran the MAR model with 24 vertical terrain-following sigma coordinate levels and we set the highest sigma level to a pressure of

0.1 hPa. The snow model component of MAR, which is based on the snow model CROCUS (Vionnet et al. 2012), encorporates 30 active layers in the snowpack. We ran the land-based component of MAR in SISVAT, used to model the soil properties over Greenland's tundra, with 7 active soil layers.

Additionally, the (lateral) boundary conditions are prescribed at 6h intervals to prevent the RCM from developing a fully independent climate, which can lead to signficant biases. MAR can be flexibly used with various forcing datasets: (1) Reanalysis datasets, for example ERA-Interim or NCEP reanalysis and (2) General circulation models of varying complexity and different greenhouse gas emission scenarios.

MAR requires 6-hourly information about the specific humidity, u- and v- wind component, temperature and sea level pressure. At the surface-ocean interface, MAR also requires daily information about the sea surface temperature and sea ice concentration.

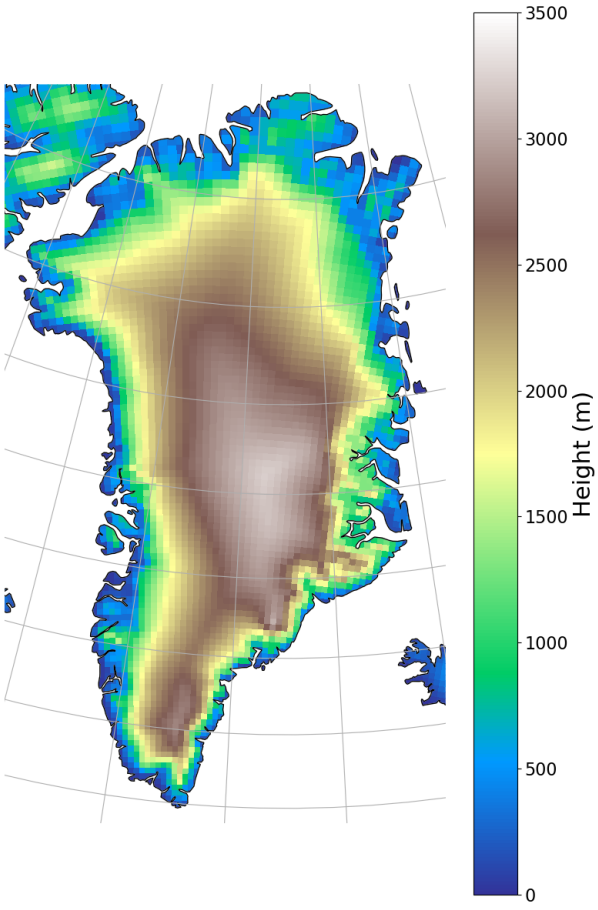

Figure 3.5: **The MAR integration domain over Greenland at 25 km horizontal resolution.** Color shading indicates height above sea level in the MAR integration domain.

3.4 Observations of the GrIS climate system

3.4.1 PROMICE in-situ observations

The Programme for Monitoring of the Greenland Ice Sheet (PROMICE) is an extensive network of weather stations on the Greenland Ice Sheet (As et al. 2011). The network started in 2007 with 5 automatic weather stations (AWS) and by 2010 already consisted of 14 AWS (As et al. 2011). Now, the in-situ climate and weather station network contains 23 AWS weather stations, located around the margins of the Greenland Ice Sheet (see also Fig.(3.6))(As et al. 2011). Usually, each region has at least two stations (orange dots in Fig.(3.6)), one located in the lower areas of the ice sheet in the ablation zone (denoted as "_L") and one in the upper parts near or in the accumulation zone (denoted as "_U") (As et al. 2011). However, some of the transects can consist of up to 4 stations, for example in the Kangerlussuaq area, but also along the Nuuk transect. The PROMICE AWS record at a temporal sampling rate of 10 minutes (As et al. 2011). The data are transmitted every hour during summer, but due to lower solar energy availability only once per day during winter. The data can be accessed in real-time and for free via www.promice.dk (As et al. 2011).

The PROMICE AWS usually report the following climate and weather variables (numbers refer to the picture of a PROMICE AWS in Fig.(3.7)) (As et al. 2011): (1) One upward- and one downward facing shortwave radiometer and a similar setup with one upward- and one downward facing longwave radiometers. (2) An inclinometer to measure the angle between the surface and the radiometers. Inclinometer readings are essential to correct radiation and albedo measurements. (3) Satellite antenna for data transfer. (4) Anemometer to measure wind speed and direction. (5) Ultrasound (sonic) height ranger which measures the time an ultrasonic signal travels from the sensor to the ice surface and back to the sensor. The travelling time can be used to measure the distance between sensor and surface, and therefore ice/snow accumulation rates (or snow compaction). (6) Thermometer (temperature) and hygrometer (humidity) sensors. (7-11) Additional equipment for battery storage and englacial sensors (As et al. 2011).

Overall, the PROMICE data network provides valuable input for validation studies of regional climate models over the Greenland Ice Sheet. I use the PROMICE data extensively in Chapter 4, where I validate two regional climate models agains in-situ and remote sensing observations of the Greenland climate system.

However, in-situ observations also contain some limitations when they are being used to validate regional climate model data (Ryan et al. 2017; Wang et al. 2016). First, most of the weather stations are only located along the margins of the Greenland Ice Sheet, with a higher density in the proximity of major Greenlandic towns (e.g. Nuuk, Kangerlussuaq). While most of the observation areas are designed as transects from the lower ablation zone

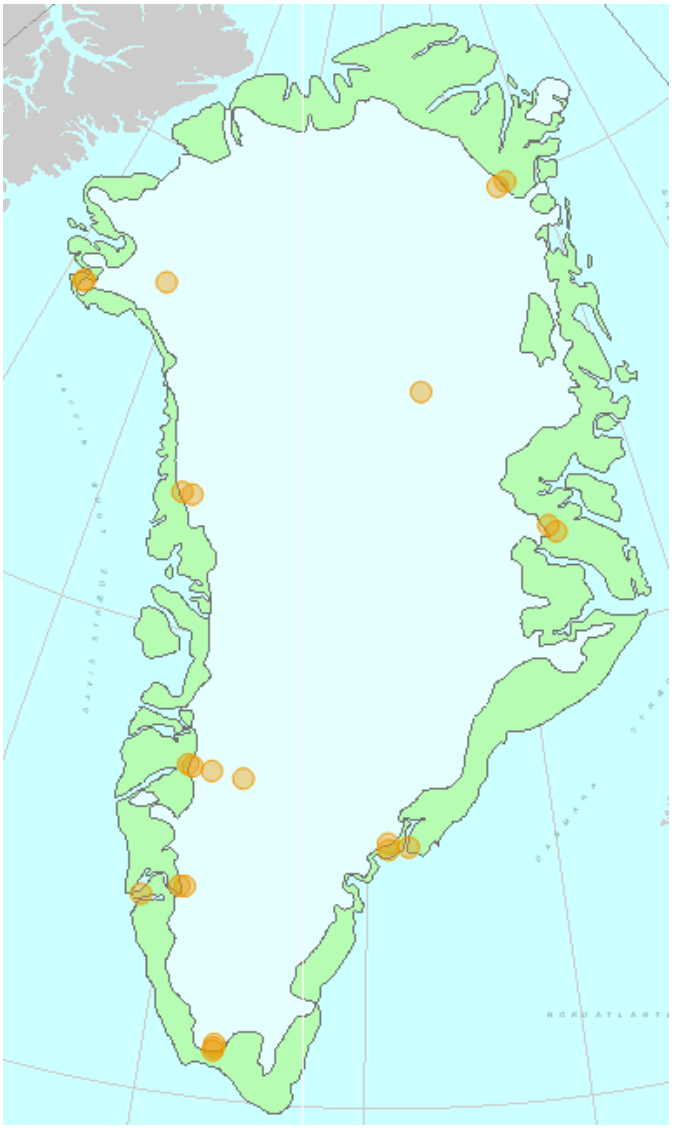

Figure 3.6: **Map of all the PROMICE weather stations over the Greenland Ice Sheet (As et al. (2011)). Figure adapted from https://www.promice.dk/CurrentWeatherMap.html. (PROMICE 2019)** The map of Greenland shows the locations of all the PROMICE weather stations. Altogether, the PROMICE network consists of 23 AWS stations across the Greenland Ice Sheet (As et al. 2011).

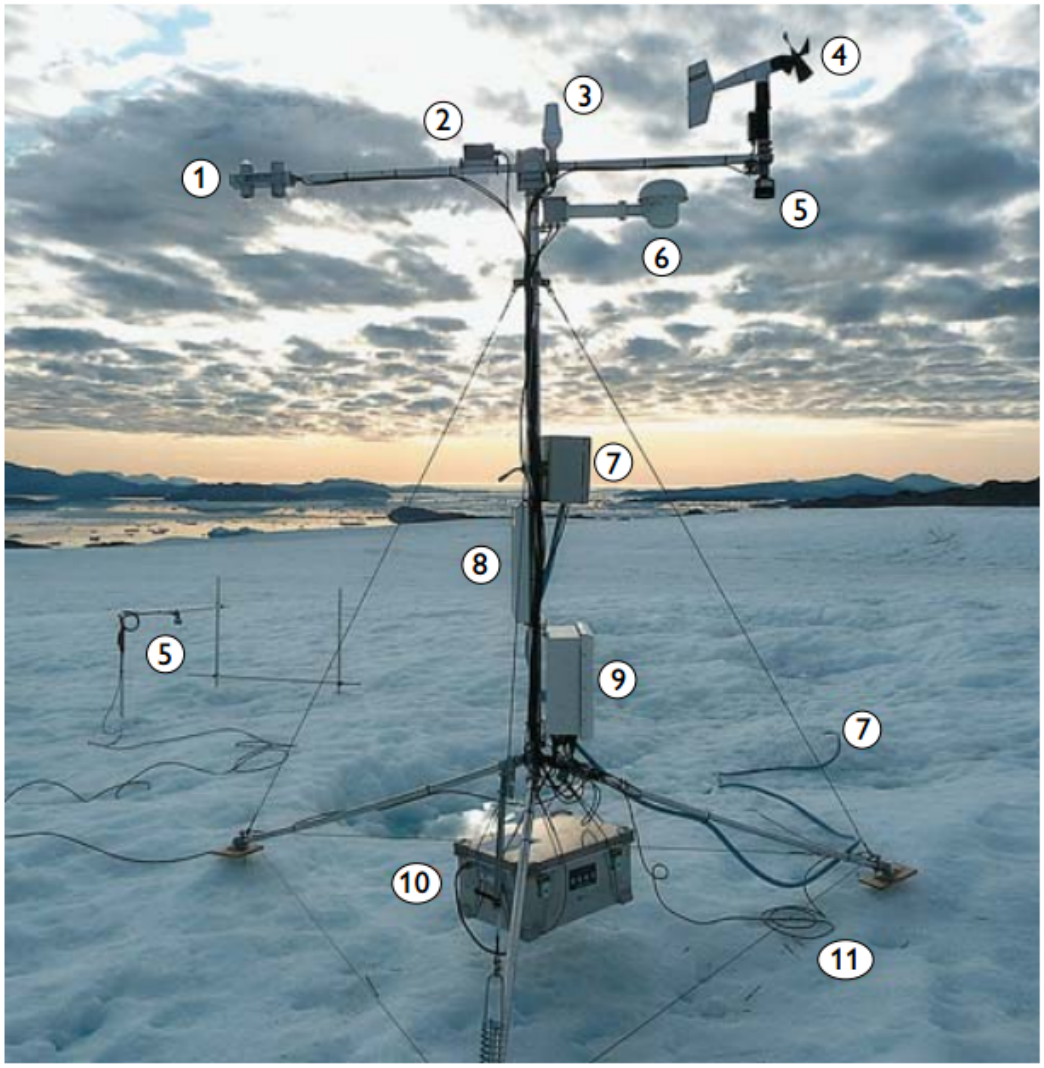

Figure 3.7: **Picture of a typical PROMICE weather station on the Greenland Ice Sheet (As et al. (2011), p.74.)** PROMICE automatic weather station UPE_L photographed on 17 August 2009 (As et al. 2011). 1: radiometer. 2: inclinometer. 3: satellite antenna. 4: anemometer. 5: sonic height rangers. 6: thermometer and hygrometer. 7: pressure transducer. 8: solar panel. 9: data logger, barometer and GPS. 10: battery box with 4×28 Ah batteries. 11: 8-level thermistor string

to the accumulation zone, very few stations are located in the interior of the ice sheet. Therefore, models might perform well over areas that are most important for melt and where most weather stations are located (i.e. the ablation zone), while it is almost impossible to validate a model's performance over the accumulation zone due to a lack of observations.

Second, even within the ablation zone there is a strong spatial heterogenity in terms of surface topography and climate, which might limit the ability to use in-situ point observations to upscale to the model pixel scale (Ryan et al. 2017). The roughness of the surface usual increases towards the lower ablation zone, where crevasses and melt-induced hummocking is abundant. Therefore, for example the point albedo measurement in areas with great surface roughness not be representative for one model pixel at the scale of approximately 10 by 10 km (Tedstone et al. 2017; Ryan et al. 2017). The same holds also true when trying to upscale other meteorological parameters from point observations, such as wind and temperature.

Third, due to its remote locations, in-situ weather stations over Greenland often remain unattended for one entire year (Wang et al. 2016). Therefore, weather stations and the accuracy of their sensors might be impeded by various influences during the year: (1) Riming on radiation sensors can lead to inaccurate radiative flux measurements, (2) due to unequal surface lowering the stations might start to tilt, leading to false reading on the shortwave radiometers, (3) riming on the wind sensors might reduce the measured wind speed and (4) lowering of the entire weather station might lead to a drift in all height-dependent measurements such as temperature, humidity and wind speed/direction. (Wang et al. 2016). Therefore, one needs to cautiously remove spurious readings from the in-situ observations when trying to assess the accuracy of regional climate models.

3.4.2 Satellite remote sensing

In this thesis, satellite remote sensing data are used to evaluate the capabilities of polar regional climate models to reproduce observed trends in cloud cover (Hofer et al. 2017). For this reason, AVHRR and MODIS data are used to compare the changes in observed cloud properties between 1982 and 2015 (AVHRR) and 2002 and 2015 (MODIS) to our regional climate model outputs. During these periods, the sensors have been carried on multiple different satellites and have undergone significant development (more spectral bands) to evaluate the Earth's cloud properties. Additionally, the algorithms that are used to retrieve these data have also been developed significantly. Therefore, this following section will establish how cloud detection in AVHRR and MODIS works, what spectral information is being used and what shortcomings these passive sensors have in high-latitudes.

AVHRR

For parts the following two subsections ("AVHRR" and "MODIS") have been published in the "Materials and Methods" section of Hofer et al. (2017) on page 6.

The Advanced Very High Resolution Radiometer (AVHRR) has been used on several polar-orbiting NOAA (NOAA-07, 09, 11, 12, 13, 14, 15, 16, 17,18, 19) and EUMETSAT's MetOp-A and MetOp-B satellites. Over the years, the AVHRR sensor underwent important improvements: AVHRR/1 only used four spectral channels (1978-1982), AVHRR/2 added a fifth channel (1982-1998) and with AVHRR/3 even a sixth band was added (1998-now, Fig.3.8, Fig.3.9) (Karlsson et al. 2016). At Nadir, the AVHRR sensor has a nominal resolution of 1 km (Karlsson et al. 2016). However, global data of the sensor have only been archived at 4 km since the beginning of the measurement period (Karlsson et al. 2016). The length is furthemore restricted to a start date of 1982, because the cloud retrieval depends on the availability of two infrared channels, centered at a wavelength of 11 (10.5-11.5) and 12 (11.5-12.5) microns (channels 4+5 Fig.(3.8)) (Karlsson et al. 2016). Therefore, for cloud retrievals, only data from AVHRR/2 and AVHRR/3 was used in the CLARA-A1 and CLARA-A2 datasets in this thesis.

Channel Number	Wavelength (micrometers) AVHRR/1 NOAA-6,8,10	Wavelength (micrometers) AVHRR/2 NOAA-7,9,11,12,14	Wavelength (micrometers) AVHRR/3 NOAA-15,16,17,18,19 Metop-A/B
1	0.58 - 0.68	0.58 - 0.68	0.58 - 0.68
2	0.725 - 1.10	0.725 - 1.10	0.725 - 1.10
3A	-	-	1.58 - 1.64
3B	3.55 - 3.93	3.55 - 3.93	3.55 - 3.93
4	10.50 - 11.50	10.50 - 11.50	10.50 - 11.50
5	Channel 4 repeated	11.5 – 12.5	11.5 – 12.5

Figure 3.8: **Overview of the AVHRR sensor channels and corresponding wavelengths (Karlsson et al. (2016), p.10).** The first column denotes the channel number, the second column describes the corresponding channel wavelength for the first version of the AVHRR sensor (AVHRR/1) and the satellites on which this sensor was mounted. Third column is the same as the second, except that it describes the second version of the AVHRR sensor (AVHRR/2). Fourth column, same as second and third but for the third version of the AVHRR sensor (AVHRR/3).

Figure (3.9) shows that NOAA and MetOp satellites have been split into morning observation nodes and afternoon observation nodes (Karlsson et al. 2016). This setup, for most of the observational period, guarantees that every given location is visited 4 times per day, ap-

proximately 6h apart (polar-orbiting satellites pass the same point again 12h later at night) (Karlsson et al. 2016). However, between 1982 and 1991 only one satellite was available and therefore the temporal sampling rate was lower. More recently, the temporal sampling rate has been higher than the aim of 4 overpasses per day due to the added data from the MetOp satellites (Fig.(3.10)). Furthermore, Fig.(3.9) also shows small problems with keeping the equatorial crossing time stable. However, the data were homogenised to avoid artificial drifting in the resulting CM SAF datasets (Karlsson et al. 2016).

Overall, the CLARA datasets based on the AVHRR sensors provide multiple cloud related parameters such as cloud fraction, cloud optical thickness and cloud top pressure, which were post-processed using the Polar Platform System and the Cloud Physical Properties retrieval technique (Dybbroe et al. 2005b; Dybbroe et al. 2005a; Karlsson 2014).

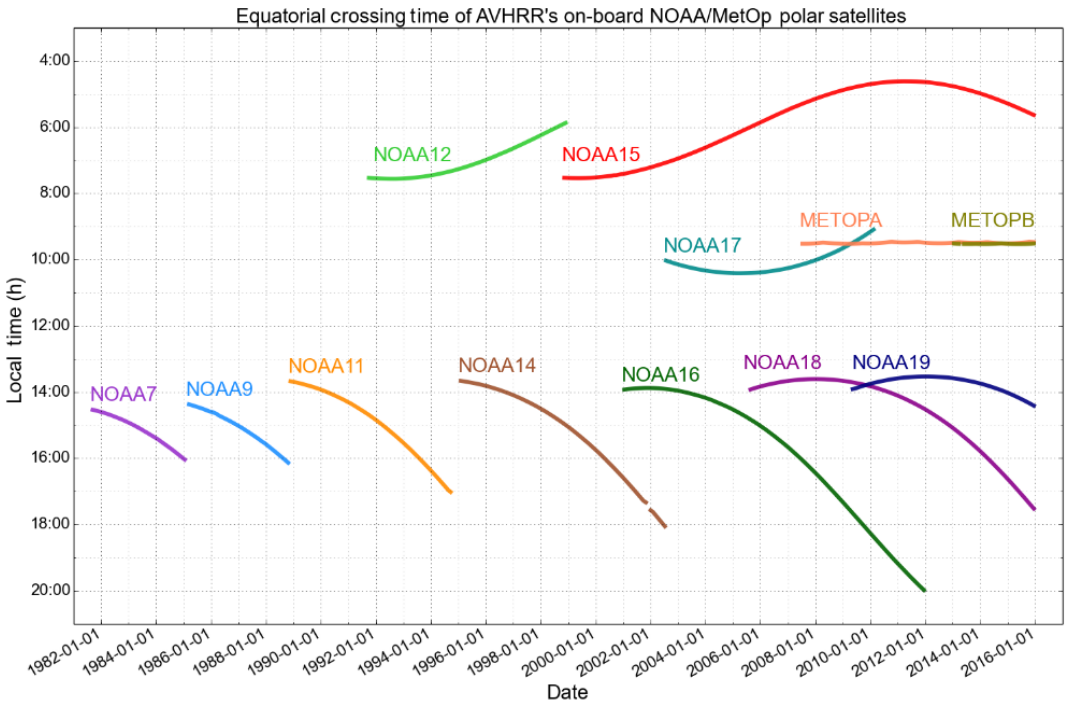

Figure 3.9: **Time series of satellites carrying the AVHRR sensor since 1982 and equatorial crossing time (Karlsson et al. (2016), p.9).** Time series of all NOAA and Eumetsat (MetOp-A and B) satellites used in the CLARA-A2 dataset and the local time (y-axis) when they cross the equator (Karlsson et al. 2017; Karlsson et al. 2016)

In this thesis I used two different AVHRR based datasets (Karlsson 2014; Karlsson et al. 2016; Karlsson et al. 2017). Chapter 5 uses the CLARA-A1 dataset, covering the period from 1982-2009 (Hofer et al. 2017; Karlsson 2014). Chapter 4 (Validation of clouds in regional climate models) uses the newly released CLARA-A2 dataset, spanning the years 1982-2015 (Karlsson et al. 2016; Karlsson et al. 2017). The main improvement between these two datasets is the elongated observational period in the CLARA-A2 data. The retrieval algorithms have only been slightly modified to enhance the calibration of the data, and therefore this is not

expected to affect the conclusions in these chapters (Karlsson et al. 2017).

Both level-3 datasets were evaluated on a 0.25° x 0.25° latitude-longitude grid (as in Hofer et al. (2017)) and were processed by EUMETSAT's Satellite Application Facility on Climate Monitoring in the following way: The level-2 data underlying the level-3 data has a spatial resolution of 0.05° x 0.05° (level-1 data 1-3 km) (Karlsson et al. 2016). The datasets were evaluated with in-situ observations, but were also compared to MODIS satellite data (Karlsson 2014; Karlsson et al. 2017; Karlsson et al. 2016).

The target bias-corrected RMSE for cloud cover data lies between 15 and 20% (Karlsson 2014; Karlsson et al. 2017). The daily fractional cloud cover product is based on the binary cloud mask retrievals (0=clear, 1=cloudy) on the level 2B grid (0.05°), and subsequently computed by aggregating all of the level 2 pixels within one level 3 pixel (0.25°) and dividing the number of cloudy pixels by the total number of retrieved cloud observations (eq.(3.9)) (Karlsson et al. 2016; Karlsson 2014). All of these daily fractional cloud cover observations were then averaged for each month to arrive at the monthly means that were used throughout this study (Karlsson et al. 2016; Karlsson 2014).

$$CFC(i,j) = \frac{N(i,j)_{cloudy}}{N(i,j)_{cloudy} + N(i,j)_{clear}} \tag{3.9}$$

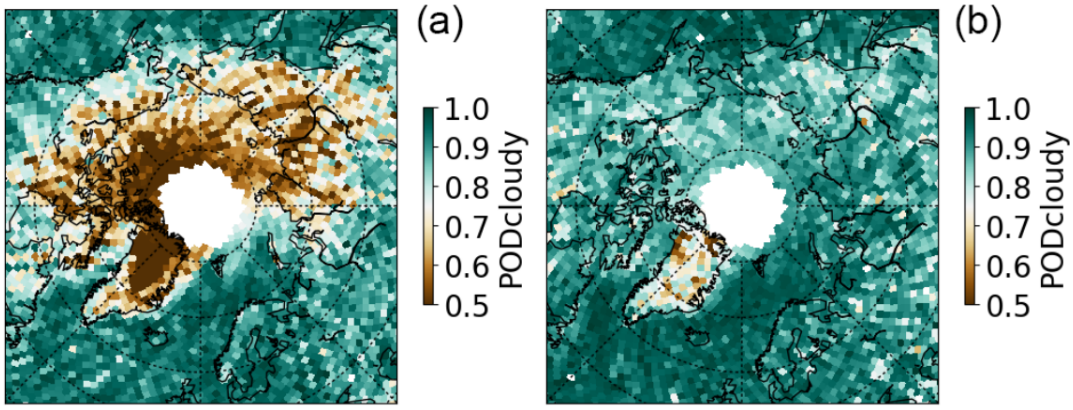

Figure 3.10: **Probability of detection cloudy conditions over the Arctic (Karlsson et al. (2017) p.5814).** a) Cloud detection probability during winter from the AVHRR sensor (CLARA-A2 data). b) Same as a) but for the polar summer (JJA).

MODIS

The Moderate Resolution Imaging Spectroradiometer (MODIS) has been in orbit since 2000 and aboard two satellites, Aqua and Terra (Ackerman et al. 1998). Its cross-track swath

width spans 2330 km and the along-track swath length is 10 km. It makes use of measurements at 36 different wavelengths, ranging from 0.4 to 14.4 mm, of which 14 are used to test whether clouds are present (Fig.(3.11)) (Ackerman et al. 1998; Frey et al. 2008). The tests mostly rely on the contrast between the surface and the clouds above (Ackerman et al. 1998).

Here, we used the global, monthly fractional cloud cover product (MYD08_M3) (Platnick et al. 2015) from the MODIS sensor on board of the polar orbiting Aqua satellite. It was computed by summarizing the daily level 3 product over one calendar month (Hubanks et al. 2008). Cloud fraction within this dataset was defined as the ratio between the sum of cloudy pixels and the total number of pixels within one grid cell. The measurement period available for this study ranged from 2002 to 2015.

The spatial grid of the monthly cloud cover product was an equal-angle 1° longitude by 1° latitude grid, while the daily level 2 product (MOD06_L2) underlying the daily level 3 product had a higher spatial resolution of 1 km (2 channels have a resolution of 250 m, 5 channels have a resolution of 500 m and the rest has a resolution of 1 km) (Hubanks et al. 2008). For every 1° by 1° grid cell, all the underlying level 2 pixels were used to determine the cloud fraction over a period of 1 day and then were averaged over 1 month (Hubanks et al. 2008). For the computation of cloud cover averages over the entire GrIS, data points were weighted on the basis of their latitude to take into account the meridian convergence toward the North Pole, given that the dataset is provided on a latitude-longitude grid.

Cloud detection and problems

The two sensors used in this thesis, MODIS and AVHRR, both use threshold tests to determine the cloud amount (Ackerman et al. 1998; Karlsson et al. 2013; Karlsson et al. 2017; Dybbroe et al. 2005b). The spectral bands used are determined by the specific cloud characteristics, because very thin ice clouds have different optical and infrared properties as for example low-level fog.

For the detection of thick high clouds, simple thresholds of the brightness temperature in the infrared can be used (e.g. 11 μm), while thin clouds are usually detected by taking the difference between two measured brightness temperatures in the infrared part of the spectrum (e.g. MODIS $BT_{11\,\mu m}$-$BT_{3.9\,\mu m}$, equivalent to AVHRR $BT_{11\,\mu m}$-$BT_{3.7\,\mu m}$) (Ackerman et al. 1998; Karlsson et al. 2013; Dybbroe et al. 2005b). Low clouds are usually detected by reflectance thresholds in the visible and near-infrared range (MODIS $r_{0.87\,\mu m}$, $r_{0.65\,\mu m}$, $r_{0.936\,\mu m}$; AVHRR $r_{0.6\,\mu m}$). of by reflectance ratio tests in the visible and near infrared spectrum (MODIS $r_{0.87\,\mu m}/r_{0.66\,\mu m}$, $r_{0.935\,\mu m}/r_{0.87\,\mu m}$; AVHRR $r_{1.6\,\mu m}/r_{0.6\,\mu m}$, $r_{3.7\,\mu m}/r_{0.6\,\mu m}$) and multiple brightness temperature difference tests (MODIS $BT_{3.9\,\mu m}$ - $BT_{3.7\,\mu m}$, these bands are not available in AVHRR) (Ackerman et al. 1998; Karlsson et al. 2013; Karlsson et al.

Band	Wavelength (μm)		Comment
1 (250 m)	0.659	Y	250-m and 1-km cloud detection
2 (250 m)	0.865	Y	250-m and 1-km cloud detection
3 (500 m)	0.470	Y	Smoke, dust detection
4 (500 m)	0.555	Y	Snow/ice detection (NDSI)
5 (500 m)	1.240	Y	Smoke, dust detection
6 (500 m)	1.640	Y	Terra snow/ice detection (NDSI)
7 (500 m)	2.130	Y	Aqua snow/ice detection (NDSI)
8	0.415	Y	Desert cloud detection
9	0.443	Y	Sun-glint clear-sky restoral tests
10	0.490	N	
11	0.531	N	
12	0.565	N	
13	0.653	N	
14	0.681	N	
15	0.750	N	
16	0.865	N	
17	0.905	Y	Sun-glint clear-sky restoral tests
18	0.936	Y	Sun-glint clear-sky restoral tests
19	0.940	N	
26	1.375	Y	Thin cirrus, high cloud detection
20	3.750	Y	Land, sun-glint clear-sky restoral tests Snow/ice, dust detection
21/22	3.959	Y(21)/Y(22)	smoke detection (21)/Cloud detection (22)
23	4.050	N	
24	4.465	N	
25	4.515	N	
27	6.715	Y	High cloud, inversion detection
28	7.325	Y	Cloud, inversion detection
29	8.550	Y	Cloud, dust, snow detection
30	9.730	N	
31	11.030	Y	Cloud, dust, snow detection, Land, sun-glint clear-sky restoral tests Inversion detection Thin cirrus detection
32	12.020	Y	Cloud, dust detection
33	13.335	Y	Inversion detection
34	13.635	N	
35	13.935	Y	High cloud detection
36	14.235	N	

Figure 3.11: **Overview over the spectral bands in MODIS (Ackerman et al. (1998) p.10, Table 2).** The first column shows the spectral band number and for the first 7 bands also their spatial resolution. The second column shows the corresponding wavelength of the band. The third column (N or Y) indicates wether or not this band is used in the cloud detection algorithm of MODIS and the last column displays additional information on how the corresponding band is used.

2017; Dybbroe et al. 2005b).

The MODIS algorithm, due to more spectal bands on the sensor itself, is able to use more tests than the AVHRR equivalent, potentially leading to a higher accuracy for cloud detection. For thin upper level clouds (i.e. Cirrus type) a reflectance test in the near-infrared (MODIS $r_{1.38\,\mu m}$, AVHRR $r_{1.6\,\mu m}$) can be combined with various Cirrus sensitive differences in the infrared bightness temperatures (e.g. MODIS $BT_{12\,\mu m}$ - $BT_{4\,\mu m}$, AVHRR $BT_{11\,\mu m}$ - $BT_{3.7\,\mu m}$ (Ackerman et al. 1998; Karlsson et al. 2013; Karlsson et al. 2017; Dybbroe et al. 2005b).

Furthermore, to test for cloud occurence, the algorithms also need information about other atmospheric variables such as water vapour content, surface temperature and the temperature of the troposphere at various pressure levels (Dybbroe et al. 2005b; Dybbroe et al. 2005a). These atmospheric variables, which can come from numerical weather prediction models or reanalysis datasets, are used for radiative transfer modelling and detection of atmospheric features that might influence cloud detection (e.g. temperature inversions) (Karlsson et al. 2013; Dybbroe et al. 2005b; Dybbroe et al. 2005a; Ackerman et al. 1998). The applied thresholds incorporate further if-conditions to account for environmental factors (e.g. illumination angle, surface albedo, sun glint) and can be dynamically updated (Dybbroe et al. 2005b; Dybbroe et al. 2005a). This dynamical threshold approach leads to the situation that every pixel has its own cloud detection algorithm (Dybbroe et al. 2005b).

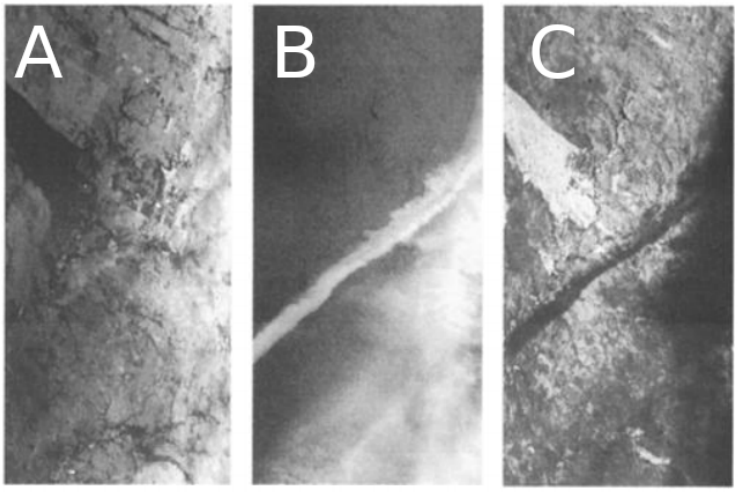

Figure 3.12: **MODIS airborne simulator contrail image in three spectral bands (Ackerman et al. (1998) p.32,142, Figure 1).** A) 0.66 μm reflectance, where white colours indicate higher reflectance. B) Same as A) but for the 1.88 μm near-infrared channel. C) 11 μm channel, where dark is cold and white is warm.

Over polar regions, cloud detection can be problematic. Normally, clouds are detected by remote sensing platforms by either higher reflectance in certain spectral bands and/or lower temperature then the underlying Earth surface (Ackerman et al. 1998). However, over the ice and snow covered areas of the GrIS, clouds can sometimes have a similar reflectance to

the underlying surface (Dybbroe et al. 2005b; Karlsson et al. 2013; Karlsson et al. 2017; Ackerman et al. 1998), rendering some reflectance tests impossible to use (e.g. MODIS reflectance test at 670 nm). Furthermore, except for parts of the melt season, Greenland experiences strong radiative cooling, leading to a stable stratification in the boundary layer with strong temperature inversions near the surface. Therefore the skin temperature of the surface is sometimes colder than the cloud temperature, creating problems for the cloud detection algorithms that depend on the brightness temperature thresholds in the infrared spectrum or on differences in (brightness) temperature between surface and clouds in different spectral bands (Ackerman et al. 1998; Dybbroe et al. 2005b; Karlsson et al. 2017).

To complicate matters further, some tests depend on the availability of solar radiation. For example, the 1380 nm band of the MODIS sensor is highly sensitive to high-level clouds, but the corresponding sensitivity vanishes during polar winter due to a lack of solar radiation (Ackerman et al. 1998) (see Fig.(3.10) and Fig.(3.12)). This spectral dependency is highlighted when looking at contrails in three different spectral bands of the MODIS airborne simulator (Fig.(3.12)). Panel A) in Fig.(3.12) shows the 0.66 μm band and the contrail is not visible at all, and in panel C) at the infrared wavelength of 11 μm (dark is cold) the contrail is visible, but the edges are not well defined (Ackerman et al. 1998). The best depiction of the contrail in Fig.(3.12) occurs in the 1.88 μm band (water vapour absorption, panel B)), but this band in the near-infrared cannot be used without sunlight (polar summer) (Ackerman et al. 1998).

Conversely, active sensors such as the CALIPSO-CALIOP do not depend on the availability of sunlight. However, the CALIOP sensor is limited in its spatial sampling coverage, only reporting observations at NADIR with a telescope viewing angle of 130 μrad, resulting in a footprint size of only 90-100 m (Winker et al. 2007). Together with a revisit time of 16 days, the spatial coverage of the CALIOP lidar is not enough for creating two-dimensional maps of seasonal cloud cover trends over the GrIS, especially when compared to the swath width of ≈ 2000 km from MODIS and AVHRR (Ackerman et al. 1998; Dybbroe et al. 2005b). Therefore, passive sensors might be an attractive alternative, as long as one keeps their shortcomings outside of polar summer in mind.

We chose to focus our use of AVHRR and MODIS on June-July-August only, because the passive sensors have the best cloud detection capabilities during summer (Fig.(3.10)). This temporal focus is further strengthened by the decreasing albedo of the GrIS during summer (Box et al. 2012), which helps to create a stronger difference between the reflectance of clouds and the GrIS surface, leading to more accurate cloud detection (Ackerman et al. 1998; Dybbroe et al. 2005b; Dybbroe et al. 2005a; Karlsson et al. 2017). Karlsson et al. (2017) found, by comparing AVHRR cloud fractions with the active CALIOP sensor, that during polar winter up to 50% of clouds remain undetected over the coldest parts of Greenland (Fig.(3.10)). However, during polar summer, the cloud detection capabilities are nearly as

good as over other parts of the world (Karlsson et al. 2017).

Chapter 4

A validation of clouds and radiation in two state-of-the-art regional climate models

4.1 Abstract

Greenland is currently the main single contributor to global sea level rise, with a maximal contribution of 1.2 mm in 2012 alone (Van den Broeke et al. 2017). It has recently been shown that changes in the circulation regime towards drier, warmer and sunnier summers have led to significant changes in cloud cover and in the surface energy budget of the Greenland Ice Sheet (GrIS), resulting in sustained and accelerating mass loss (Van den Broeke et al. 2017; Hofer et al. 2017; Delhasse et al. 2018; Hanna et al. 2016; Fettweis et al. 2017; Box et al. 2012; Van den Broeke et al. 2016). While changes in cloud cover and of the surface energy budget (SEB) are a main contributor to the recent increases in surface melt, these properties often remain poorly constrained. Here we use two regional climate models (MARv3.9, RACMO2p3 (Fettweis et al. 2017; Noël et al. 2018)) and compare the models' ability to reproduce absolute values and trends in the SEB and cloud cover over the last decades. Both models were forced with the same boundary conditions from the ERA-Interim reanalysis (Dee et al. 2011), to be able to attribute differences in the model simulations only to the physics in the RCMs themselves.

We compare the simulated radiative fluxes to 23 AWS in-situ weather stations from the PROMICE network (Ahlstrøm et al. 2009; As et al. 2011), the cloud cover trends to remotely sensed data from AVHRR (CLARA-A2 (Karlsson et al. 2017)) and the atmospheric water vapour content to in-situ observations from Summit Camp in the interior of the GrIS (Dybbroe et al. 2005b; Miller et al. 2015; Miller et al. 2017). Our results show, that MAR

and RACMO are able to capture melt season changes in cloud cover when compared to satellite observations, and that they are also able to reproduce in-situ observations of temporal changes in shortwave (solar) and longwave (terrestrial) radiation accurately. However, when compared to the daily absolute values of the radiative components of the surface energy budget, the two regional climate models show greater biases than when comparing their temporal changes. Therefore, the more accurate representation of temporal changes in the energy budget, rather than their absolute daily values in regional climate models, raises the question whether it is more important that models are able to accurately depict temporal changes, rather than the absolute magnitude of the surface energy budget components over the Greenland Ice Sheet.

4.2 Introduction

The Greenland Ice Sheet is losing mass at an increasing pace since approximately the mid-1990s (Van den Broeke et al. 2017; Fettweis et al. 2017; Van den Broeke et al. 2016). While the annual mass loss has increased, the split between anomalies in ice discharge into the ocean ("calving rates") and surface melt has changed significantly: Until the 1990s, surface mass balance (SMB) and ice discharge into the ocean had a similar magnitude, corresponding to an ice sheet in equilibrium (Van den Broeke et al. 2016). However, from 1991 to 2015 this balance shifted, and a reduction in SMB, driven by surface melt and runoff, accounts for almost 60% of the total mass loss (1991-2015), peaking at 68% during 2009-2012 (Enderlin et al. 2014). Because surface melt is driven by absorbed radiative fluxes (Van de Wal et al. 2005), it is highly important for regional climate models to accurately reproduce observations and trends of the radiative components of the SEB.

Additionally, due to their significant impact upon radiative fluxes over the Greenland Ice Sheet, clouds are an essential parameter to obtain accurate melt simulations over Greenland (Hofer et al. 2017; Hofer et al. 2019; Van Tricht et al. 2016; Wang et al. 2019; Wang et al. 2018). Here, I validate two regional climate models (RACMO2p3, MARv3.9) against cloud satellite remote sensing data (AVHRR, MODIS) and in-situ data from the PROMICE network (As et al. 2011) and Summit station (Miller et al. 2015; Miller et al. 2017) to evaluate the biases and trends in the Greenland Ice Sheet surface energy budget and cloud cover trends in regional climate model simulations.

4.3 Regional climate models, observations and computation of melt potential

4.3.1 Modèle Atmosphérique Régional (MAR)

The Modèle Atmosphérique Régional (MAR) has been specifically developed for polar climates (Gallée et al. 1994; Gallée 1995). Its dynamical core solves the primitive equation set and uses the hydrostatic approximation to simplify the momentum equations (Gallée et al. 1994; Gallée et al. 1994; Fettweis 2007). An explicit description of most of the model physics are presented in Gallée et al. (1994), Gallée (1995) and Fettweis (2007), including the hydrological cycle and cloud microphysics schemes which are essentially based on studies by Kessler (1995) and Lin et al. (1983). In this validation study, I use output from the MAR version 3.9. At the lateral boundaries, the MAR model is forced by reanalysis data from ERA-Interim dataset (Dee et al. 2011). The forcings fields are prescribed at an interval of 6 hours. As boundary and initial conditions, MAR uses 3-D atmospheric fields of temperature, specific humidity, pressure and the u- and v- components of the wind vector. Additionally, MAR also uses the fractional sea ice cover over the ocean surface and sea surface temperature as boundary conditions. Note, that the clouds (i.e. the vertical distribution of ice and water particles) are not prescribed at the lateral boundaries and as a result, the clouds are not being advected onto the MAR domain from the forcing fields. The snowpack properties in MAR are modelled by the prognostic snow scheme CROCUS (Gallée et al. 2001; Vionnet et al. 2012; Brun et al. 1992).

MAR was run on a 15x15 km equal-area grid and used an integration time step of 90 seconds. Over the GrIS, the MAR model has been thoroughly validated and tuned to match in-situ and remote sensing observations (Fettweis 2007; Fettweis et al. 2017; Fettweis et al. 2011). It has especially been tuned to match the surface mass balance and melt extent on the GrIS (Fettweis 2007; Fettweis et al. 2011; Hofer et al. 2019), and has been validated against in-situ observations, satellite melt extent, in-situ surface mass balance observations and ice core based annual accumulation rates (Fettweis et al. 2017).

4.3.2 RACMO

While the overall architecture of RACMO is comparable to MAR, the parameterisations and the dynamical cores of the models differ. In this thesis I use the most current outputs of RACMO (RACMO2.3p2). The polar version of RACMO essentially uses the dynamical core of the High Resolution Limited Area Model (HIRLAM) and also incorporates a predictive snow model (Noël et al. 2018; Meijgaard et al. 2008; Undén et al. 2002).

The snow model in RACMO is able to predict the evolution of the snowpack properties such as melt, meltwater percolation and refreezing and snow grain metamorphism (Noël et al. 2018). The snowpack properties are forecasted on up to 40 layers within the snowpack at varying depths (Noël et al. 2018). The cloud microphysical scheme and therefore the hydrological cycle, from water vapour to cloud droplets/crystals and precipitation, is based on the physics package cycle CY33r1 of the European Centre for Medium-Range Weather Forecasts (ECMWF) Integrated Forecast System (ECMWF 2009; Noël et al. 2018). The model output used in this study is located on a grid-spacing of approximately 5.5 x 5.5 km and is therefore a slightly newer version than the RACMO results presented in Noël et al. (2018).

Like the MAR model, RACMO was also forced by the ERA-Interim reanalysis dataset at the lateral boundaries (Dee et al. 2011; Noël et al. 2018), and the boundary conditions are prescribed at all 40 vertical layers of RACMO at a 6-hourly timestep (Noël et al. 2018). The regional climate model RACMO has been validated thoroughly over the Greenland Ice Sheet. It has been compared to in-situ observations of surface mass balance from Machguth et al. (2016), against in-situ observations from the PROMICE and IMAU weather stations (Noël et al. 2016; Noël et al. 2018), but also to satellite albedo data from MODIS (Noël et al. 2016) and to the GRACE gravimetry data (Van den Broeke et al. 2016).

Initial results from the SMB Model Intercomparison Project (SMBMIP) show, that MAR and RACMO model the Greenland Ice Sheet surface mass balance components very similarly (Fettweis 2018). When compared to the PROMICE SMB database of in-situ observations, MAR has a mean bias of 0.10 mWE, while RACMO has a bias of -0.07 mWE. Furthermore, the Root Mean Square Error (RMSE) in MAR is 0.49, while it is slightly greater in RACMO with 0.61. When looking at the correlation score between observed and modelled SMB, MAR has a slightly higher R^2 score of 0.93 compared to 0.89 in RACMO. Out of the nine GrIS SMB models in the SMBMIP project, MAR has the highest and RACMO the third highest correlation score when compared to SMB observations, with a similar performance in the mean bias and RMSE. Therefore, MAR and RACMO are reproducing the surface mass balance observations with similar accuracy (Noël et al. 2018; Fettweis et al. 2017).

4.3.3 In-situ observations

For the validation of the two models in our study, we use in-situ observations from 23 automatic weather stations (AWS) from the Programme for Monitoring of the Greenland Ice Sheet (PROMICE) network (Ahlstrøm et al. 2009; As et al. 2011). The temporal coverage of the PROMICE AWS dataset starts in 2007 (5 stations) and has been expanded to 23 stations (Ahlstrøm et al. 2009; As et al. 2011).

Here I use the reported daily mean values, which I have post-processed in the following way

to avoid using erroneous sensor readings, similarly to Noël et al. (2018). First, I discarded unphysically low values where daily mean radiation values were below 0 Wm^{-2}. Then, I rejected values that were unphysically large such that I rejected values where the outgoing longwave radiation (LWU) was $\geq$ 318 Wm^{-2}, indicating a surface temperature of above 0°C at and emissivity ϵ of $\approx$ 0.99. Similarly, I also discarded daily mean values of longwave incoming fluxes above 450 Wm^{-2}. Further, I computed the values for the standard deviation of the mean bias of all stations for both models and averaged it over all the stations and both models. Then I discarded values in the time series where the difference between the modelled daily radiative fluxes and the observations were outside of $6 \cdot \sigma$, where σ is the mean standard deviation of the mean bias over all PROMICE stations. In our case, the values for $6 \cdot \sigma$ are: $SWD = 86\ Wm^{-2}, LWD = 38\ Wm^{-2}, SWU = 130\ Wm^{-2}, LWU = 53\ Wm^{-2}$. Figure (4.1) shows the number of daily observations that were deemed plausible by our described testing algorithm.

4.3.4 Computation of anomalies

For large parts the following section ("Computation of anomalies") follows the description in Hofer et al. (2017) and Hofer et al. (2019).

Anomalies presented in this chapter are calculated based on the 1971-1990 average of the model outputs (Melt, SMB, cloud properties, radiative properties etc.). Whenever radiation anomalies and non-radiative surface energy budget components are not shown in their SI-unit (joule) they have been converted to a mass anomaly ("melt potential") (Hofer et al. 2017). For this purpose, I use the heat of fusion which is needed to melt 1 kg of ice H_f = 333.55 kJ/kg, where positive values correspond to an above average downward flux of energy or heat. A positive anomaly therefore means that more energy has been received at the surface of the GrIS than in the reference climate period. Because the two model grids differ in their spatial resolution and grid centers, I have regridded the MAR outputs onto the 5.5 km x 5.5 km grid of RACMO using a bilinear interpolation approach using the Python xESMF package (https://xesmf.readthedocs.io/). The three main steps from the normal model output to the anomalies used in this study are:

- Computing the monthly arithmetic mean of a given parameter from daily model outputs
- Computing the 1971-1990 climatological mean state of every pixel for every month
- Summing up the anomalies from the climatological mean and convert to melt potential (if applicable)

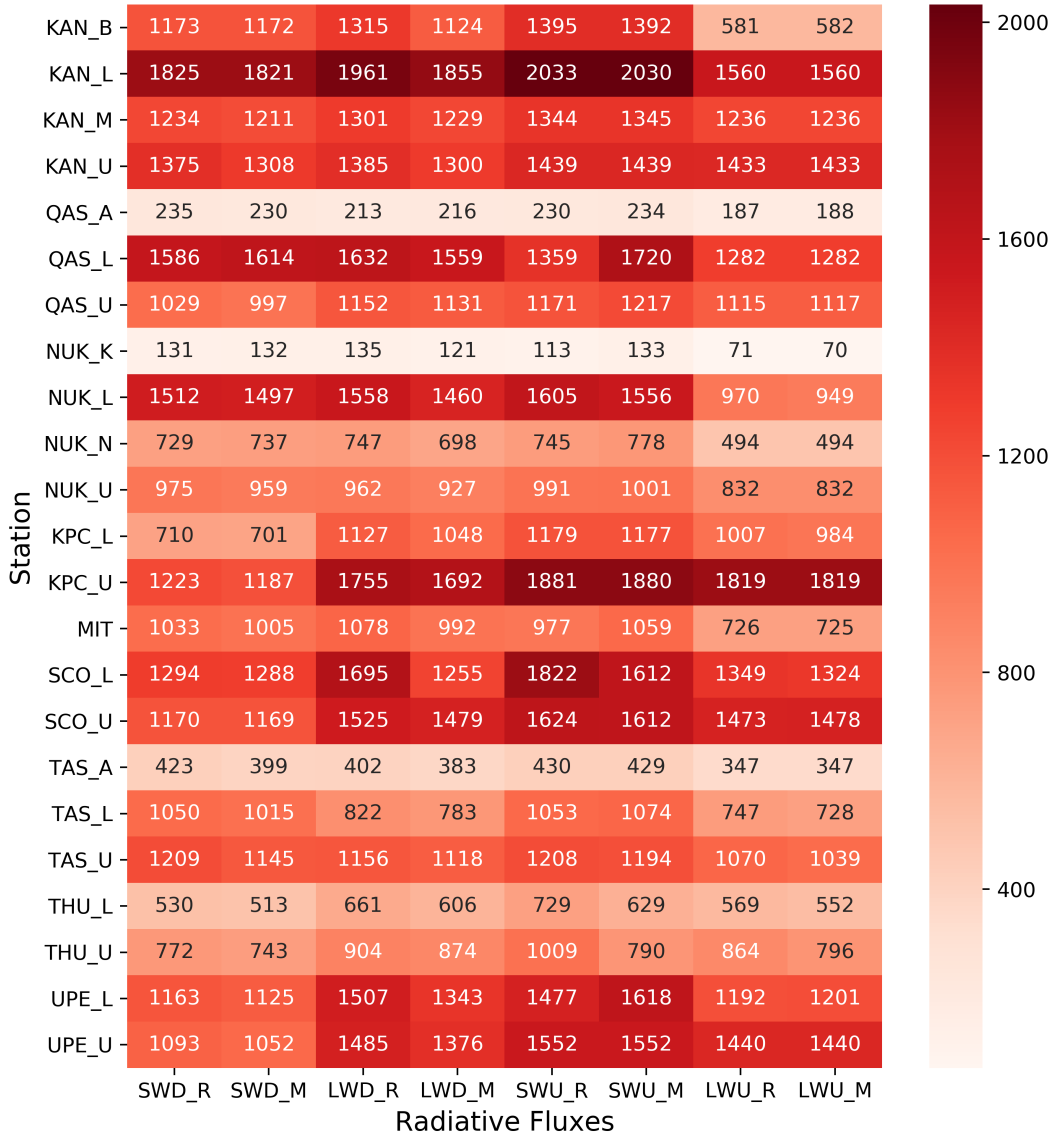

Figure 4.1: **Number of daily observations of all 23 PROMICE weather stations used for statistical analysis.** Number of daily observations after checking for physical plausibility and neglecting values that lie outside of 6 times the standard deviation of the mean bias following the method of Noël et al. (2018) (see Methods for further description of post-processing applied to in-situ observations).

The following equation was used to compute the anomalies for every pixel and month

$$a_{i,j,month} = x_{i,j,month} - \overline{x_{i,j,m}} \tag{4.1}$$

where $a_{i,j,month}$ refers to the anomaly of a model pixel value ($x_{i,j,month}$) in the i^{th} row and j^{th} column of the grid, from the corresponding monthly grid cell climatology. Subscript m refers to the month for which the equation was evaluated, i and j to the specific position on the model grid.

Calculations began with the radiative anomalies at each pixel in watts per metre squared. Because of the grid-cell extent of 5.5x5.5 km, we then multiplied this by the area of the pixel to arrive at the total anomaly in watts (joules per second) of one grid cell. We then summed up all the individual grid cell values spatially over the entire GrIS (see Eq. 4.2) and multiplied it by the duration of the month (in seconds). This took us from joules per seconds to the total anomalies in joules, which we then converted to melt anomalies in gigatons.

$$\Delta a_{total} = \sum_{i} \sum_{j} a_{i,j,month} \tag{4.2}$$

4.4 Results

4.4.1 Partitioning of the surface energy and mass budget anomalies

Overall, MARv3.9 and RACMO2p3 model the anomalies (i.e. the temporal changes) of the GrIS surface mass balance (SMB) during the melt season very similarly (Fig.(4.2) A,B). When compared to the 1971-1990 mean state of each model, MAR simulates a 3.6% greater decline in SMB than RACMO (-3410 Gt vs -3290 Gt). In both cases, the main driver this decline in SMB is a significant increase in summer surface melt with 3880 Gt in MAR and 3470 Gt in RACMO. Most of this surplus surface meltwater is routed off the GrIS via surface runoff, with an increase of 2950 Gt (8.1 mm sea level equivalent SLE (Planton 2013)) in MAR and 2680 Gt (7.4 mm SLE) in RACMO (Fig.(4.2) A,B green lines). Furthermore, both models show similar efficiency in creating runoff from extra meltwater, with MAR transporting 76% of all extra meltwater from the GrIS via surface runoff, compared to 77% in RACMO. Both models also show a slight decline in summer precipitation, -490 Gt (MAR) and -580 Gt (RACMO), most likely due to a shift of the North Atlantic Oscillation (NAO) leading to persistent anticyclonic conditions during summer (Hanna et al. 2016; Hanna et al. 2018; Hofer et al. 2017). I find no evidence for a significant contribution from changes in sublimation rates (-35 Gt and -29 Gt). Overall, the two models agree that the main driver of recent SMB changes are due to an increase in surface melt and subsequent meltwater runoff.

When partitioning the surface energy budget (SEB) anomalies during the melt season into

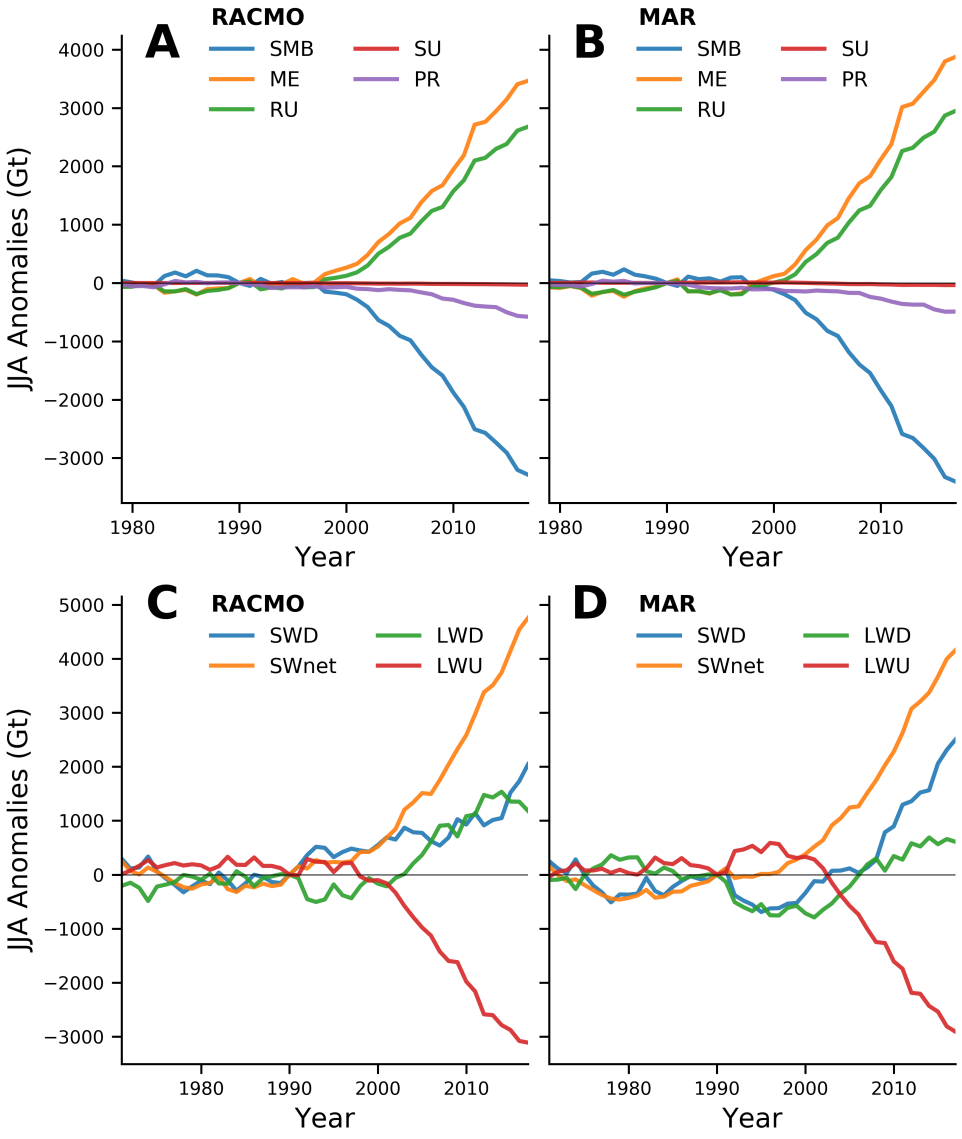

Figure 4.2: **Cumulative summer surface mass balance and radiation anomalies expressed as melt potential.** A) Cumulative anomalies of all surface mass balance components during summer (JJA) from RACMO, compared to the 1971-1990 average. B) same as A) but for MAR. C) Cumulative anomalies of the surface energy budget components compared to 1971-1990 in RACMO. All SEB components are expressed as "melt potential" in gigatonnes (Gt, see methods). D) same as C) but for MAR.

its components, the two models slightly disagree on the magnitude of each component, but still agree on the major temporal changes in the SEB (Fig.4.2 C, D). When looking at the "external" drivers of the SEB (i.e. not influenced by surface properties), both models show a higher contribution from downwelling shortwave fluxes (SWD, less clouds) than from an increase in downward longwave fluxes (LWD, higher temperature/humidity). MAR produces 2500 Gt of SWD melt potential compared to 2050 Gt in RACMO. Furthermore, MAR shows an increase in cumulative LWD anomalies of 600 Gt, while the LWD increase in RACMO is two times greater than in MAR at 1200 Gt.

Overall, even during decades of sustained Arctic warming, both models agree that during the melt season the main external increase in downwelling radiation is coming from incoming shortwave radiation. Therefore, reduced cloud cover due to an increased frequency of high-pressure systems over the Greenland Ice Sheet has contributed more energy to the surface energy budget than the increase in atmospheric temperature, before taking into account the radiation-surface interaction. Spatially, downwelling shortwave radiation anomalies can especially enhance melt rates over the dark albedo ablation zone, while their impact is limited in the accumulation zone.

Additionally, these increases in external SEB components have led to an increase in the melt-albedo feedback (Box et al. 2012), expressed in the net shortwave anomalies (SWnet) of 4800 Gt (RACMO) and 4200 Gt (MAR). However, the melt-albedo feedback in both models seems to have a different sensitivity to the overall melt. While RACMO is modelling slightly lower melt anomalies than MAR since the mid-1990s (3470 Gt in RACMO, 3880 Gt in MAR), RACMO still produces a higher increase in absorbed shortwave anomalies (SWnet). Potentially, the greater increase in SWnet indicates a more sensitive melt-albedo feedback in RACMO (i.e. a greater albedo decline), especially given that RACMO also models a smaller increase in SWD.

Further, because SWnet is a linear combination of SWD and albedo (α), the decrease in summer clouds and SWD has contributed roughly 60% in MAR and 42% in RACMO to this increase in SWnet. Both models also show a significant increase in "heat-loss" from the surface via emitted longwave anomalies (LWU, -2900 Gt (MAR) and -3100 Gt (RACMO)). This is a result of increases in GrIS snow, firn and ice temperature, driven by greater absorbed shortwave and longwave fluxes, with SWD and SWnet being the dominant contribution in both models. Overall, both models agree that the main driver of recent changes in the external SEB components and subsequent melt is due to an increase in downwelling shortwave radiation (SWD, i.e. less clouds) rather than the atmospheric greenhouse effect and an increase in warm-air and humidity advection (LWD).

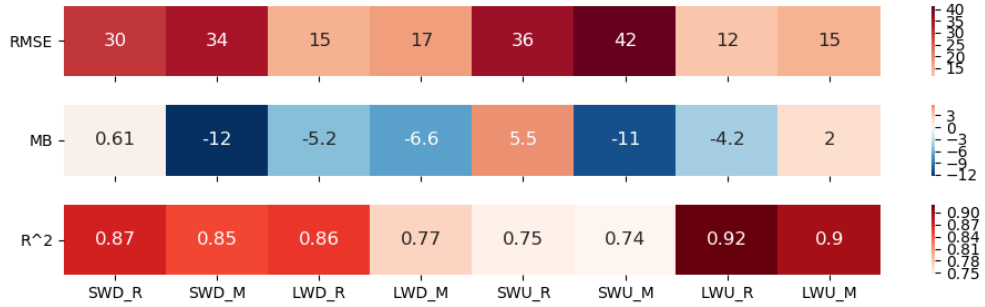

Figure 4.3: **Mean statistical values of MAR and RACMO over all 23 PROMICE weather stations.** The first row shows the mean root mean square error (RMSE, W/m^2) for both models, where $_R$ stands for RACMO and $_M$ stands for MAR statistics. The second row shows the mean bias (W/m^2 over all fluxes and PROMICE stations for both models, and the last row shows the mean correlation score R^2 for both models.

4.4.2 Radiation biases in MAR and RACMO

While the cumulative anomalies, and therefore the temporal trends, of both models show a very similar behaviour, they produce different biases when compared to the absolute daily values of in-situ observations of radiative fluxes on the GrIS. In general, both models show a similar performance when comparing the correlation score (R^2) of the monthly SEB components to in-situ observations from the PROMICE AWS data (Fig.(4.3), Fig.(4.4)). For the external SEB components, SWD and LWD, the average R^2 values are 0.85 (MAR) and 0.87 (RACMO) for SWD (Fig.(4.3)), and 0.77 (MAR) and 0.86 (RACMO) for LWD.

However, when looking at the mean biases in Fig.(4.3), RACMO reproduces the daily observations with a lower bias than MAR for both incoming SEB components. While the mean bias in the LWD fluxes is similarly small at -5.2 Wm^{-2} in RACMO and -6.6 Wm^{-2} in MAR, they differ significantly when looking at SWD fluxes (biases for all station individually can be found in Fig.(4.5). Here, RACMO has a bias of only 0.61 Wm^{-2} over all PROMICE stations, while MAR has a higher mean bias of -12 Wm^{-2}. The root mean square error (RMSE) shows a similar behaviour for both models (Fig.(4.3), Fig.(4.6)), with a 4 Wm^{-2} higher RMSE in SWD, and a 2 Wm^{-2} higher RMSE in LWD in MAR than in RACMO.

When looking at the outgoing components, SWU and LWU, there is a contrasting picture. MAR and RACMO both seem to show a significantly lower but similar average correlation in the SWU component with correlation scores of 0.75 (RACMO) and 0.74 (MAR) (Fig.(4.3), Fig.(4.4)). This is very likely because the surface albedo exerts very strong spatial heterogenity, reducing the representativenes of the in-situ point observations when compared to a model pixel value (5.5 x 5.5 km in RACMO, 15 x 15 km in MAR) (Box et al. 2012; Tedstone et al. 2017; Alexander et al. 2014; Ryan et al. 2017). The mean biases (and Fig.(4.4), Fig.(4.5)) in the reflected shortwave fluxes are 5.5 Wm^{-2} for RACMO and -11 Wm^{-2} for

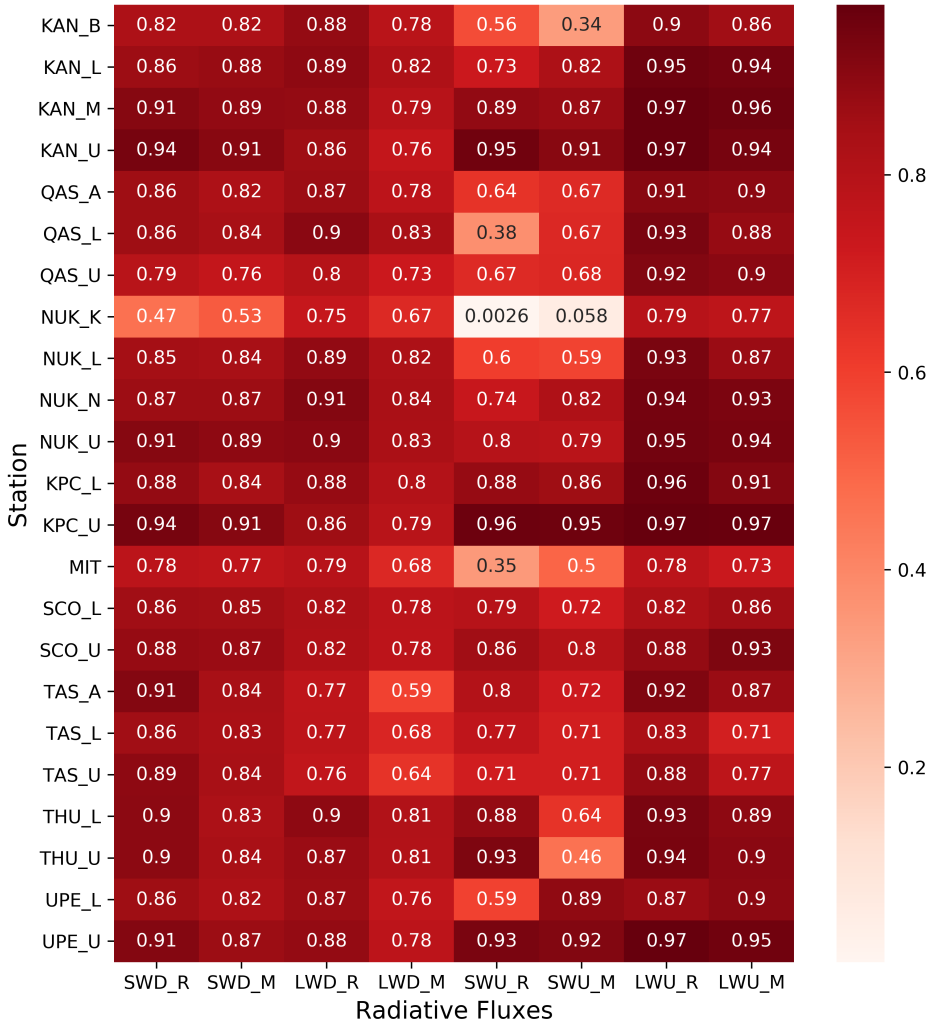

Figure 4.4: **Correlation scores between Greenland in-situ observations and two regional climate models.** Correlation between in-situ radiative flux observations (PROMICE weather stations (As et al. 2011)) and MAR and RACMO model output. The correlation scores are R^2 values, computed using daily means. The station names are listed on the left ("y-axis"), while the name of the radiative fluxes is on the "x-axis". The underscore "M" stands for MAR, while "R" stands for output from the RACMO model.

MAR. Conversely, LWU has the highest correlation of all SEB fluxes, with 0.90 (MAR) and 0.92 (RACMO). It also shows the lowest mean biases for both models, with MAR producing a slightly lower bias at 2 Wm^{-2}, compared to RACMO's -4.2 Wm^{-2}.

Both models display the lowest bias in the LWU component, which is mainly a function of the surface temperature and therefore of the absorbed fraction of the other radiative fluxes. This could indicate that both models have compensating biases elsewhere in the model physics. Given that the radiative forcing due to the increase in greenhouse gas concentration so far has been roughly 1.5 W/m^2 (Church et al. 2013), biases in both models of the order of 10 W/m^2 seem significant. However, both models very likely have compensating biases to create (1) an SMB that matches in-situ observations, (2) very similar temporal trends in the SEB and SMB (Fig.(4.2)).

Both models, despite significant differences in the absolute magnitude of daily radiative fluxes, show a very similar SMB and SEB response (Fig.(4.2)). This raises the question whether capturing anomalies and temporal trends in the SEB and SMB are more important than reproducing the absolute magnitude of the SEB components? Alternatively, this could also imply that due to the high spatial variability of the surface albedo, point observations are less representative of a model pixel value in the SWU component than in the LWU component (Ryan et al. 2017).

In some cases, very low correlation scores in Fig.(4.4) together with a very low number of daily observations (Fig.(4.1)) could have three different reasons. First, the location of the AWS is not representative of the pixel value of the model due to local micro-geographical features. Second, there could be problems with the radiometers of the specific AWS station (frequent riming or overheating). Third, a short observational period of the AWS station. In case of the AWS "MIT" the most likely "issue" is the local geography. "MIT" is situated on an independent glacier on an island only $\approx$ 5 km away from the sea, surrounded by a very complex fjord-glacier-mountain system. In this case more than 1000 daily values that have passed our tests (Fig.4.1) indicate that the problem here is the model resolution, rather than erroneous measurements.

In the case of another station with unfavourable statistic, "NUK_K", also located on an independent glacier in a complex fjord system, the problem could be exacerbated by a short observational period (starting in summer 2014) resulting in just over 100 acceptable daily values. In both cases however, given the frequently observed fog over these fjords, the local meteorological conditions could also favor frequent riming and subsequent measurement problems. In case of the station "KAN_B", the low correlation scores for outgoing shortwave radiation are likely a direct consequence of the fact that this AWS is situated on land, just off the GrIS and misrepresentation of the surface albedo of the overlying model grid-cell due to slight inaccuracies in the ice sheet extent in both models. Overall however, despite testing for physical and statistical plausibility, it is important to highlight these potential sources of

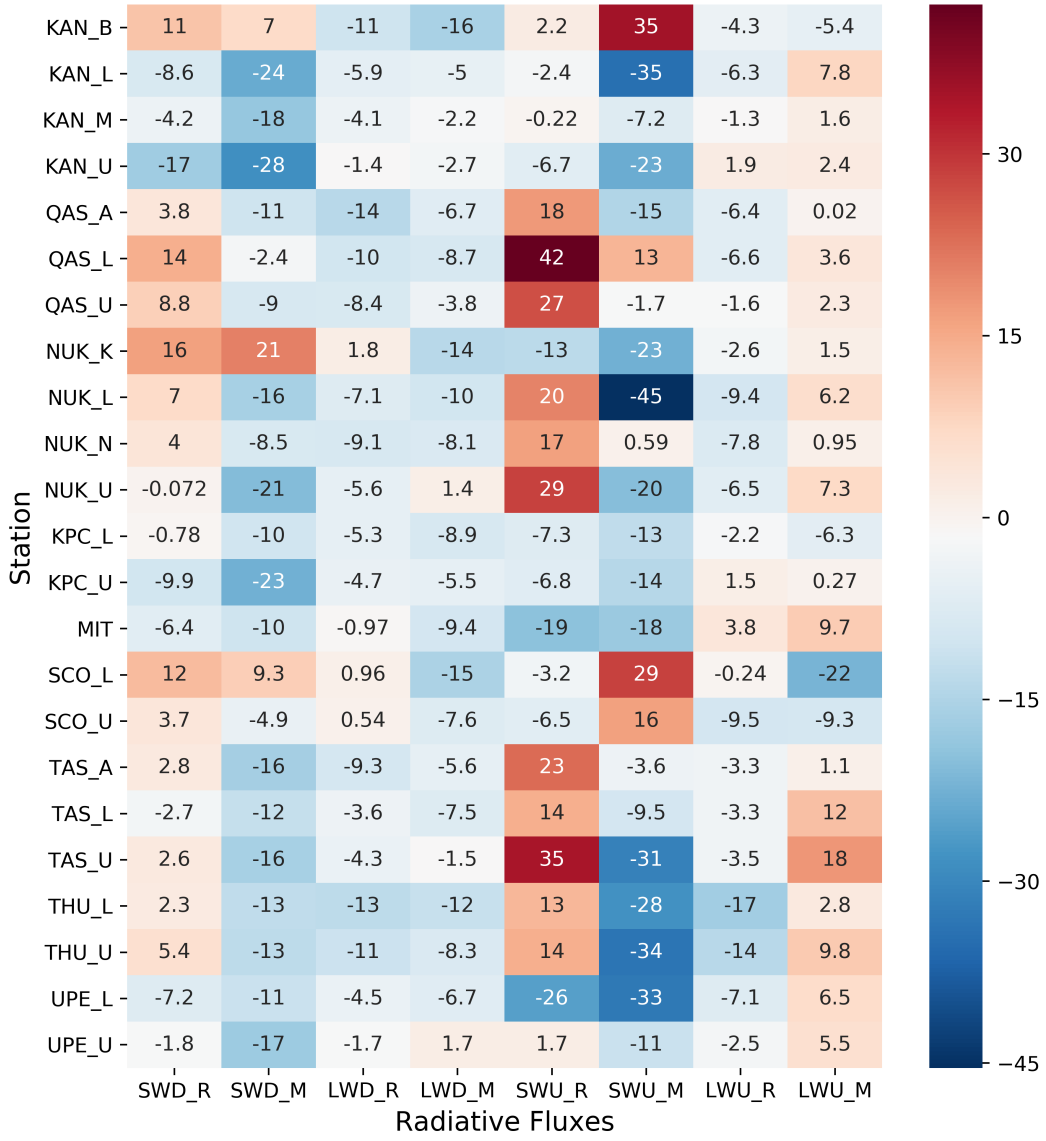

Figure 4.5: **Mean bias (W/m^2) of daily observations of all 23 PROMICE weather stations.** Mean bias of each AWS station in the PROMICE dataset when compared to RACMO and MAR radiative fluxes (daily timestep).

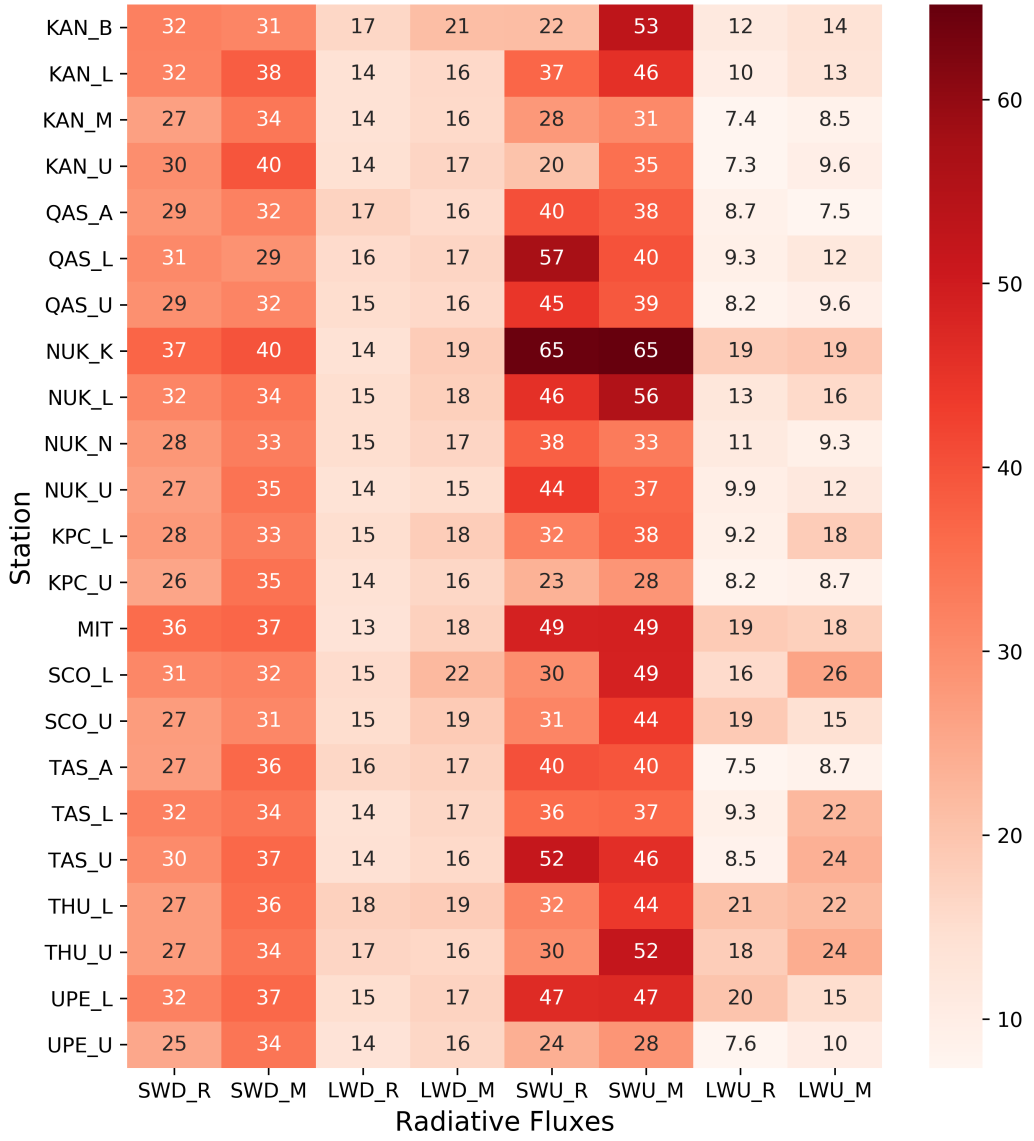

Figure 4.6: **Mean root mean square error (W/m^2) of daily observations of all 23 PROMICE weather stations.** Mean root mean square error of each AWS station in the PROMICE dataset when compared to RACMO and MAR radiative fluxes.

reduced statistical scores.

4.4.3 Spatial trends in the surface energy budget

While we have discussed temporal trends in SMB and SEB, we have not yet shown how MAR and RACMO compare when looking at spatial trends in the SEB components over the last two decades. During 1995-2015, both models show a signficant increase in downwelling solar radiation (SWD), due to a decrease in summer cloud cover (Hofer et al. 2017). Both MAR and RACMO model the greatest increase in SWD over the south of the GrIS, with a more patchy picture and lower trends in the North (Fig.4.7 A, B). The largest difference between RACMO and MAR (Fig.4.7 C) is visible in the NW accumulation zone and over the SW ablation zone of the GrIS. Overall, MAR simulates an increase in SWD over 88% of the GrIS, while RACMO only shows an increase over 65%, likely indicating slight differences in modelled cloud cover trends. In general, MAR shows a slightly larger trend over the accumulation zone (blue colors Fig.(4.7) C), while RACMO models a more positive trend over parts of the darker ablation zone.

The trends in LWD show the opposite spatial patterns as SWD: LWD has decreased in the southern half of the GrIS and increased in the North (Fig.4.7 D, E). In both models the greatest increase in LWD happens toward the Northwest, with slightly larger trends again in MAR (4.7 F). However, the spatial differences are more homogenous than in the SWD (4.7 C vs. F). LWD decreased over 36% of the GrIS in MAR and 47% in RACMO, during a period of sustained and accelerating Arctic warming, highlighting the importance of synoptic-scale circulation and cloud cover changes in the GrIS surface energy budget. Overall, the spatial patterns in SWD and LWD seem to be mostly driven by the same cause, most likely the decrease in cloud cover over the last two decades in the South, while LWD increases have been amplified by an overlapping increase in temperature and cloud cover in the North.

However, it is interesting to note that compared to the absolute biases, which are on the order of 5-10 W/m^2 (Fig.(4.3)), the differences in temporal trends in SWD and LWD between MAR and RACMO differ less. On average, for the temporal trends in incoming shortwave radiation averaged over the whole Greenland Ice Sheet (Fig.(4.7)) RACMO and MAR only differ by 0.69 W/m^2. Furthermore, for the longwave temporal trends over the last two decades, MAR and RACMO show an even lower difference of only 0.31 W/m^2.

When considering the temporal trends in downwelling shortwave radiation, both models have a similar sensitivity to the same lateral boundary conditions. Additionally, given the similar trends in SMB and melt as well as in the radiative components of the surface energy budget, this smaller difference in trends highlights that it might be more important for polar RCMs to capture temporal changes in the surface energy budget accurately, rather than the

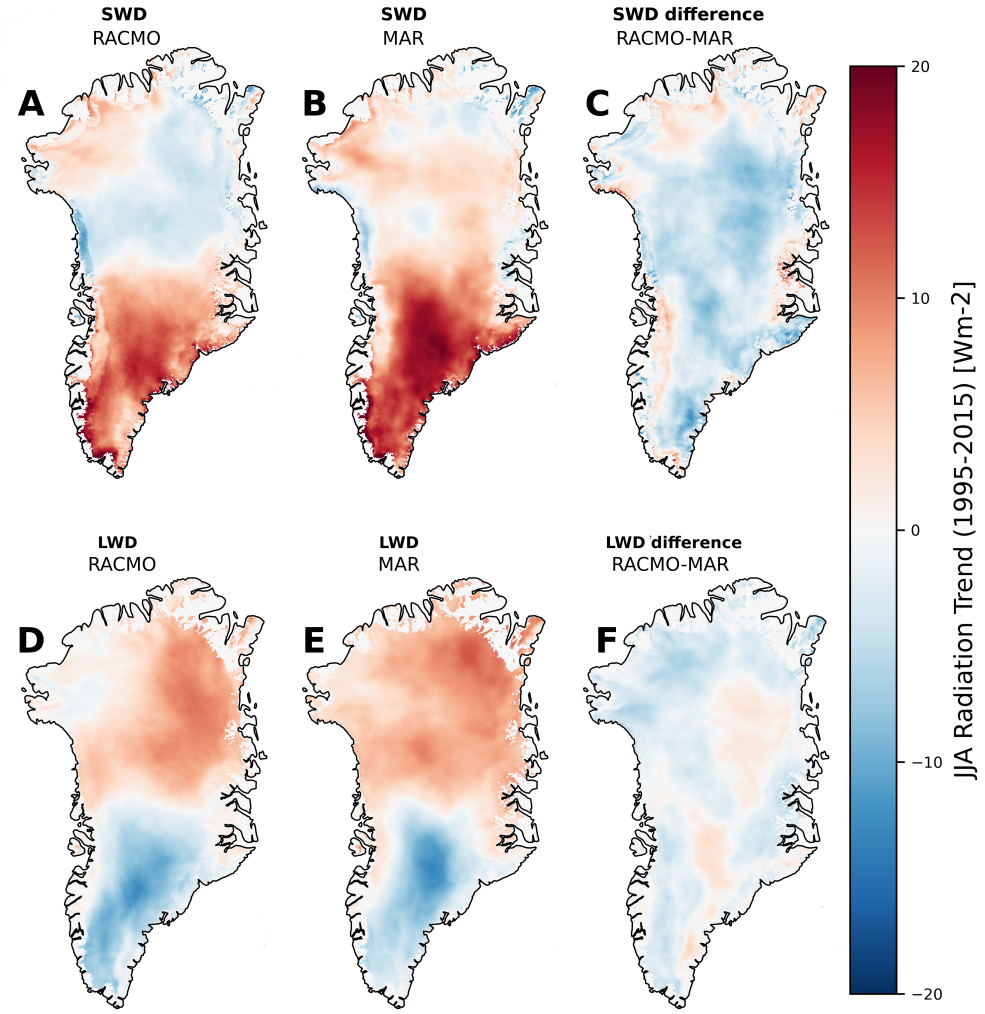

Figure 4.7: **Trends in downwelling shortwave and longwave fluxes.** A) Temporal trend in JJA shortwave downward radiation (JJA) from RACMO during 1995-2015 (total change). B) Same as A) but for MAR. C) Difference in trends of downwelling shortwave radiation (1995-2015) between MAR and RACMO during JJA (RACMO-MAR), positive values (red) indicate a lower value in MAR -> more negative or less positive trend in MAR than in RACMO. D) Same as A) but for temporal trends in incoming longwave radiation. E) Same as D) but for MAR. F) Difference in trends of downwelling longwave radiation (1995-2015) between MAR and RACMO during JJA (RACMO-MAR), positive values (red) indicate a lower value in MAR -> more negative or less positive trend in MAR than in RACMO.

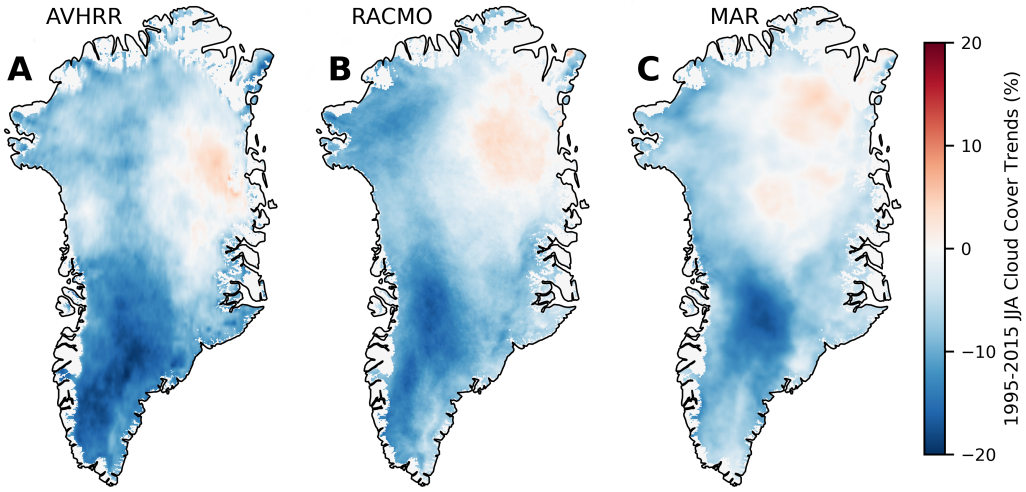

Figure 4.8: **Comparison between satellite and model cloud cover trends during summer.** Linear trend (total change) in JJA cloud cover during 1995-2015 from A) the Clara-A2 dataset using the AVHRR sensor (Karlsson et al. 2017), B) from RACMO and C) from MAR.

absolute magnitude of the daily radiative fluxes.

4.4.4 Cloud cover trends: RCMs vs. satellite observations

Observed and modelled cloud cover trends explain the patterns in LWD and SWD changes: Satellite and RCM data both depict a strong decrease in melt season (JJA) cloud cover over the GrIS, with the largest reduction in the southern half of Greenland and a more patchy picture in the North (1995-2015, Fig.(4.8) A-C). Again, when comparing RACMO (Fig.(4.8) B) and MAR (Fig.(4.8) C) to the observed spatial cloud cover trends during 1995-2015, they both agree on the significant decrease of JJA cloud cover in the south. However, while the satellite observations show an increase in summer cloud cover over only 5.9% of the GrIS, MAR models an increase over 10.4% and RACMO over 9.4% of the GrIS. Therefore, both models underestimate the spatial extent of cloud cover reductions during summer, but also underestimate the magnitude of the cloud cover reductions in the south of the Greenland Ice Sheet. Potentially, the differences in cloud cover trends between observations and models also lead to subsequent biases in the surface energy budget over areas where the trends disagree with the observations. However, both models show good agreement with the spatial patterns of observed melt-season cloud cover trends over the GrIS when compared to the CLARA-A2 dataset (Karlsson et al. 2017).

The underestimation of melt season cloud cover reductions in the RCMs is also apparent in the magnitude of the cloud cover trends (Fig.(4.9)). Figure (4.9) A) shows that the magnitude of the latitudinal mean of JJA cloud cover trends is greater in the satellite observations

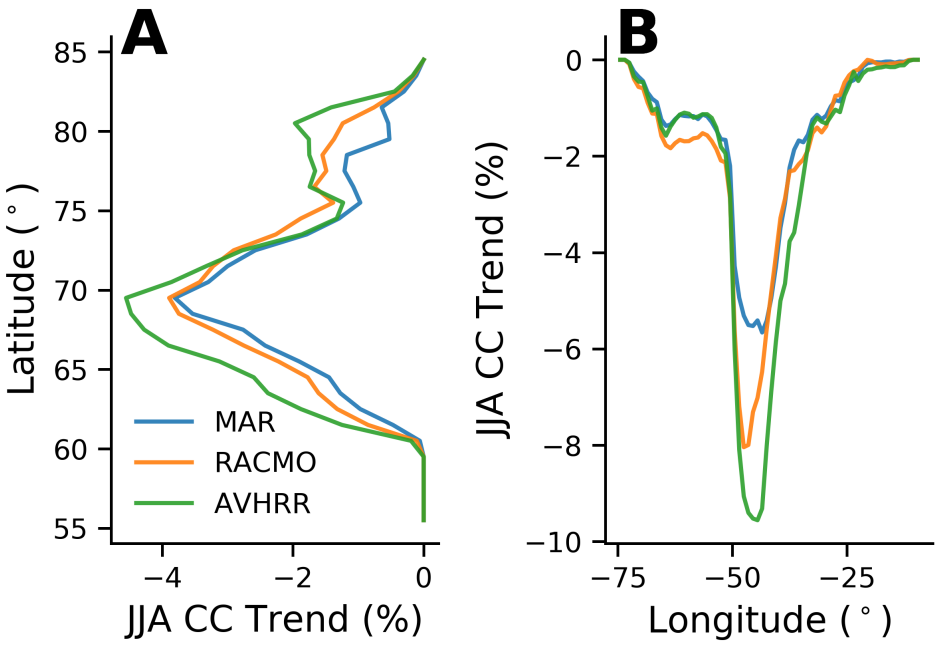

Figure 4.9: **Latitudinal and longitudinal comparison between satellite and model cloud cover trends during summer.** Linear trend (total change) in JJA cloud cover during 1995-2015 using 1°bins to calculate the mean for each degree. A) Latitudinal mean of the total JJA cloud cover change from the Clara-A2 dataset using the AVHRR sensor (Karlsson et al. 2017), MAR and RACMO. B) Same a A) but for the longitudinal mean of JJA cloud cover trends.

(green line) than in MAR and RACMO (orange and blue). On average, RACMO has a slightly lower difference in latitudinal mean cloud cover trends, with an underestimation of cloud cover reductions of 0.4%, compared to 0.7% in MAR. Further, the maximal difference between a 1° mean in RACMO and AVHRR is 1.2%, while it is slightly greater in MAR with 1.5%.

A similar pattern evolves when looking at the longitudinal differences between observations and RCMs. On average, RACMO has a slightly lower mean deviation from the satellite observations with 0.3% compared to 0.7% in MAR, with a maximum difference of 2.8% (RACMO) and 4.1% (MAR). Overall this analysis further demonstrates that both models underestimate melt season cloud cover reductions and that MAR underestimates it more than RACMO, potentially explaining some of the biases in the surface energy budget comparisons (Fig.(4.3)-(4.6)).

MAR and RACMO both underestimate cloud cover trends when expressed as a longitudinal mean but also when compared to the latitudinal mean of the satellite observations (Fig.(4.9)). However, the differences are greater when looking at the longitudinal means (Fig.(4.9) B). This greater difference in the longitudinal means indicates that the models not only underestimate the cloud cover trends, but also shifting their respective trends along the east-west axis. This amplified difference in cloud cover trends in the meridional analysis could be due to inaccuracies in representing the interaction between the synoptic-scale flow and the Greenland Ice Sheet. Given that the Greenland Ice Sheet is dominated by a N-S facing ridge or plateau, slightly shifting the sinking or rising motion eastwards or westwards also leads to greater errors in the resulting cloud cover trends. The connection between errors in cloud cover and the topography-flow interaction is further strengthened by the fact the the maximum in difference in Figure (4.9) B lies at or near the interior plateau of the Greenland Ice Sheet (between -35 and -50° Longitude).

4.4.5 Water vapour

The atmospheric water vapour content is of first-order importance for the formation of clouds and the efficiency of the atmosphere to emit longwave radiation. The mean annual cycle of Precipitable Water Vapour (PWV) observed at Summit Station is shown in Fig.(4.10) A (green) (Miller et al. 2015; Miller et al. 2017). It shows a distinctive peak during the melt season (July) when the atmosphere is the "warmest" and can hold more water vapour. Conversely, the PWV is a factor of ≈ 4 lower during the cold and dry winter months.

Both MAR and RACMO show a similar annual PWV cycle (Fig.(4.10) A, blue, orange). However, both slightly overestimate the PWV, MAR by 0.15 mm and RACMO by 0.14 mm (or roughly by 5%). When comparing the variability of modelled monthly mean PWV to the

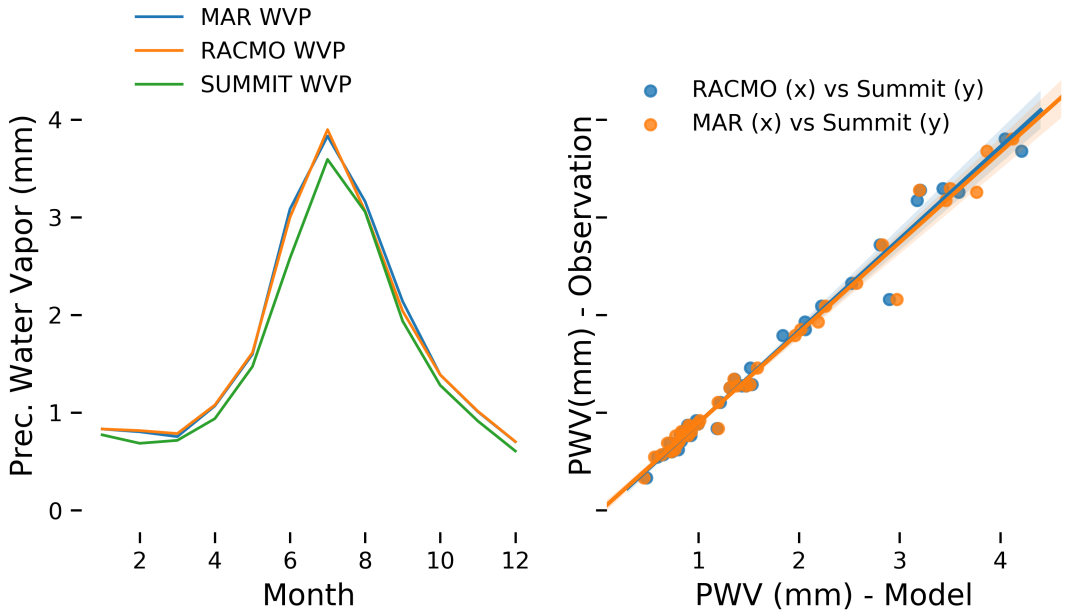

Figure 4.10: **Comparison between observed and modelled atmospheric water vapour in the interior of the GrIS.** A) Comparison of Summit observations (Miller et al. 2015; Miller et al. 2017) with MAR and RACMO annual cycle of atmospheric precipitable water vapour (PWV). B) Correlation between observed (Summit) PWV and modelled PWV (RACMO, MAR): $R^2_{MAR} = 0.93$ and $R^2_{RACMO} = 0.93$.

observations (Fig.(4.10) B), it shows that MAR and RACMO both correlate strongly with the measurements, both explaining 93% of variability of the in-situ observations (R^2). To summarise, both MAR and RACMO outputs agree very well with in-situ PWC observations, and they capture the annual PWV cycle.

4.5 Discussion

I have demonstrated that MAR and RACMO capture key characteristics of cloud cover trends and behaviour, compared to satellite observations. Both models agree that the main external driver of the SEB over the last two decades has been an increase in downwelling shortwave radiation, with MAR modelling a 21% higher increase in downwelling shortwave radiation than RACMO. These changes in the SEB are a direct consequence of large-scale decreases in JJA cloud cover. Furthermore, the changes in melt season cloud cover are well captured by both models when compared to spatial trends of JJA cloud cover from the CLARA-A2 dataset (Karlsson et al. 2017). However, both models slightly underestimate the magnitude of these reductions in cloud cover, with MAR modelling a 0.7% too low trend compared to 0.3% in RACMO.

And yet, despite a too low reduction in cloud cover, MAR SWD anomalies are greater than RACMO's over the 1995-2015 period, indicating that cloud microphysical properties might change differently in both models. This is not surprising, given that MAR and RACMO incorporate cloud microphysical schemes of different complexities. While MAR uses a one-moment scheme that only predicts the temporal evolution of one cloud variable (mixing ratio (Gallée 1995)), RACMO uses a more sophisticated two-moment scheme that predicts two cloud microphysical variables, which is essentially based on the physics package cycle CY33r1 of the European Centre for Medium-Range Weather Forecasts Integrated Forecast System (ECMWF (ECMWF 2009; Noël et al. 2018)).

Furthermore, the comparison with radiative fluxes from 23 AWS stations from the PROMICE network shows that both models are able to model the daily radiative fluxes of the SEB, however RACMO outperforms MAR in most of the statistical metrics (especially in the shortwave radiation). MAR underestimates incoming shortwave radiation when compared to the in-situ observations, but models a greater increase than RACMO when looking at GrIS wide anomalies. However, given that only one station over the Greenland Ice Sheet measures cloud microphysical properties, it is unclear whether the conclusion that RACMO performs better than MAR when compared to in-situ radiation measurements is due to a more sophisticated cloud microphysics scheme. Given that both models show a similar deviation from the observed trends in JJA cloud cover, one possible reason for this could be that biases in RACMO cloud cover and microphysics simply compensate each other better than in MAR.

Additionally, our analysis also raises the question whether it is more important for regional climate models to capture temporal trends, rather than the absolute daily values of the surface energy budget components. The mean biases when compared to the absolute values of observed radiative fluxes between the models differ by up to 16.6 W/m^2 (Fig.(4.3)). This is a significant difference, given that the radiative forcing causing global temperature rise is due to an increase in surface the energy budget of around 1.5 W/m^2 (Church et al. 2013). However, when looking at the temporal changes, the two models only disagree by 0.69 and 0.31 W/m^2. Therefore, our results indicate that it might be more important that RCMs capture changes in the surface energy budget to accurately model the subsequent impacts upon melt and surface mass balance dynamics. Therefore, it might be useful to define transient RCM climate metrics similarly to the Equilibrium Climate Sensitivity (ECS) for GCMs, to know the sensitivity of RCMs to changes in the SEB, rather than only validating RCMs against absolute values of observed daily radiative fluxes.

Furthermore, both models also use different radiative schemes, and therefore significant parts of the biases compared to the radiation observations could also be to the differences in the radiative transfers schemes of the models. To develop these RCMs further, it would be of first order importance to have a denser network of in-situ cloud microphysical observations. Currently, the GrIS is only monitored by one single station at Summit (Miller et al.

2015; Miller et al. 2017). Furthermore, active satellite sensors such as Cloudsat-Calipso lack the spatial coverage for a GrIS wide comparison of cloud parameters, while passive sensors (AVHRR, MODIS) only work reliable during sunlit periods and a limited number of parameters (cloud cover). Therefore, while this study highlights areas where regional climate models over polar regions can be significantly improved, the sparse data coverage could prove to be a significant bottleneck.

Chapter 5

Decreasing cloud cover drives the recent mass loss on the Greenland Ice Sheet

5.1 Preface

The previous chapter has explored the accuracy of polar regional climate models in their representation of clouds and the Greenland surface energy budget. It has established, by partitioning the anomalies of the Greenland Ice Sheet surface energy budget, that downwelling shortwave radiation has been the main external contributor to the surface energy budget over the last two decades. Furthermore, the previous chapter shows that polar regional models can accurately reproduce temporal trends in melt season cloud cover over Greenland. Subsequently, we conclude that high-resolution regional climate models are a useful tool to study in more detail the effect of recent trends in cloud cover over Greenland. The impact of this reduction in cloud cover since the mid-1990s upon the increasing rate of mass loss of the Greenland Ice Sheet will be explored in more detail in the following chapter.

For large parts the following chapter has been published in *Science Advances* under the citation: **Hofer, S., Tedstone, A. J., Fettweis, X., Bamber, J. L. (2017). Decreasing cloud cover drives the recent mass loss on the Greenland Ice Sheet. Science Advances, 3(6), e1700584. DOI: 10.1126/sciadv.1700584.**

Overall, only very minor adjustments have been made to the published paper. Supplementary material has been added in-line and the Data and Methods chapter has been moved to the main part of the manuscript, just after the Introduction chapter. The author contributions from this paper are as follows: *"S.H. analyzed the data and wrote the manuscript. S.H.,*

J.L.B., and A.J.T. designed the study and methods. J.L.B. supervised the project. X.F. developed and provided the daily climate model output as well as additional analyses. A.J.T. provided some of the code for the analysis."

5.2 Abstract

The Greenland ice sheet (GrIS) has been losing mass at an accelerating rate since the mid-1990s. This has been due to both increased ice discharge into the ocean and melting at the surface with the latter being the dominant contribution. This change in state has been attributed to rising temperatures and a decrease in surface albedo. Here we show, using satellite data and climate model output, that the abrupt reduction in surface mass balance since about 1995 can be largely attributed to a coincident trend of decreasing summer cloud cover enhancing the melt-albedo feedback. Satellite observations show that, from 1995 to 2009, summer cloud cover decreased by 0.9% ± 0.3%.yr. Model output indicates that the GrIS summer melt increases by 27 ± 13 Gt per percent reduction in summer cloud cover, due principally to the impact of increased shortwave radiation over the low albedo ablation zone. The observed reduction in cloud cover is strongly correlated with a state shift of the North Atlantic Oscillation promoting anticyclonic conditions in summer and suggests that the enhanced surface mass loss from the GrIS is driven by synoptic-scale changes in Arctic-wide atmospheric circulation.

5.3 Introduction

The mass balance of the GrIS has changed significantly over the last two decades. Until the mid-1990s, losses from surface meltwater runoff and ice discharge into the ocean (D) were roughly balanced by snow accumulation (Van den Broeke et al. 2009; Van den Broeke et al. 2016; Van den Broeke et al. 2017). Since then, however, mass loss has accelerated (Wouters et al. 2013) as the surface mass balance (SMB) has declined and D has increased (Van den Broeke et al. 2009), with a possible link between meltwater production and ice dynamics (Rignot et al. 2008; Bamber et al. 2012). As a consequence, the GrIS has become the dominant source of barystatic sea level rise, with an average (1991-2015) contribution of 0.47 ± 0.23 mm/a (equivalent to 171 Gt of ice) (Van den Broeke et al. 2016). About 60% of this recent mass imbalance has been associated with a declining SMB due, predominantly, to enhanced surface melt (Van den Broeke et al. 2009; Van den Broeke et al. 2016). Studies based on in-situ observations suggest that surface melt rates are controlled by variations in summertime shortwave (SW) radiation (Van den Broeke et al. 2011; Van de Wal et al. 2005). To date, however, only the impact of a declining albedo (α) on the SW radiation budget (Eq.

5.1) has been considered (Box et al. 2012; Dumont et al. 2014).

$$SW_{net} = SWD \cdot (1 - \alpha) \tag{5.1}$$

It has previously been suggested that cloud cover has a positive feedback on melt rates by controlling longwave fluxes (Van Tricht et al. 2016). Here, we use a combination of satellite cloud data and modelled radiation fluxes to assess the impact of recent changes in GrIS cloud cover upon radiative fluxes and, in turn, the SMB of the GrIS.

5.4 Study design, regional climate models and cloud remote sensing data

5.4.1 Experimental Design

We chose to base our analysis on the fact that for the observed melt-induced reduction of the SMB on the order of 103 Gt since the mid-1990s (Van den Broeke et al. 2009; Van den Broeke et al. 2016) significant amounts of extra energy are required. Therefore, this deviation from the stable state before the mid-1990s has to be depictable as a large-scale deviation from the long-term mean in energy fluxes toward the ice surface or atmospheric variables (that is, precipitation). Because most of Greenland's melt occurs during the three summer months (JJA) and studies based on in situ observations clearly show that variations in SW radiation dominate SMB variability (Van den Broeke et al. 2011; Van de Wal et al. 2005), we tested the hypothesis that incoming SW radiation (that is, reduced cloud cover) is partly causing these changes in the net SW balance, along with the observed reduction in surface albedo (Box et al. 2012; Dumont et al. 2014), with a possible link between the two (Box et al. 2012). Wherever possible, we therefore converted radiation and heat flux anomalies to a melt potential, using the heat of fusion to melt 1 kg of ice, H_f= 333.55 kJ/kg, to make a direct comparison with melt anomalies as much as possible. We acknowledge the fact that this is an oversimplification of the physical processes involved as some of the additional energy may heat up the snowpack rather than directly influencing melt (and therefore, SMB). However, if parts of our presented energy surplus are used for processes such as heating the snowpack, then the correlation between melt potential (radiation and heat flux anomalies) and melt anomalies in our analysis will decrease, and therefore, our results represent a cautious estimate of the actual contribution to Greenland's melting signal

5.4.2 Modèle Atmosphérique Régional (MAR)

The MAR used in this study is a hydrostatic regional climate model that solves the atmospheric primitive equation set [refer to the studies of Gallée and Schayes (Gallée et al. 1994) and Fettweis (Fettweis 2007) for a detailed description of the model]. MAR version 3.5.2 was used here (Fettweis et al. 2017).It was forced at its lateral boundaries every 6 hours by the ECMWF ERA-Interim (1979–2015) and ERA-40 data set (before 1979) (Dee et al. 2011), with the atmospheric forcing fields containing temperature, wind, humidity, and surface pressure. Sea ice cover and sea surface temperature were also prescribed every 6 hours. Therefore, in terms of cloud cover trends, it was independent of the (cloud) data assimilation of MODIS and AVHRR data into the ERA fields.

MAR was coupled with the multi-layered one-dimensional energy balance–based snowmodel SISVAT (Soil Ice Snow Vegetation Atmosphere Transfer), which is used for the connection between atmosphere, snowpack, sea, and permanent ice as well as the snow-covered tundra [for adetailed description of SISVAT, see the study of De Ridder and Gallée (De Ridder et al. 1998). The snow and ice related properties in SISVAT were calculated based on the snowmodel CROCUS (De Ridder et al. 1998; Gallée et al. 2001). The cloud scheme of MAR was based on Meyers et al.(Meyers et al. 1992) and on in situ measurements and subsequent model development during the Mixed-Phase Arctic Cloud Experiment (Fridlind et al. 2007) and was specially developed to depict Arctic cloud characteristics. The model setup and output of MAR were rigorously tested over the GrIS and tuned to match observed atmospheric and surface properties as closely as possible to depict trends in the SMB of the GrIS (Fettweis 2007; Fettweis et al. 2011). It was validated against other regional climate models (Fettweis et al. 2011), and it also showed good agreement with in-situ automatic weather station data and passive microwave remote sensing data (Fettweis et al. 2017; Fridlind et al. 2007; Fettweis et al. 2011). The model was run on an equal-area 25x25 km grid, whereas the temporal coverage of the data in this study spanned from 1979 to 2015, except for the climatological base state (1970–1995).

5.4.3 Computation of anomalies

The computation of anomalies from MAR (cloud cover, SMB, SW,longwave radiation components, etc.) was based on the 1970–1995 mean state of the model. If radiation and heat flux anomalies were not presented in the corresponding SI unit (joule), then we used the heat of fusion to melt 1 kg of ice, H_f= 333.55 kJ/kg, to convert the radiation anomaly in a corresponding mass anomaly ("melt potential"). A positive melt anomaly corresponds to an above-average downward flux of radiation and vice versa. For every pixel of the 25x25 km grid, first, a monthly arithmetic mean from the daily model output was computed for every grid cell. Then, a climatology was produced, on the basis of an arithmetic mean of

the period 1970–1995 for the specific month (January-December), and then, the deviation for every grid cell and individual month was computed as

$$a_{i,j,month} = x_{i,j,month} - \overline{x_{i,j,m}} \tag{5.2}$$

where $a_{i,j,month}$ is the deviation of the monthly values $x_{i,j,month}$ from the specific monthly grid cell climatology (second term in Eq.(5.2)),subscript $_{\text{i,j}}$ refers to the i-th row and j-th column of the model grid, and subscript $_{\text{m}}$ represents a fixed month for which the climatology was computed. If values of SMB anomalies were presented, we summed up (spatially) all the per-pixel deviations from the 1970–1995 mean state ($a_{i,j,month}$) over the GrIS model domain to obtain one value forthe specified time for the entire GrIS.

$$\Delta a_{total} = \sum_{i} \sum_{j} a_{i,j,month} \tag{5.3}$$

If radiation anomalies were presented, we first calculated the per-pixel deviations as given by Eq.(5.2) to obtain the deviation from the 1970–1995 mean in watts per meter square. Because every grid cell in the model configuration had a spatial coverage of 25x25 km, we multiplied this value by the grid-cell area to obtain the total deviation in watts (joules per second) per one grid cell. In the last step, we summed up all these values spatially (as in Eq.(5.3)) and multiplied it by the time of the month (in seconds) to get from joules per second to total deviation in joules.

5.4.4 MODIS cloud cover

The MODIS has been operational since 2000 on board two satellites, Aqua and Terra. It has a cross-track swath width of 2330 km and an along-track swath length of 10 km. It makes use of measurements at 36 different wavelengths, ranging from 0.4 to 14.4 μm, of which 14 are used to test whether clouds are present (Ackerman et al. 1998; Frey et al. 2008). Most of the tests are designed to identify contrast between clouds and the atmosphere or the surface. Here, we used the global, monthly fractional cloud cover product (MYD08_M3) (Platnick et al. 2015) from the MODIS sensor on board of the polar orbiting Aqua satellite, which was computed by summarizing the daily level 3 product over one calendar month (Hubanks et al. 2008). Cloud fraction within this data set was defined as the ratio between the sum of cloudy pixels and the total number of pixels within one grid cell. The measurement period available for this study ranged from 2002 to 2015. The spatial grid of the monthly cloud cover product was an equal-angle 1°longitude by 1°latitude grid, with the daily level 2 product (MOD06_L2) underlying the daily level 3 product that had a higher spatial resolution of 1 km (2 band at 250 m, 5 at 500 m and the remaining 29 bands were measured at resolution of 1 km) (Hubanks et al. 2008). For every 1°by 1°grid cell, all the underlying level 2 pixels were used to determine the cloud fraction over a period of 1 day and then were averaged

over 1 month (Hubanks et al. 2008). For the computation of cloud cover averages over the entire GrIS, data points were weighted on the basis of their latitude to take into account the meridian convergence toward the North Pole.

5.4.5 AVHRR cloud cover

The AVHRR is a broadband, four- to six-channel (depending on the sensor version) radiometer. The sensors have mostly been carried on different National Oceanic and Atmospheric Administration (NOAA) polar-orbiting satellites all forming a part of the Polar-Orbiting Environmental Satellites (POES). The monthly cloud cover retrievals were provided by EUMETSAT (European Organisation for the Exploitation of Meteorological Satellites)'s Satellite Application Facilityon Climate Monitoring (CM SAF). The CM SAF Global Area Coverage (GAC) Edition 1 data set provides an intercalibrated Climate Data Record (CDR) on fractional cloud cover based on AVHRR measurements, with the cloud characteristics (cloud fraction, cloud optical thickness, etc.) being produced with the Polar Platform System and the Cloud Physical Properties algorithms (Dybbroe et al. 2005b; Dybbroe et al. 2005a).The information of the data set used in this study was provided on a 0.25°by 0.25°equal-angle latitude-longitude grid, with the underlying level 2 GAC data having a spatial resolution of 4 km (Karlsson et al. 2013). The temporal range of the available cloud fraction CDR was from 1982 to 2009. The data set was mostly verified by cross-checking with data from weather stations (surface synoptic observation reports) but was also validated against MODIS observations, with the targeted bias-corrected root mean square error lying between 15% and 20% (Karlsson 2014). Newer AVHRR data were also available for 2009–2016, but they have not been processed to reach the status of an intercalibrated CDR yet. As in the previous subsection, if area averages from AVHRR were presented, data points were weighted on the basis of their latitude.

5.4.6 Comparison between MODIS and AVHRR

The main advantage of using MODIS and AVHRR data compared to earlier derived cloud climatologies is the wide spectral coverage and their relatively high spatial resolution (King et al. 2013). The International Satellite Cloud Climatology Project, for example, only used two spectral bands to detect clouds, one in the visible and one in the infrared, whereas the AVHRR cloud mask algorithm used six different bands. The higher resolution and number of spectral bands used in the MODIS product resulted in a more robust, but shorter-length, product than AVHRR. The detection limit for MODIS was found to be situated at a cloud optical thickness of $\tau \approx 0.4$ (Holz et al. 2009). The validation of MODIS cloud cover with the Cloud-Aerosol Lidar with Orthogonal Polarization (CALIOP) aboard the Calipso satellite, with a detection limit of $\tau \approx 0.1$, showed an overlap in 87% of cloud conditions (39).The

difference was mainly due to the superior detection capabilityby CALIOP of clouds with a cloud optical thickness between $\tau \approx 0.4$ and $\tau \approx 0.1$. Although the AVHRR cloud cover data set is less capable than MODIS, particularly in the detection of very thin clouds (and showing less total cloud amount), it is still capable of reproducing multi-annual cloud cover trends for all the other types of clouds. Its biggest advantage is its longer time range. The first measurement in the data set was taken in 1982 (compared to 2002 with MODIS Aqua).

5.5 Results

5.5.1 Trends in summer cloud cover

We use satellite-derived cloud products from (1) the MODIS sensor (Platnick et al. 2015) on-board NASA's Aqua satellite and (2) AVHRR (Karlsson 2014) to quantify cloud cover changes. We also use a regional climate model, MAR, forced by the European Centre for Medium Range Weather Forecasting Reanalysis (ERA), to assess the subsequent impact on SMB (Van den Broeke et al. 2009; Van den Broeke et al. 2016) (see Methods). Satellite observations reveal that there have been significant reductions in summertime (JJA) optically-thick cloud cover. Observations from AVHRR (Figure 5.1A) recorded reductions in cloud cover over 84% of Greenland's area over the time period 1982-2009. Over the same time period MAR shows a reduction over 82%. During the period 2002-2015 (Fig. 5.1B), observations from MODIS show a cloud cover decrease over 77% of Greenland's area, compared with 68% from MAR. Outputs from MAR show good agreement in the spatial distribution and amplitude of the changes observed by both satellite platforms. The largest reductions are seen in the warmer west and south of Greenland, whereas cloud cover increased in the colder and drier northeast. The decrease in cloud cover which occurred after 2002 is relatively large, with substantial parts of southern Greenland experiencing a reduction of more than 10%. These cloudiness changes are a direct response to the circulation changes observed since the end of the 1990s (Fettweis et al. 2013a). As shown in Fig. 5.1 A, B (bottom), these circulation changes favour more anticyclonic conditions (warm and dry) over the south of Greenland except in the North-East where they favour southward fluxes (wet and cold), explaining the cloudiness increase in this area. During 1982-2009, the increases in geopotential height of the 500 hPa pressure level (Z500) promoted more anticyclonic conditions over most of Greenland while for 2002-2015, the Z500 increases are limited to the west coast.

Though the spatial distribution of cloud cover is similar between MAR and the observations, the model slightly overestimates the area with cloud cover increase (32%) compared to the observations (23%). Nonetheless, the MAR trends and behaviour are suitable for exploring the role that changing cloud cover has had on surface melt and, in turn, the SMB of the ice sheet.

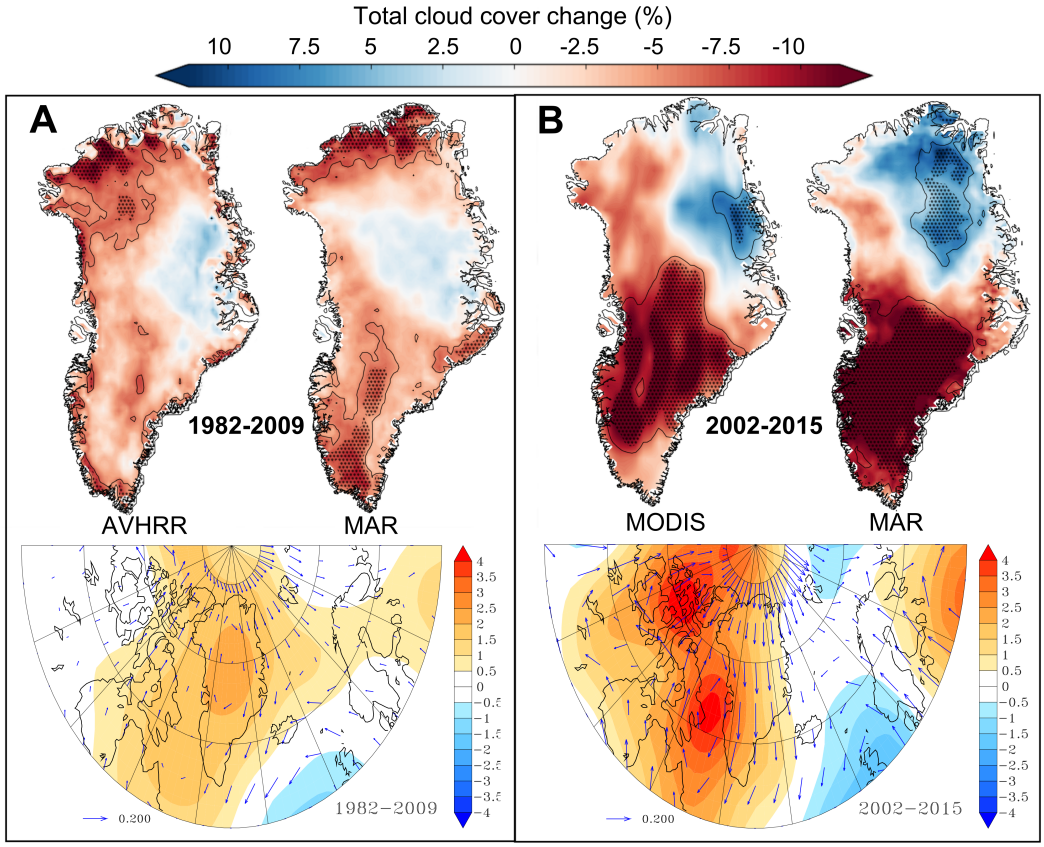

Figure 5.1: **Total change in summer (JJA) cloud cover from satellites and a regional climate model.**
(A), comparison between AVHRR (ref.(Karlsson 2014), left, top) and MAR (right, top) total JJA cloud cover change (%) during the full available data period of AVHRR between 1982-2009. Below: Trend of JJA 500hPa Geopotential height (Z500) in m/yr. The arrows show the wind trend in m/s/yr and highlight the circulation anomalies induced by the JJA Z500 changes. The arrow length of a change of 0.2 m/s/yr is given in the legend for indication. (B), the same as a, but for MODIS (ref.(Platnick et al. 2015), left, full observation period 2002-2015) and MAR (right, 2002-2015). Values inside black line have significance level of $p < 0.10$, dotted areas indicate statistical significance with $p < 0.05$.All cloud cover trends are based on a linear regression analysis for every pixel individually.

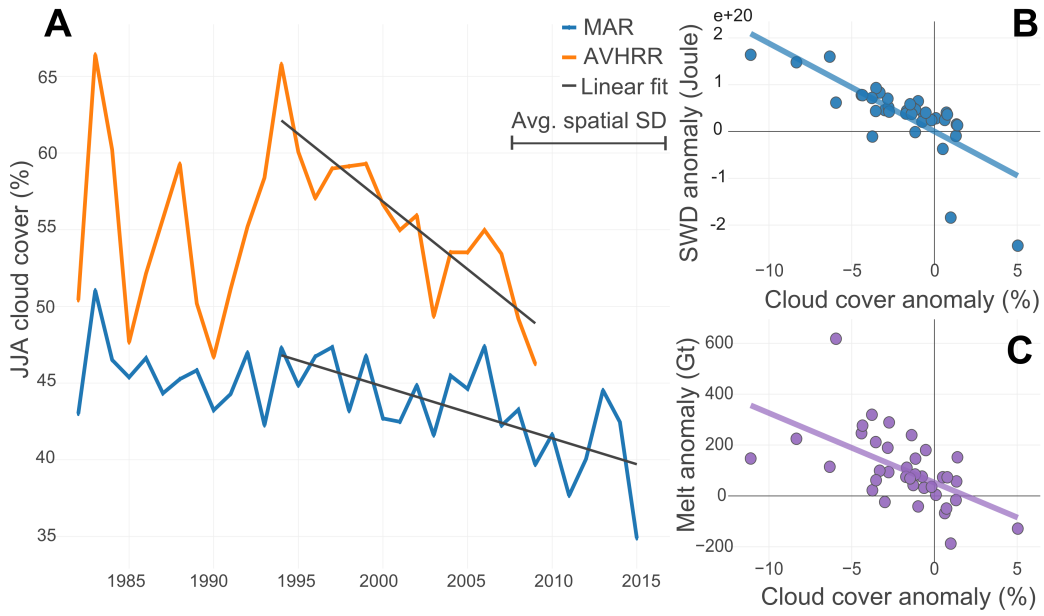

Figure 5.2: **Summer (JJA) cloud cover time series, trends and impacts of clouds on melt and radiation.**
(A), time series of average Greenland cloud cover from AVHRR sensor (orange, 1982-2009) and MAR (blue, 1982-2015). Linear fit (dark grey): AVHRR (1994-2009) R^2=0.76, $p < 0.001$, MAR (1994-2015) R^2=0.46, $p < 0.001$. Length of one average spatial standard deviation is shown in the legend. (B), correlation between MAR JJA cloud cover anomaly and JJA SWD anomalies (R^2=0.58, $p < 0.001$). (C), correlation between JJA cloud cover anomalies and JJA melt anomalies (R^2=0.32, $p < 0.001$). All anomalies in (B) and (C) are calculated based on the 1970-1995 average.

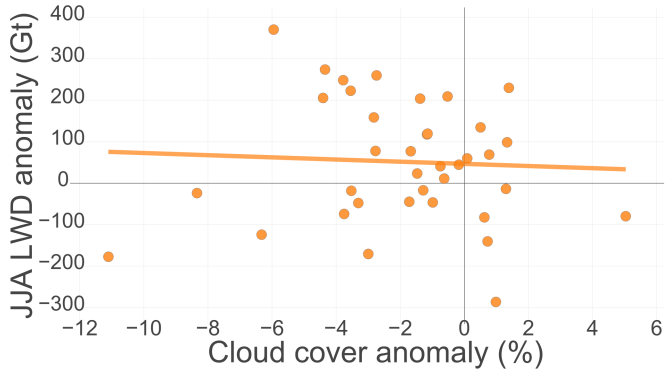

Figure 5.3: **Correlation between JJA cloud cover and LWD anomalies.** Scatterplot and linear regression line of JJA cloud cover anomalies (%) and JJA longwave downward anomalies (Gt) (R^2=0.003, p=0.1).

Figure 5.2A (orange line) shows the average JJA cloud cover retrieved from AVHRR over Greenland from 1982-2009. It is characterized by two phases: From 1982 until 1994 there is high inter-annual variability (SD = 6.1%) and no statistically significant trend. Around 1995, the behavior changes as a result of changes in general circulation reflected in a decreasing JJA NAO index (Fettweis et al. 2013a). The detrended inter-annual variability (SD = 2.3%) decreases by more than half and the cloud cover shows a statistically significant negative trend between 1994 and 2009 (-0.9± 0.28% per year, $p < 0.001$, $R^2 = 0.76$). The total change in cloud cover is -14.1%, which is larger than the average spatial SD (10.1%) and markedly above the inter-annual variability. This coincides with a shift in the North Atlantic Oscillation (NAO) to an extremely negative, and with a shift in the Greenland Blocking Index (GBI, ref. (Hanna et al. 2016)) to an extremely positive state (Fig.5.8 and 5.9) which appears anomalous for at least the last 160 years. These anomalies in both indexes suggest a higher frequency of anticyclonic conditions over Greenland, where the NAO index is susceptible to changes in mean surface pressure conditions over the North Atlantic (Fettweis et al. 2013a), while the GBI is proportional to the general circulation directly over the GrIS at the 500 hPa level (Hanna et al. 2016). Figure 5.2A (blue line) presents the average JJA cloud cover from MAR. It also shows a statistically significant trend from the mid-1990s to 2015, but less marked (-0.3 ± 0.17% per year) and the total change during the period is –6.1%, which is below the spatial variability (10.4%), but above the detrended inter-annual variability of 2.3%. The underestimation of cloud cover decline appears to be a consequence of the overestimation of the spatial extent of cloud cover increase (1982-2009: 2% of Greenland, 2002-2015: 9%) when comparing MAR to the observations (Fig. 5.1). These differences are likely due to small biases in temperature, humidity and wind simulated by MAR and the non-linear behaviour of simulated cloud cover in regional climate models.

5.5.2 Sources of increase in melt

Based on the correlation between JJA cloud cover and JJA shortwave downward (SWD) radiation anomalies (Figure 5.2B) we find that, for every percent of negative JJA cloud cover anomaly, Greenland receives 1.9 ± 0.6 x 10^{19} J of extra SWD energy during summer melt season. We also find that for every percent of JJA cloud cover reduction the melt during summer is enhanced by 27 ± 13 Gt (Fig. 5.2C). Next, we partitioned melt anomalies estimated by MAR into their different contributions (Fig. 5.4), converting radiative flux anomalies from Joules into melt potential (Gt) wherever applicable (see Experimental design).

Fig. 5.4A shows the accumulated, annual MAR melt anomalies, with a strong positive trend (more melt) from about 1995, resulting in an accumulated melt anomaly of +3971 Gt between 1995 and 2015, in good agreement with other studies (Van den Broeke et al. 2009; Van den Broeke et al. 2016; Van den Broeke et al. 2017). We find a strong increase in both, SWD (+4112) and SWnet (+3737 Gt) JJA anomalies during the same period. While the

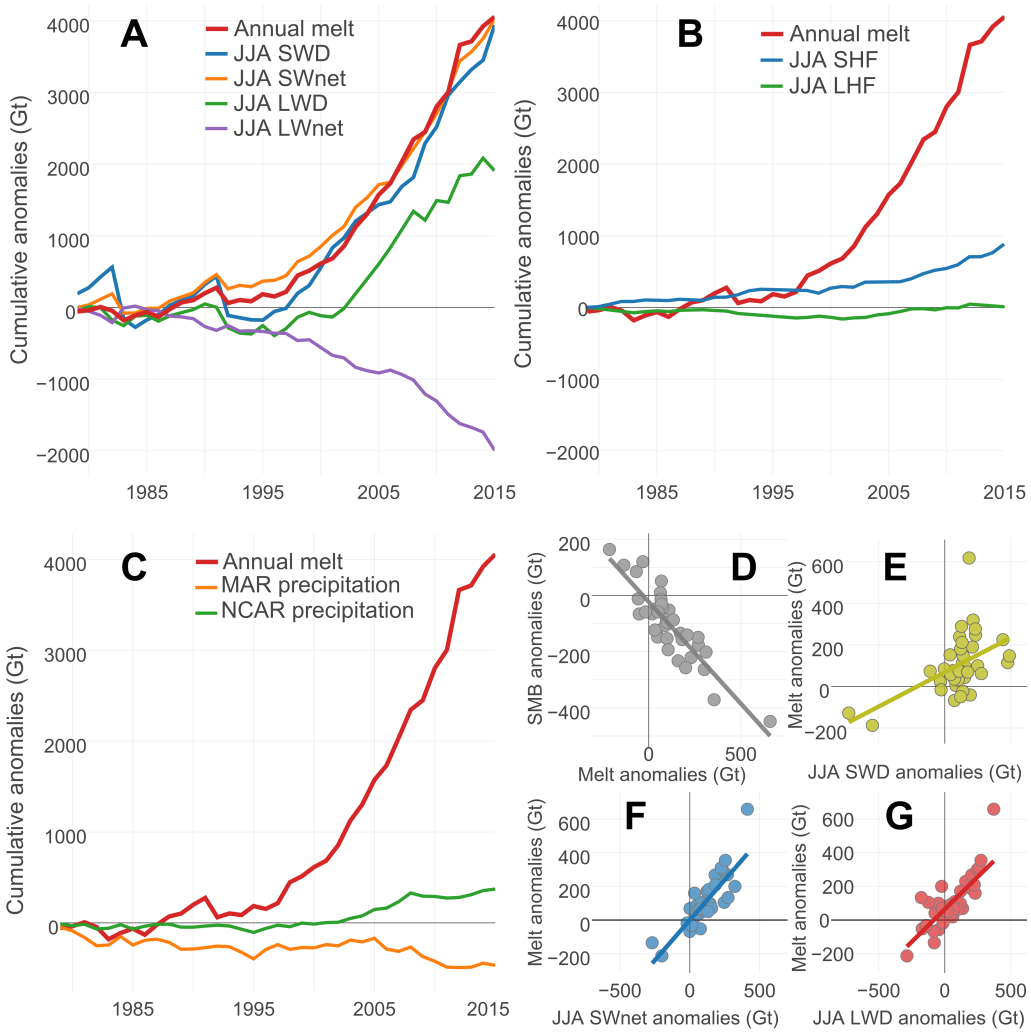

Figure 5.4: **Accumulated melt anomalies and contributing factors.**(A), accumulated annual melt anomalies (Gt) and JJA SWD, SWnet, LWD and LWnet anomalies. Radiation anomalies converted from Joule to 'melt potential' (Gt) (**see methods**). Anomalies are based on the 1970-1995 average of MAR (**Eq. (2)**) and the accumulation of anomalies starts in 1979. (B), same as A), but showing JJA latent (LHF) and sensible heat flux (SHF). (C), accumulated annual precipitation anomalies (MAR and NCEP v1 reanalysis) and annual melt anomalies. (D), correlation between annual melt anomalies and annual SMB anomalies (R^2 = 0.77, p < 0.001). (E), correlation between JJA SWD anomalies and melt anomalies (R^2 = 0.26, p < 0.001). (F), correlation between JJA SWnet anomalies and melt anomalies (R^2 = 0.75, p < 0.001). (G), correlation between JJA LWD anomalies and melt anomalies (R^2 = 0.63, p < 0.001).

increase in SWD is fully driven by the decrease in cloud cover during summer, the increase in SWnet is both a result of the increase in SWD (reduced cloud cover) and the coinciding decrease in surface albedo (Dumont et al. 2014; Van Tricht et al. 2016).

We also find that the increase in JJA longwave downward (LWD) radiation anomalies , which is directly proportional to the free atmospheric temperature in summer and global warming, has contributed less to the energy balance over the GrIS than SWD anomalies (+2277 Gt vs +4112 Gt). We also find that LWD anomalies are not sensitive to summer cloud cover anomalies (Fig.(5.3), $R^2 = 0.003$). The negative anomalies in LWnet radiation (-1669 Gt) indicate that the surface of the GrIS has recently been warming more than the atmosphere because of the combined effect of increased shortwave and longwave radiation reaching the surface.

The exceptional melt of the GrIS since the mid-1990s seems therefore to be a result of increases in both of the 'external' drivers of the surface energy balance, LWD and SWD. While previous studies have focused on the role of rising temperatures as the main cause of the current melt increase and albedo decline over the GrIS (e.g. (Tedesco et al. 2013; Tedesco et al. 2016)), our results strongly indicate that it rather is a combination of increased SWD due to reduced cloud cover in summer combined with an increase in LWD due to higher free atmosphere temperatures that causes melt and surface darkening. Therefore, the decrease in surface albedo because of the melt-albedo feedback (Box et al. 2012), which increases surface melt by increasing the ratio of absorbed solar radiation, has also been partly driven by a recent decrease in summer cloud cover enhancing the melt-albedo feedback (see also Fig.(5.5)) and not only by temperature anomalies.

Other studies have indicated that in the western ablation zone non-radiative energy fluxes can play a significant role in enhancing short-term melt events (Fausto et al. 2016). While this can be the case for specific events on a small spatial and temporal scale, our results (Fig. 5.4B) indicate that over longer time periods and over the whole GrIS, sensible and latent heat flux have contributed very little extra energy to the surface energy increase of the GrIS (+630 Gt and +119 Gt respectively). In order to exclude the possibility that changes in precipitation patterns have contributed to the recent decline in SMB, we have analyzed two independent datasets of precipitation over Greenland (Fig. 5.4C). While MAR driven by ERA-reanalysis shows a slightly negative precipitation trend (-143 Gt), NCEP reanalysis indicates marginal precipitation increase between 1995 and 2015 (+446 Gt).

Our results also show that melt anomalies are the main factor in controlling total annual SMB anomalies (Fig. 5.4D). MAR indicates that 77% of the variability in SMB anomalies is controlled by melt anomalies, while melt anomalies are the main driver of meltwater runoff anomalies from the GrIS ($R^2 = 0.98$, Fig.(5.6)). This agrees with finding of van den Broeke (2009) and (2016) (Van den Broeke et al. 2009; Van den Broeke et al. 2016; Van den Broeke et al. 2017) who used gravimetry and climate model data to show that surface

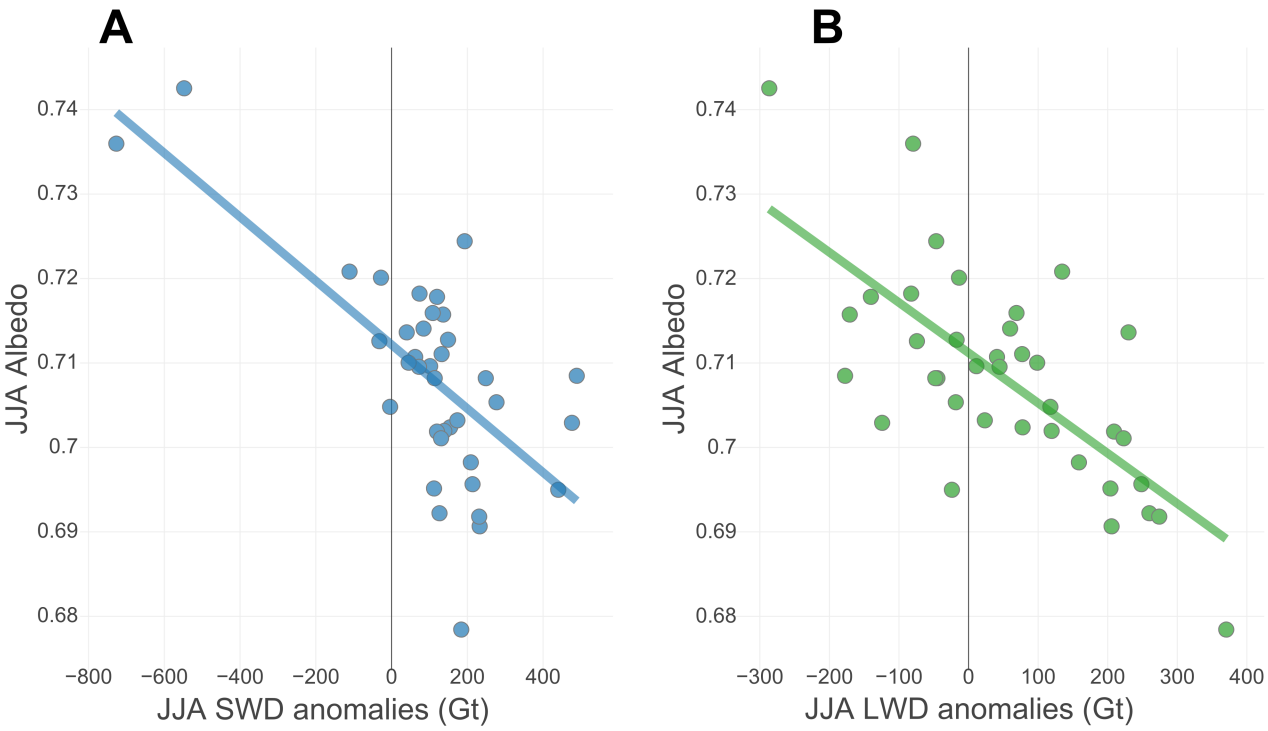

Figure 5.5: **Correlation between summer radiation anomalies and albedo.**(A), correlation between JJA SWD anomalies since 1979 and GrIS summertime albedo (R^2=0.46, p<0.001), based on the 1970-1995 climatological mean of MAR, (B), same as A) but showing JJA LWD anomalies and summertime albedo correlation (R^2= 0.50, p<0.001).

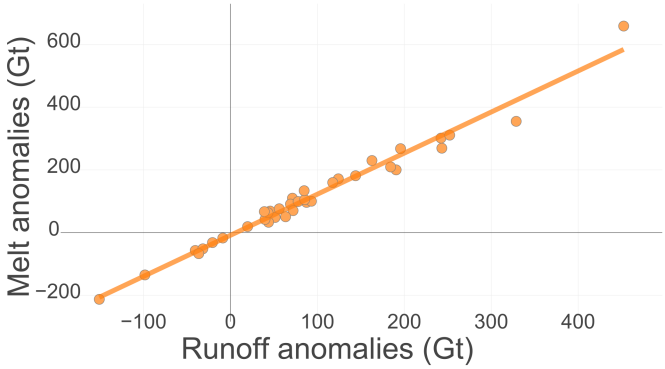

Figure 5.6: **Correlation between annual melt and runoff anomalies.** Scatterplot of annual melt anomalies against annual runoff anomalies, based on the 1970-1995 average of MAR (R^2= 0.98, p<0.001).

melt anomalies are the main driver of the recent mass loss from the GrIS. We also find that summertime SWD anomalies, due to a reduction in cloud cover, directly explain 26% of the variability in melt anomalies (Fig. 5.4E). JJA SWnet anomalies show an even stronger correlation with summertime melt anomalies, explaining 75% of the variability (Fig. 5.4F). In reality, parts of this strong correlation are also a manifestation of SWD anomalies, because under sunny conditions the albedo of the GrIS is automatically lower than under overcast conditions, because clouds filter out parts of the spectrum where the surface albedo is very low (near-IR,(Warren 1982)). This direct effect of clouds on the albedo is accounted for in MAR's albedo scheme but does not show up in the correlation between melt and SWD anomalies. JJA LWD anomalies (Fig. 5.4G), although smaller in magnitude than SWD and SWnet, also show significant overlap with summer melt anomalies ($R^2 = 0.63$). This effect is a direct consequence of arctic free-atmosphere temperature increase. However, because the emissivity of the atmosphere, ϵ, is higher in cloudy conditions, the decrease in summertime cloud cover might have had some dampening effect on global warming and associated increase in LWD (the increase in LWD is lower in Fig. 5.4A during phases with high SWD and vice versa).

5.5.3 Influence of large-scale circulation patterns

Fettweis et al.(Fettweis et al. 2013a) reported on the importance of an anomalously low North-Atlantic-Oscillation (NAO) index during summer and a subsequent increase in high-pressure frequency over Greenland. Synoptic-scale ridges in the mid-troposphere and high-pressure systems near the surface lead to large scale sinking motion, which enhances cloud dissipation, leading to reduced cloud cover. The 5-year average of the NAO index has not been consistently negative since around 1960 ((Barnston et al. 1987), Fig.5.8). The extended Greenland Blocking Index (GBI) time series (Fettweis et al. 2013a) (Fig.5.9) indicates it reached its highest values in the 2000s: a high that has not been seen since 1850 (>3 SD outside the mean).

We find that these changes in synoptic-scale circulation patterns and the associated increase in high-pressure frequency over Greenland (Fettweis et al. 2013a) correlate strongly with changes in summertime cloud cover ($R^2 = 0.75$, $p < 0.001$, Figure 5.7A, B). For every 0.2 decrease in JJA NAO index, gauging the general circulation at the surface over the North Atlantic, the JJA cloud cover has reduced by 0.88% ± 0.16%, with times of especially low cloud cover such as 2010-2015 coinciding with a very negative NAO. There is also strong agreement between the JJA Greenland Blocking Index (14), representative of the general circulation at 500 hPa over the GrIS, and JJA cloud cover (Fig. 5.7A, C, $R^2 = 0.74$, $p < 0.001$), confirming that the decrease of cloudiness over Greenland is due to synoptic-scale circulation changes and in particular due to the increase of anticyclonic conditions over Greenland for which GBI is particularly sensitive. This strong correlation between summer-

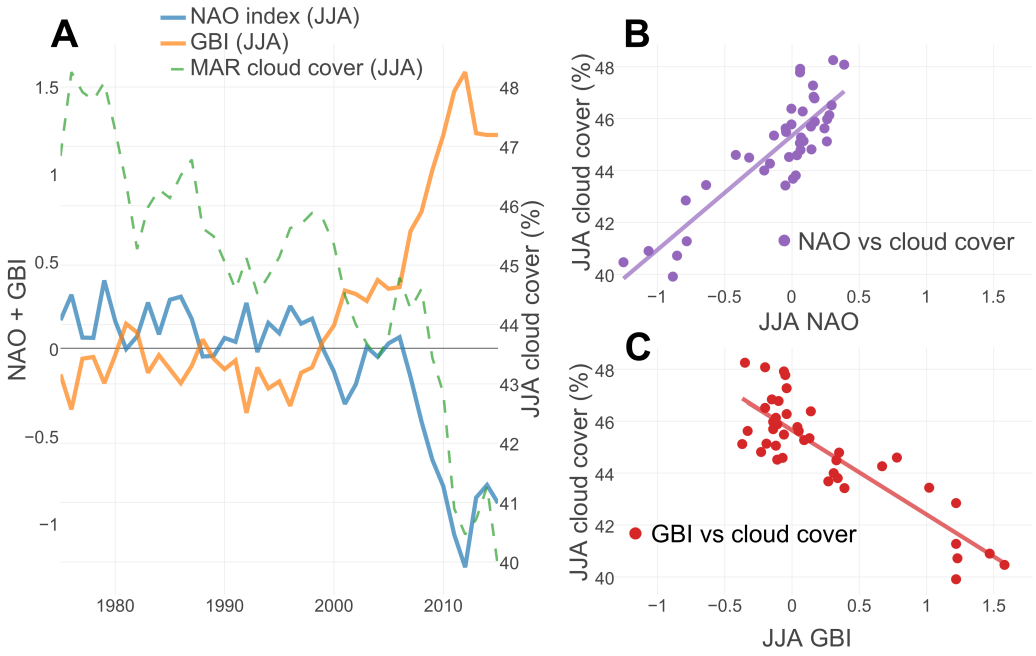

Figure 5.7: **Correlation between cloud cover (model) and measured NAO/GBI index during summer (JJA).** (A), 5 year running average of MAR JJA cloud cover (green, %), JJA NAO index (blue) and JJA Greenland Blocking Index (orange). (B), the scatterplot (purple) shows the correlation (R^2=0.75, $p < 0.001$) between observed NAO index and MAR cloud cover (both for JJA). (C), the scatterplot (red) shows the correlation (R^2=0.74, $p < 0.001$) between Greenland Blocking Index (GBI) and MAR cloud cover (both for JJA).

time NAO index and the MAR-based cloud cover could be used to forecast if the observed reduction in cloud cover during summer, and the associated increase in GrIS melt, are likely to continue. If it is linked to global warming and the poleward migration of large-scale circulation patterns (Norris et al. 2016), then global circulation models (GCMs) could be used to test this hypothesis. However, Franco et al.(Franco et al. 2013) have reported that GCM forced regional climate models show an opposite trend in SW radiation compared to when they are driven by reanalysis data because GCMs do not project change in general circulation over Greenland. It is interesting to note that only one of the CMIP5 GCMs simulates the recent extreme low in NAO index (Fettweis et al. 2013a) and this extreme negative phase continues throughout the 21st Century (Fettweis et al. 2013a).

5.5.4 Circulation anomalies in long term context

We also find that the anomalies in the synoptic-scale circulation lie outside the natural, internal variability of the climate system. Looking at the extended NAO and GBI time series (Fig. 5.8 and 5.9), going back to 1950 and 1850 respectively, we find that the observed anomalies are more than three standard deviations outside the long-term mean. Assuming normally distributed internal variability around the mean state, the probability to observe such deviations is less than 0.03%. Current research suggests, that recent circulation anomalies are

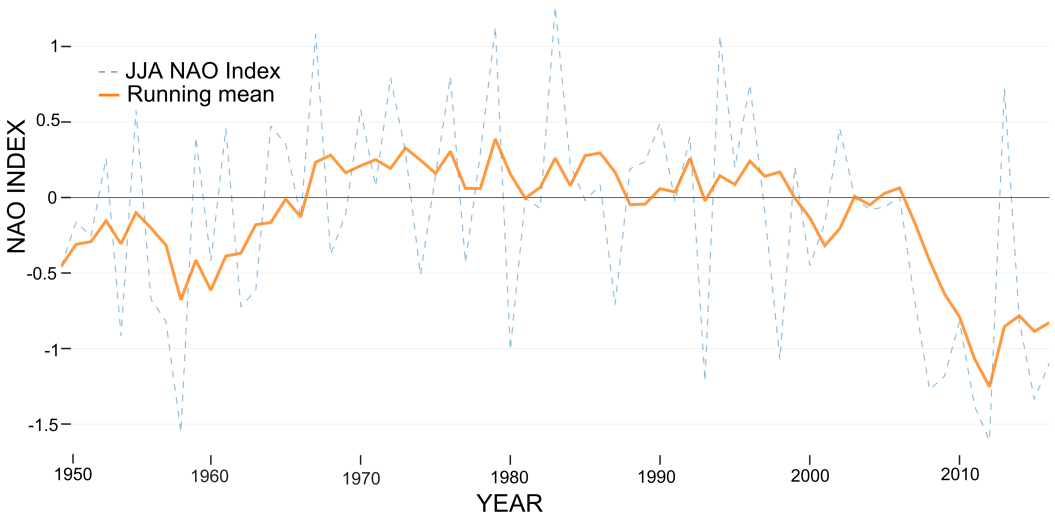

Figure 5.8: **Long-term NAO index from observations on Iceland and the Azores (1950-2016)**. Average JJA NAO index (blue) and 5 year running average (orange) retrieved from observations from the Azores (Ponta Delgada) and Iceland (Reykjavik) (Barnston et al. 1987).

closely linked to rapidly declining sea ice extent, which enhances ocean-atmosphere heat transport, weakens near-surface inversions and has therefore a controlling influence upon tropospheric circulation and even on the stratospheric polar vortex (Screen et al. 2010;

Screen et al. 2013). A second influencing factor could be the slowing down of the Atlantic Meridional Overturning Circulation (AMOC), leading to below-average sea surface temperatures (SSTs) in the North Atlantic, with a feedback upon tropospheric conditions (Rahmstorf et al. 2015; Caesar et al. 2018). However, due to the complex nature of the climate system it might also be possible that remote teleconnections between the Tropics and the Arctic, or that changes in the Polar Vortex might lead to an anomalous state of the tropospheric circulation. Furthermore, it has recently been shown by Hanna et al. (2018) that none of the CMIP5 models captures the current anomalous state of the North Atlantic Oscillation. Because the current suite of the GCMs are not able to simulate these circulation anomalies, their ability to predict the future evolution of the Greenland Ice Sheet are highly questionable (Hanna et al. 2018). Overall, looking at the long term evolution of the GBI and the NAO leads to the conclusion that it is highly likely that the current state of the synoptic-scale circulation over Greenland lies outside the nature variability of the Arctic climate system.

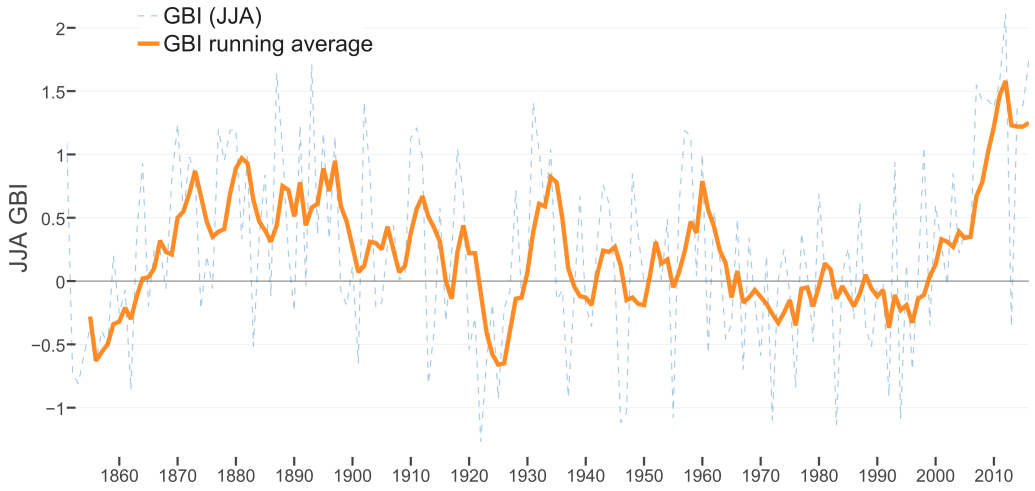

Figure 5.9: **Extended Greenland Blocking Index (GBI) (1850-2016, data from Hanna et al. (2016)).** Average JJA GBI from mean 500 hPa geopotential height between 60-80°N and 20-80°W (blue) and 5 year running average GBI (orange).

5.6 Discussion

Our results indicate that climate models which do not adequately capture NAO behavior will not reproduce the forcing required to simulate the current SMB trends observed over the last two decades, which confirms results of previous studies (Fettweis et al. 2013a; Tedesco et al. 2013; Hanna et al. 2014; Hanna et al. 2015). They also indicate that the sudden decline in Greenland's (surface) mass balance is not primarily a direct response to the local increase in atmospheric temperature, because anomalies in downwelling longwave radiation have

contributed less energy to the increase in melt of the GrIS than SWD anomalies. This is contradictory to previous analyses that have focused on the increase in temperature as the main cause of GrIS melting (Tedesco et al. 2013; Tedesco et al. 2016), as well as on the long-wave warming effect of clouds (Van Tricht et al. 2016). Climate warming is instead altering large-scale circulation patterns (Fettweis et al. 2013a; Norris et al. 2016; Hanna et al. 2014; Hanna et al. 2015) (Fig.5.7, Fig.5.8 and 5.9), which then causes an even larger response in the local energy budget of the GrIS by enhancing not only atmospheric temperature, but also solar insolation. Further, our results indicate that the recent decline in surface reflectivity is partly caused by SWD anomalies by enhancing the melt-albedo feedback and the spectrum of radiation reaching the surface (Box et al. 2012; Warren 1982)(Fig. 5.7).

In addition, we note that it is essential that simulations used for future projections capture both the seasonal and spatial pattern of cloud cover changes, if they are to provide useful forcing for modelling future GrIS mass trends. This will be challenging given the relatively coarse resolution of the current generation of GCMs and the difficulty in optimizing cloud properties for both low-mid latitude and polar climates. Our results present a paradigm shift for understanding the role of optically thick clouds on the SMB of the Greenland Ice Sheet.

Chapter 6

Cloud microphysics and circulation anomalies control differences in future Greenland melt

6.1 Preface

The previous chapter has explored the influence of clouds on the contemporary Greenland Ice Sheet melt increase over the last two decades. In this chapter we will discuss the role of clouds in future projections (until 2100) of the Greenland Ice Sheet surface mass balance and sea level contribution. We will especially focus on the role that cloud microphysical properties (ice vs. liquid cloud fraction) will play in the 21st century and we will quantify the uncertainties in these projections directly attributable to clouds. Additionally, we will also focus on how uncertainties due to cloud microphysics compare to uncertainties due to potentially missing anticyclonic circulation anomalies. We will also highlight the dynamic nature of the cloud radiative effect over Greenland, which also shows a transient response in a warming climate. Therefore, this research chapter will add additional insight into the importance of clouds for accurate future sea level rise predictions.

For large parts the following research chapter has been published in *Nature Climate Change* under the citation: **Hofer, S., Tedstone, A. J., Fettweis, X., & Bamber, J. L. (2019). Cloud microphysics and circulation anomalies control differences in future Greenland melt. Nature Climate Change, 9(7), 523.**

Overall, only very minor adjustments have been made to the published paper. Supplementary material has been added in-line and the Data and Methods chapter has been moved to the main part of the manuscript. The author contributions from this paper are as follows:

"*S.H. analysed the data and wrote the manuscript. S.H., J.B. and A.T. designed the study and methods. J.B. and A.T. supervised the project. X.F. developed and provided the daily climate model outputs as well as additional analyses. All authors discussed the results and commented on the manuscript.*"

6.2 Abstract

Recently, the Greenland Ice Sheet (GrIS) has become the main source of barystatic sea level rise (Van den Broeke et al. 2016; Van den Broeke et al. 2017). The increase in GrIS melt is linked to anticyclonic circulation anomalies, a reduction in cloud cover and enhanced warm air advection (Box et al. 2012; Hofer et al. 2017; Delhasse et al. 2018; Fettweis et al. 2017; Hanna et al. 2016). Despite CMIP5 GCMs not capturing recent circulation dynamics, regional climate models (RCMs) driven by these models still show significant uncertainties in future GrIS sea level contribution, even within one emission scenario (Delhasse et al. 2018; Taylor et al. 2012; Knutti et al. 2013; Hanna et al. 2018). Here, we use the RCM MAR to show that modelled cloud water phase is the main source of disagreement among future GrIS melt projections. We show that in the current climate, anticyclonic circulation results in more melting than under a neutral circulation regime. However, we show that the GrIS longwave cloud radiative effect is extremely sensitive to modelled cloud liquid water path, explaining melt anomalies of +378 Gt/yr (+1.04 mm/yr) in a +2 °C warmer climate with a neutral circulation regime, equivalent to 21% more melt than under anticyclonic circulation. The discrepancies between modelled cloud properties within the high-emission scenario (RCP8.5) introduce larger uncertainties in projected melt volumes than the difference in melt between low- and high emission scenarios (Church et al. 2013).

6.3 Introduction

Clouds are of first-order importance for the GrIS surface energy budget (SEB, Eq.6.1) as they can control shortwave (SW) and longwave (LW) fluxes (Bintanja et al. 1996; Warren 1982).

$$R = SW\downarrow \cdot (1-\alpha) + LW\downarrow - LWU \tag{6.1}$$

In the SW, clouds (i) block incoming solar radiation and (ii) change the albedo of the surface (Bintanja et al. 1996; Warren 1982). The amount of solar radiation reaching the surface for vertically homogenous liquid clouds depends on the cloud optical depth (COD, $\tau = (3LWP)/(2\rho_w r_e)$), which is a function of liquid water path (LWP), the effective particle radius (r_e) and the density of water (ρ_w). Variability in LWP controls the variability in COD. Clouds interact with the surface by filtering out parts of the near-infrared spectrum where

the ice albedo is low, thereby increasing the broadband surface albedo (Warren 1982).

In the LW, clouds contribute to the SEB by trapping heat, with a dependence upon cloud-phase (Shupe et al. 2004). Cloud mainly enhance the atmospheric emissivity ε in Eq.6.2.

$$LW \downarrow = \epsilon \cdot \sigma \cdot T^4 \tag{6.2}$$

While clouds tend to warm the highly reflective interior of the GrIS (Van Tricht et al. 2016), the secular trend in enhanced melt over the darker ablation zone has been partly controlled by a decrease in summer cloud cover and hence increased downwelling SW radiation (SWD) and SWnet (Hofer et al. 2017). These complex interactions show that appropriate representation of cloud microphysics is critical to reducing uncertainties in the projected GrIS sea level contribution (Van den Broeke et al. 2017; Hofer et al. 2017; Bintanja et al. 1996; Shupe et al. 2004; Bennartz et al. 2013; Bony et al. 2011; Tsay et al. 1989).

6.4 Regional climate models, sensitivity experiments and computation of melt potential

6.4.1 Modèle Atmosphérique Régional (MAR)

The regional climate model used in this study, MAR, is a hydrostatic atmospheric model that solves the primitive equation set. A detailed description of the model setup, physics and performance in regional climate simulations is given in Gallée et al. (1994), Fettweis (2007) and Fettweis et al. (2017). In this study we used the MAR version 3.7.0. The forcing fields from the CMIP5 model data (Taylor et al. (2012)) are prescribed at the model boundaries at a 6-hourly timestep for the period 1976-2100 for MIROC5 and NorESM1 and 1971-2100 for the CanESM2 forcing fields. These fields include information about temperature, wind, humidity and pressure at the surface. Within the model, the one-dimensional energy balance-based snow model SISVAT (Soil Ice Snow Vegetation Atmosphere Transfer) creates the link between the atmosphere, snowpack, the permanent ice on glaciers and the ice sheet, as well as the tundra surrounding the GrIS (De Ridder et al. 1998). The physical properties of snow and ice in SISVAT are directly based on the snow model CROCUS (De Ridder et al. 1998; Gallée et al. 2001). The model was run on an equal-area grid with a 25 km resolution. Over the GrIS the MAR has been extensively tested and its physics have been finely tuned to match in-situ and remote sensing data. Furthermore, it was also tested against other polar regional climate models (Fettweis 2007; Fettweis et al. 2017; Fettweis et al. 2011). It has especially been tuned to match the surface mass balance and melt extent on the GrIS (Fettweis 2007; Fettweis et al. 2011). The physical parameterisation of cloud microphysics in MAR was developed based on Meyers et al. (1992), with significant

improvements being implemented based on the work during the Mixed-Phase Arctic Cloud Experiment (Fridlind et al. 2007).

6.4.2 Sensitivity to anticyclonic circulation anomalies and cloud microphysics

ERA-Interim sensitivity experiments

To assess the impact of anticylonic circulation anomalies over Greenland as observed during the last two decades we split the ERA-Interim reanalysis product (Dee et al. 2011) into two parts following Delhasse et al. (2018). First, the JJA 1980-1999 period served as the reference period in which no circulation anomalies were observed and the GrIS was in equilibrium (Van den Broeke et al. 2009; Van den Broeke et al. 2016). Second, we used the JJA 2000-2016 period, when anticyclonic circulation anomalies were observed, to examine the impact of anticylonic conditions on melt and radiative fluxes relative to the neutral-circulation reference period. We note that the 2000-2016 period was 0.7°C warmer than the reference period, due to an inseparable combination of (i) circulation changes causing warm-air advection and (ii) global warming. In the next step, we artificially increased the ERA-Interim temperature at all of the 24 vertical sigma levels of MAR by +1, +1.5 and +2 °C. We preserved the relative humidity at the lateral boundaries by increasing the specific humidity. Sea surface conditions remained unchanged in the warmed ERA-Interim input fields. In Fig. 6.6 all the comparisons labelled "Circulation response" are differences between the 1980-1999 (neutral circulation) and the 2000-2016 period where anticylonic circulation anomalies were observed. Positive values correspond to higher melt or radiative fluxes during the anticyclonic period 2000-2016.

GCM sensitivity tests

We compared the response of GrIS radiation fluxes and melting caused by anticyclonic circulation anomalies (see ERA-Interim sensitivity experiments) to the response caused by diverging modelled cloud water phase in the GCM-forced MAR simulations at different warming levels.

First, for each of the MIROC5- and NorESM1-forced MAR simulations, we identified each 20-year period where the mean JJA temperature (at 850, 700, 600 and 500 hPa) over the whole integration domain reached +1, +1.5 and +2°C compared to the 1980-1999 reference period. Next we calculated the mean 20-year period of the two simulations for each warming level. We used these mean 20-year periods to compute the mean of the radiative fluxes and melt at +0 (1980-1999), +1, +1.5 and +2°C for each of the three GCM-forced simulations.

To identify the radiation and melt anomalies associated with cloud microphysics alone (i.e. without associated tropospheric warming), we compared the mean radiative and melt fluxes

of the MIROC5- and NorESM-forced simulations (low LWP enhancement, Fig.6.4a,c) with the CanESM2-forced simulation (∼3 x LWP enhancement compared to the other simulations, Fig.6.4b) at each warming level and period identified.

We note that CanESM2 exhibited slightly more JJA warming at each period/warming level than the other two simulations (Table 6.1, Table 6.2). During the whole period of study, CanESM2 projects approximately 1°C more warming over Greenland (Table 6.1, ΔT). However, CanESM2-forced JJA temperatures are in agreement with the other simulations during the 1980-1999 reference period and so we therefore conclude that the higher rate of warming through the CanESM-forced simulation is due to a positive feedback with the higher amount of liquid water content and greater downwelling longwave radiation, rather than a warm-bias inherent to the CanESM2 simulation.

	JJA (°C)			DJF (°C)			Annual (°C)		
	Nor1	Can2	M5	Nor1	Can2	M5	Nor1	Can2	M5
1980-2000	-7.10	-6.39	-6.29	-28.36	-30.81	-27.70	-19.20	-19.97	-18.61
2030-2050	-5.04	-3.31	-4.52	-26.20	-26.95	-26.26	-17.37	-16.67	-16.98
2080-2100	-1.97	-0.14	-1.04	-23.67	-23.18	-21.89	-14.59	-13.18	-13.06
ΔT	+5.13	+6.25	+5.25	+4.68	+7.63	+5.81	+4.61	+6.79	+5.55

Table 6.1: **Evolution of GrIS mean 2 m temperature during 21st century.**

	0°C	+1°C	+1.5°C	+2°C
MAR NorESM1	1980-1999	2005-2024	2017-2036	2031-2050
MAR CanESM2	1980-1999	1993-2012	1999-2018	2009-2028
MAR MIROC5	1980-1999	2009-2028	2019-2038	2030-2049

Table 6.2: 20 year period for specific warming levels of every MAR GCM simulation.

6.4.3 Computation of anomalies

Anomalies presented in this paper are calculated based on the 1980-1999 average of the model outputs (Melt, SMB, cloud properties, radiative properties etc.). Whenever radiation anomalies and non-radiative surface energy budget components are not shown in their SI-unit (joule) they have been converted to a mass anomaly ("melt potential") (Hofer et al. 2017). For this purpose, we use the heat of fusion which is needed to melt 1 kg of ice $H_f = 333.55\ kJ/kg$, where positive values correspond to an above average downward flux of energy or heat. A positive anomaly therefore means that more energy has been received at the surface at the GrIS than in the reference climate period. The radiative scheme in MAR is

the same that is used in the ERA-40 reanalysis product (Uppala et al. 2005). Radiative fluxes in the shortwave and longwave are broadband values, integrated over the whole range of the corresponding spectrum.
The three steps from model output on the 25 x 25 km grid to anomalies involve:

- Computing the monthly arithmetic mean of a given parameter from daily model outputs
- Computing the 1980-1999 climatological mean state of every pixel for every month
- Summing up the anomalies from the climatological mean and convert to melt potential (if applicable)

The following equation was used to compute the anomalies for every pixel and month

$$a_{i,j,month} = x_{i,j,month} - \overline{x_{i,j,m}} \tag{6.3}$$

where $a_{i,j,month}$ refers to the anomaly of a model pixel value ($x_{i,j,month}$) in the i^{th} rows and j^{th} column of the grid, from the corresponding monthly grid cell climatology. Subscript m refers to the month for which the equation was evaluated, i and j to the specific position on the model grid. We began with the radiative anomalies at each pixel in watts per meter squared. Because of the grid-cell extent of 25x25 km, we then multiplied this by the area of the pixel to arrive at the total anomaly in watts (joules per second) of one singular grid cell. We then summed up all the values spatially over the entire GrIS (see Eq. 6.4) and multiplied by the duration of the month (in seconds). This took us from joules per seconds to the total anomalies in joules, which we then converted to melt anomalies in gigatons.

$$\Delta a_{total} = \sum_{i} \sum_{j} a_{i,j,month} \tag{6.4}$$

CMIP5 and RCP pathways

The fifth phase of the Climate Model Intercomparison Project (CMIP5) is the most recently completed general circulation model (GCM) intercomparison project (Taylor et al. 2012). In total, around 20 climate modelling groups were a part of the CMIP5 project and altogether roughly 50 different climate models took part (Taylor et al. 2012). To produce higher resolution regional climate model output, the Coordinated Regional Downscaling Experiment (CORDEX) was built around the CMIP5 GCM model output (Taylor et al. 2012), with the MAR model outputs used in this being compliant with the CORDEX framework (Fettweis et al. 2017).

For CMIP5 models there have been four representative concentration pathways (RCP) formulated, but only two of them are part of the "core" experiments in the CMIP5 project (Taylor et al. 2012). The RCP values (e.g. RCP 8.5) refer to the approximate forcing due to GHG forcing in Wm^{-2} at the surface of the Earth, compared to preindustrial levels (Taylor et al. 2012). The RCP 8.5 pathway used in this study is a high emission scenario ("business as usual"), with the radiative forcing increasing throughout the 21st century (Taylor et al. 2012). Various other intercomparison projects have been built around CMIP5, with one specifically looking at feedbacks from clouds in the GCMs (Cloud Feedback Model Intercomparison Project - CFMIP, see Bony et al. (2011)). However, despite a significant increase in resolution and therefore more computational power being used by these models, and more physical processes being captured by the CMIP5 model block compared to previous CMIP models, the overall spatial and temporal patterns of main climate variables like temperature and precipitation have not changed significantly (Knutti et al. 2013). CMIP5 models have incorporated more physical processes than any other CMIP project before, making it the most physical based representation of climate change modelling to date (Taylor et al. 2012; Knutti et al. 2013).

6.5 Results

6.5.1 Partitioning of surface energy budget anomalies

To analyse the differences between RCP 8.5 GrIS melt projections, we forced the RCM MAR (Modèle Atmosphérique Régional (Fettweis et al. 2017)) with three different projections from the CMIP5 model suite (Fettweis et al. 2017; Fettweis et al. 2013b; Fettweis et al. 2011). We chose these GCMs because they most closely match the 700 hPa temperature and mid-tropospheric circulation over Greenland during 1980-1999 when compared to ERA-Interim reanalysis (Fettweis et al. 2013b). However, because the CMIP5 models do not predict the recent anticyclonic circulation regime over Greenland (Hofer et al. 2017; Delhasse et al. 2018; Hanna et al. 2018; Fettweis et al. 2013b), these results are only valid for a neutral circulation state.

There is a significant difference in total melt amount between the simulations (Fig.6.1). From 2017-2100 MAR forced by CanESM2 simulates 86,000 Gt of melt anomalies (23.7 cm sea level equivalent SLE (Planton 2013)) during summer (JJA), almost twice as much as MAR NorESM1 (46,400 Gt, 12.8 cm SLE) and MIROC5 (54,100 Gt 14.9 cm SLE). There is a factor of 1.85 between the smallest and largest melt projections, which is larger than the factor 1.75 difference between the projected GrIS contribution to barystatic global sea level rise by the end of the 21st century under RCP 2.6 versus RCP 8.5 (Church et al. 2013).

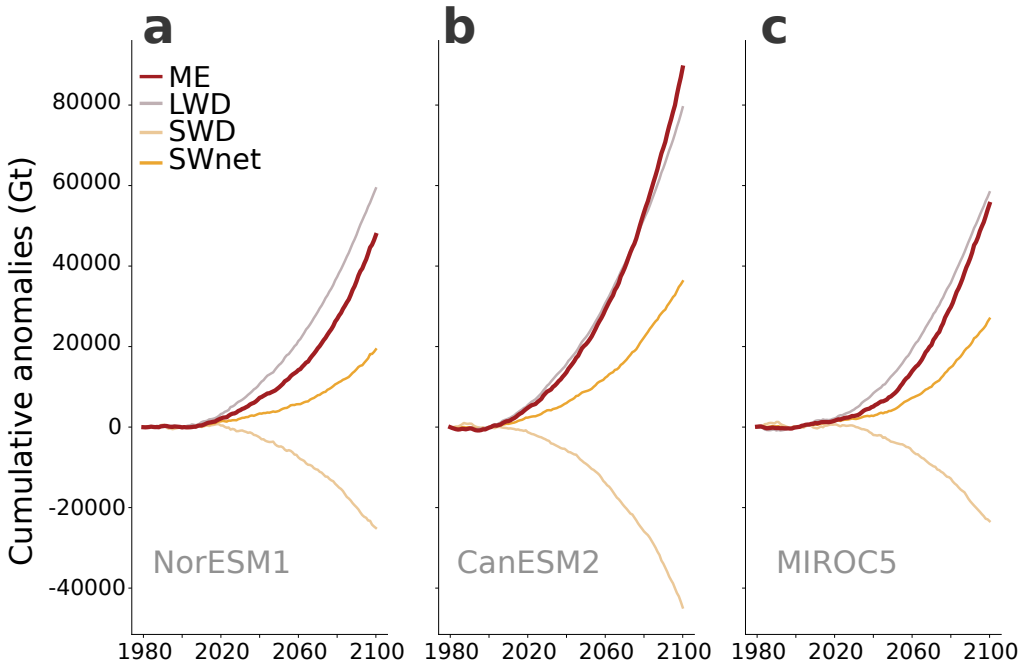

Figure 6.1: **Cumulative summer melt and radiation anomalies expressed as melt potential.** a) Cumulative anomalies based on the 1980-1999 mean state of the model expressed as melt anomalies (Gt) and radiation anomalies as melt potential (Gt), with MAR forced by NorESM1. 'ME' are the cumulative melt anomalies, 'SWD' and 'LWD' are shortwave downward and longwave downward anomalies, 'SWnet' are anomalies in the net shortwave radiation. b) Same as a), but with CanESM2 input. c) Same as a) but with MIROC5 input.

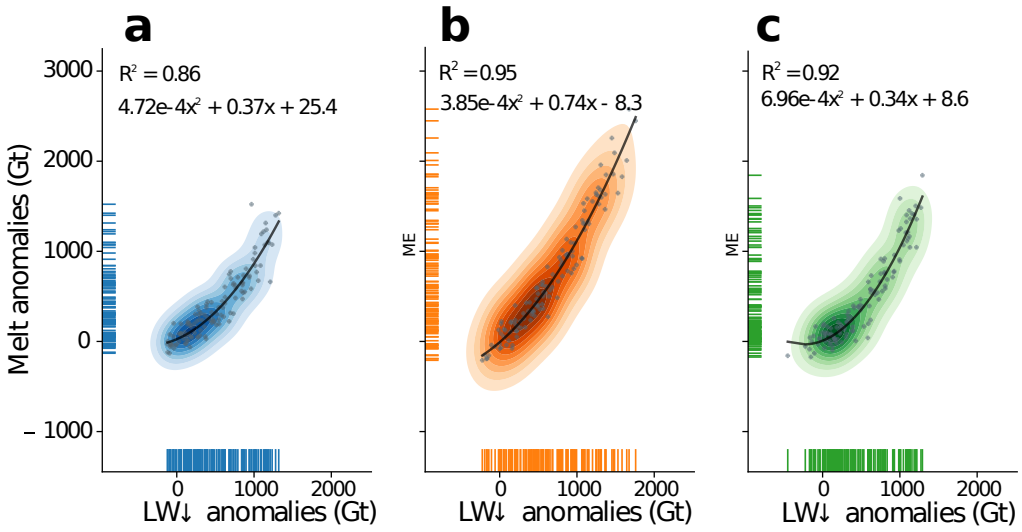

Figure 6.2: **Correlation between LWD and melt anomalies during summer.**. Panel a) shows the correlation between JJA LWD anomalies expressed as melt potential (Gt) and GrIS JJA melt anomalies (Gt) in MAR NorESM1. The dark grey line shows a second-order fit, with correlation coefficient and polynomial parameters given on the panel. b) same as a) but for MAR CanESM2. c) same as above but for MAR MIROC5.

The most significant energy flux contribution comes from JJA longwave downward (LWD) radiation anomalies, with a total of 79,400 Gt melt potential between 2017 and 2100 in CanESM2. Again, MAR NorESM1 and MIROC5 show significantly lower LWD anomalies, with 59,300 Gt and 58,300 Gt respectively. The significant positive correlation between melt and LWD anomalies explains between 86% and 95% of melt anomalies (Fig. 6.2). Conversely, SWD anomalies are negative across all simulations. This suggests that the shortwave transmissivity of the atmosphere will decrease in a warming climate with a neutral circulation over the GrIS (Franco et al. 2013). This combined change in LWD and SWD anomalies points towards a contribution of cloud microphysical properties.

Despite a decrease in SWD, SWnet anomalies are positive in all simulations because of the melt-albedo feedback (Box et al. 2012; Tedesco et al. 2016). CanESM2 also estimates the largest increase in SWnet at 36,200 Gt, versus 19,300 Gt (NorESM1) and 26,900 Gt (MIROC5). We find that SWD and SWnet anomalies are of second-order importance in future GrIS surface mass balance (SMB) projections compared to differences in LWD (on average, SWnet 2.4 x lower, SWD 2.1 x lower) (Franco et al. 2013). While the albedo scheme of MAR has been verified against in-situ observations and remote sensing data, the quantification of SWnet anomalies remain subject to uncertainties as RCMs lack important albedo feedbacks (Tedesco et al. 2016; Tedstone et al. 2017; Alexander et al. 2014; Cook et al. 2017).

Physically, there are two mechanisms that can explain the differences in LW fluxes: Differ-

ences (i) in the emissivity of the atmosphere (eq.6.5) and (ii) in air temperature. Because infrared cloud emissivity (ϵ) is linked to cloud microphysics and the COD (τ) via

$$\epsilon = 1 - \exp(-\beta\tau), \tag{6.5}$$

where β is a diffusivity factor (Curry et al. 1992), any increase in COD can also enhance the general LWD fluxes from the atmosphere by increasing the emissivity.

6.5.2 Evolution of cloud optical thickness

Figure 6.3 (first row) shows that CanESM2, with the highest projected melt and LWD anomalies also shows the largest increase in COD, 2.18 times greater than in NorESM1 and 2.06 times greater than in MIROC5 (1980-2100). The increase in all three simulations is correlated most closely with a quadratic increase of COD over time. MAR CanESM2 also predicts the largest increase in LWD anomalies, reaching 1165 Gt (NorESM1), 1622 Gt (CanESM2) and 1122 Gt (MIROC5, Fig.6.3, second row). All three simulations show a statistically significant positive correlation between COD and LWD ($R^2 = 0.98$, 0.99 and 0.99, Figure 6.3 last row). However, the increase in COD follows a parabolic function, while the anomalies in LWD show a more linear response, indicating a saturation effect.

Using the equation of the saturation curve (Fig. 6.3 last row), we find that for CanESM2 the impact of COD on LWD anomalies would cease at COD=1.46, 0.61 (NorESM1) and 0.57 (MIROC5). At this point the cloud emissivity reaches unity in a neutral future GrIS circulation state. Figure 6.3 (last row) also indicates a transient response of the LW CRE, with a decreasing sensitivity with increasing COD. However, in our simulations cloud cover does not change during the 21^{st} century and therefore increasing COD is the only mode of variability. Normally, the atmospheric emissivity only reaches unity when the cloud cover approaches 100%. Conversely, an increase in COD beyond the saturation values for LWD would still reduce SWD anomalies because this effect saturates more slowly (Shupe et al. 2004). These results also suggest that the LW CRE is currently highly sensitive to changes in cloud properties (i.e. steep slope at current COD).

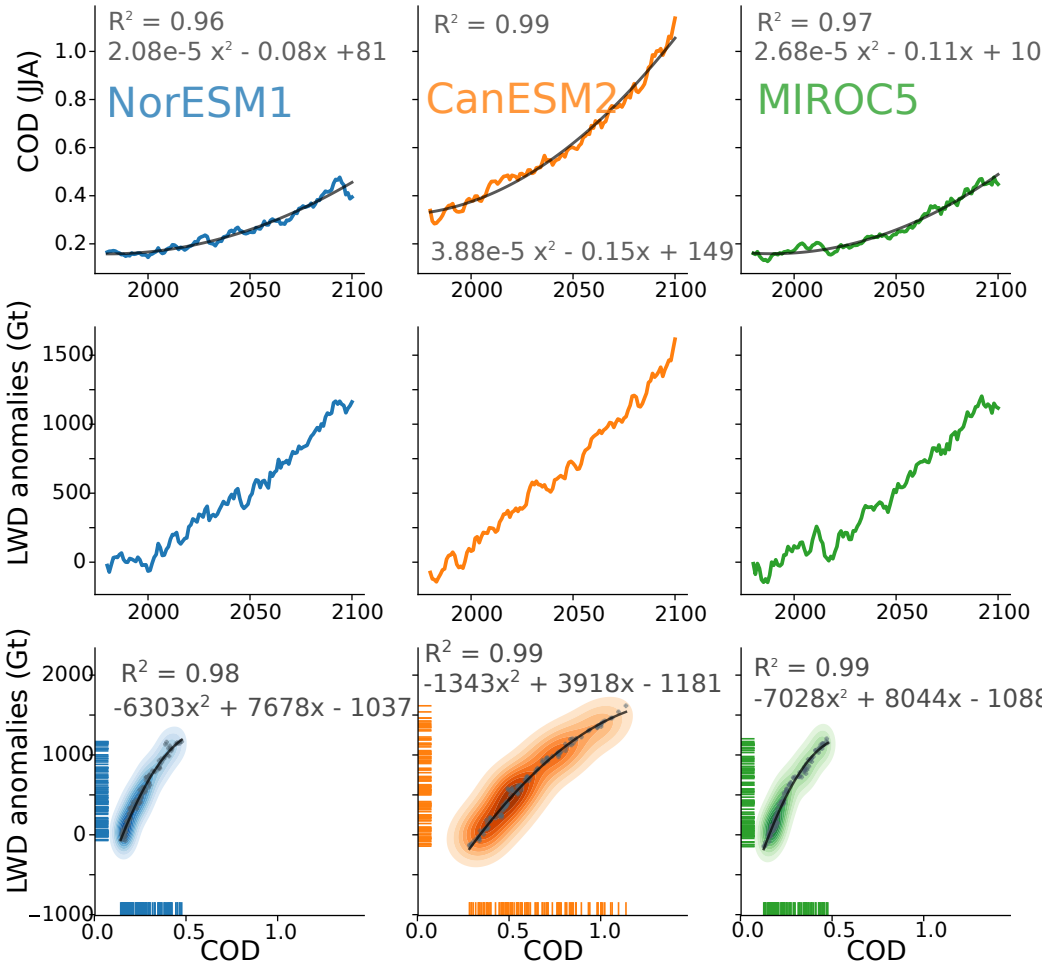

Figure 6.3: **Cloud optical depth, LW radiation anomalies and their connection.** The first row shows the five-year running mean of COD during JJA over the GrIS from the three different GCM inputs - NorESM1, CanESM2, MIROC5 from left to right (blue, orange and green respectively). The black line is a second-order polynomial fit, with corresponding fit parameters and R^2 values as plot labels ($p \ll 0.01$). The second row shows the five-year running mean of GrIS JJA LWD anomalies based on the 1980-1999 mean state of the model, expressed as melt potential (Gt). Last row shows the correlation between JJA COD and LWD anomalies, with a second-order polynomial fit to the data with coresponding fit parameters and R^2 values ($p \ll 0.01$).

6.5.3 Representation of cloud water phase

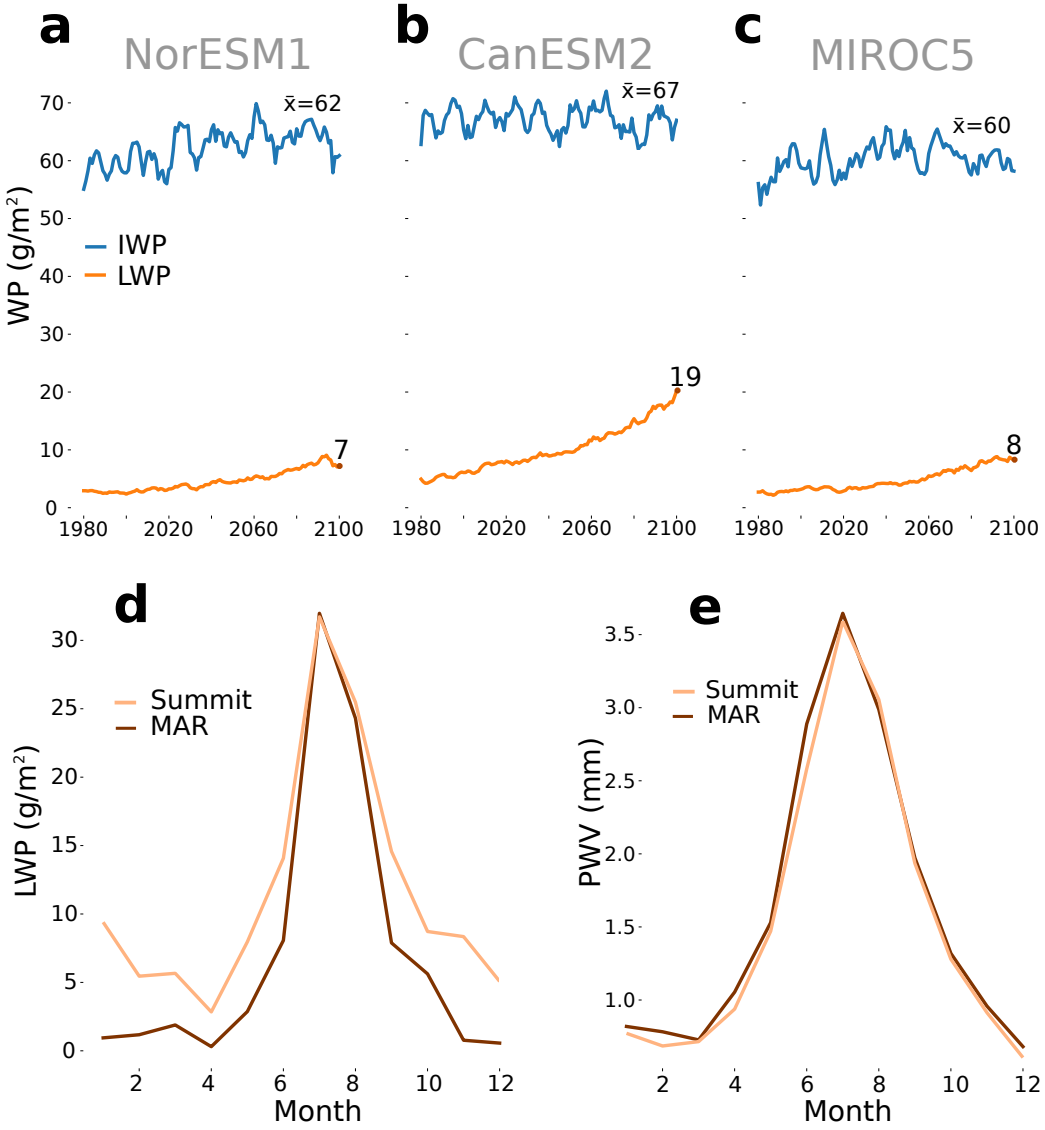

Figure 6.4: **Evolution of liquid and ice water path and comparison to in-situ and satellite observations.** The first row (a-c) shows the five-year rolling mean of JJA liquid water path (LWP) and ice water path (IWP) over Greenland. Panel d) shows a comparison of the annual LWP (g/m^2) cycle for Summit Camp, Greenland. We compare MAR LWP over Summit Camp (72°35'46.4"N 38°25'19.1"W) to in-situ observation from Summit between 2011-Jan and 2014-Jun when in-situ data are available (Miller et al. 2015; Miller et al. 2017). Panel e) shows the precipitable water vapour (mm) output from MAR over Summit and in-situ observations from Summit Camp.

The representation of atmospheric water content is very important in determining the SEB because the LW emissivity of clouds (Eq. 6.5) is dominated by variability in the LWP. Fig. 6.4a-c shows only small differences in total ice water path (IWP), with averages of 62, 67 and 60 g/m^2. However, there are significant differences in the LWP, with MAR CanESM2

estimating a 2.7 times greater LWP. The optically thicker clouds in the highest melt simulation are therefore due to a significantly larger amount of liquid water, rather than a homogenous increase in both IWP and LWP. This also highlights how COD and higher melt are connected: MAR CanESM2 produces clouds that bear more liquid water, which leads to optically thicker clouds via $\tau = (3LWP)/(2\rho_w r_e)$, which in turn makes the atmosphere more efficient at emitting LWD (c.f. Eq. 6.5).

The source of higher LWP and melt in the CanESM2-forced run may be associated with higher humidity as CanESM2 predicts an earlier ice-free Arctic Ocean than other CMIP5 models (Stroeve et al. 2012). GCMs in the Arctic are also highly sensitive to tropical teleconnections and differences in ocean forcing such as the Atlantic Multidecadal Oscillation (AMO) (Trenberth et al. 2014; Ding et al. 2014).

We are confident that the longwave emissivity is not influenced by changes in the overall JJA cloud cover. While the cloud cover shows significant decadal variability, there is no clear secular trend (Fig.6.5 A), likely because GCMs do not simulate future circulation changes (Hanna et al. 2018; Fettweis et al. 2013b; Delhasse et al. 2018).

Temperature only accounts for small proportions of LW and melt anomalies. At the start, MAR CanESM2, the model with 1.85 times more melt ranks in second place for melt season 2-m temperature while MIROC5 is the warmest (Table 6.1, Fig. 6.5 B, C). MAR CanESM2 also has the coldest annual temperature at the start. However, MAR CanESM2 becomes slightly warmer towards the end of the 21^{st} century when its JJA temperature is 0.9 °C and 1.8 °C elevated compared to MIROC5 and NorESM1. These differences in JJA temperatures are likely a consequence of and not a precursor for differences in modelled cloud microphysics. Approximating the atmosphere as a black body (Eq.6.2) (2080-2100), these temperature anomalies only explain 2.7% of the differences in LWD.

6.5.4 Comparison between uncertainties due to cloud microphysics and circulation

MAR is able to reproduce JJA cloud cover trends when compared to satellite data with increases in the North and decreases in the South of Greenland ((Hofer et al. 2017)). We also checked MAR's ability to reproduce observed cloud LWP and atmospheric water vapour content when forced with ERA-Interim (Miller et al. 2015; Miller et al. 2017; Dee et al. 2011). While MAR slightly underestimates the LWP between autumn and spring when compared to observations from Summit (Miller et al. 2015; Miller et al. 2017), it accurately captures the LWP evolution during the melt season. MAR also accurately models the precipitable water vapour distribution over Summit (Fig. 6.4e). MAR therefore captures the influence of cloud water phase distribution upon the SEB and future GrIS melt.

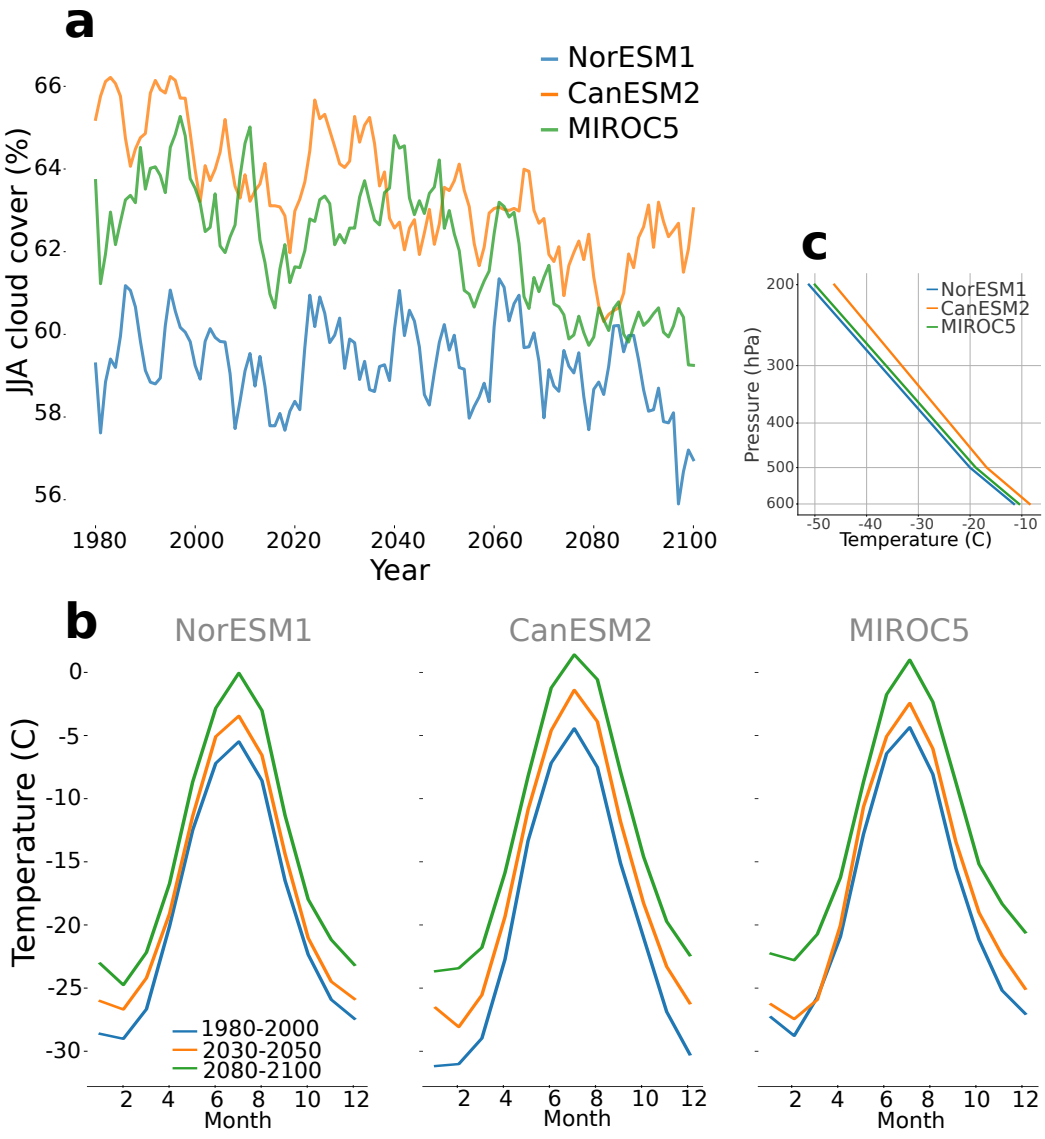

Figure 6.5: **Cloud cover and temperature evolution over Greenland.** Panel a) shows the five-year running mean of Greenland JJA cloud cover (liquid+ice) for all three simulations. b) shows the mean annual near-surface temperature cycles (monthly means) for three different periods and for all three MAR simulations over Greenland. c) shows the 600 hPa – 200 hPa 2070-2100 mean JJA temperature over Greenland.

Besides cloud microphysics, missing circulation anomalies in the GCMs are a second major source of uncertainties (Delhasse et al. 2018; Hanna et al. 2018). The recent melt increase over the GrIS is largely attributed to a switch of the NAO to an anticyclonic state (Hofer et al. 2017; Delhasse et al. 2018; Hanna et al. 2016; Hanna et al. 2018; Hanna et al. 2014; Fettweis et al. 2013a). These circulation anomalies have led to a decrease in cloud cover and to an increase in warm air advection mainly over southwest Greenland, increasing both LW and SW fluxes (Box et al. 2012; Hofer et al. 2017; Delhasse et al. 2018). However, the latest studies show that all the CMIP5 models used for future projections do not simulate these circulation anomalies (Hanna et al. 2016; Hanna et al. 2018). Delhasse et al. (Delhasse et al. 2018) have shown that future melt could double if anticyclonic circulation were to persist during the 21^{st} century.

To compare uncertainties resulting from potentially missing anticyclonic circulation anomalies with uncertainties due to cloud microphysics, we forced MAR with artificially warmed reanalysis data which capture the recent anticyclonic circulation anomalies because they are observationally constrained (Fettweis et al. 2017; Fettweis et al. 2013b; Fettweis et al. 2013a).

We examined the effect of anticyclonic circulation anomalies upon GrIS melt and the SEB anomalies at different warming levels (+0°C, +1°C, +1.5°C, +2°C with respect to 1980-1999), and compared them to differences due to modelled cloud microphysics in a neutral future Greenland circulation (Fig.6.6). We compare 1980-1999 to 2000-2016 when circulation anomalies were observed at four warming levels (see Methods). We note that the 2000-2016 period is 0.7°C warmer than the reference period, due to an inseparable combination of (i) circulation changes causing warm-air advection and (ii) global warming.

Furthermore, we compare one RCP 8.5 simulation that produces the most 21^{st} century melt (CanESM2) to the mean of the other two projections at the same warming levels to assess differences resulting from diverging cloud LWP (see Methods). Our results therefore show the melt signal resulting from cloud microphysics on top of the additional melt due to tropospheric warming.

At the present-day climate of +0°C, anticyclonic circulation anomalies are 4.7 times more efficient at enhancing melt than cloud LWP anomalies at +218 Gt/yr compared to +38 Gt/yr (Fig. 6.6a). This is principally because anticyclonic circulation can enhance both LWD fluxes (warm air/humidity advection) and SWD fluxes (cloud dissipation) (Hofer et al. 2017; Delhasse et al. 2018). Conversely, positive LWP anomalies can only enhance LWD, while SWD is being reduced due to a higher cloud optical thickness (Fig. 6.6 b,c).

The extra melt due to uncertainties in modelled cloud microphysics is more sensitive to increasing temperatures than melt due to anticyclonic circulation anomalies. At +2°C, the cloud liquid water response yields an increase in melt of +378 Gt/yr (+1.04 mm/yr sea level

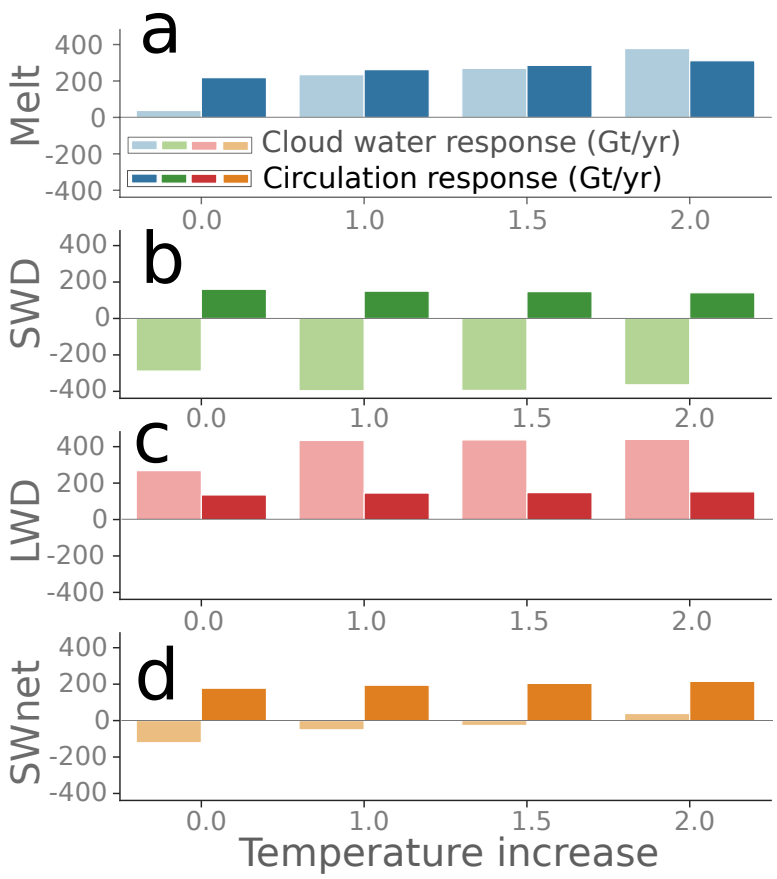

Figure 6.6: **Impact of anticyclonic circulation anomalies and cloud liquid water fraction anomalies upon melt and the surface energy budget.** a) Impact of circulation anomalies (dark blue) and liquid water path anomalies (pale blue) upon JJA melt and surface energy flux anomalies (Gt/yr) at different temperatures compared to 1980-1999 (+0, +1, +1.5 and +2 °C). Anomalies due to circulation changes are based on comparing the 1980-1999 mean of MAR forced by ERA-Interim with the 2000-2016 period where circulation anomalies have been observed. The cloud liquid water response is calculated based on comparing the mean of two MAR projections forced with GCMs without significantly enhanced cloud liquid water fraction (MIROC5 and NorESM1), with MAR CanESM2 which shows significantly enhanced cloud liquid water path. b) Impact of circulation and cloud liquid water fraction anomalies upon shortwave downward flux anomalies expressed as melt potential (Gt/yr). c) Same as b) but for longwave downward (LWD) anomalies. d) same as b) but for absorbed shortwave fluxes (SWnet).

equivalent SLE (Planton 2013)), a tenfold increase from the +38 Gt/yr at +0 °C. Melt due to anticyclonic circulation anomalies only increases by a factor of 1.4 compared to +0 °C, resulting in +311 Gt/yr (+0.86 mm/yr). While a LW dominated SEB could potentially lead to more melt over the bright accumulation zone and less melt over the darker ablation zone, we do not find any strong evidence for this: at +2 °C in the anticyclonic case 83% of total melt occurs in the ablation zone, compared to 82% in the neutral CanESM2 simulation. The main reason for the higher sensitivity of the neutral circulation case is a 1.6 times increase in LWD and an increase in SWnet (Fig. 6.6 d) from -121 Gt/yr to +39 Gt/yr due to the melt-albedo feedback, despite negative SWD anomalies (Fig. 6.6 b). However, SWD anomalies decrease more slowly than the rate of LWD increase, implying a different sensitivity of the LW and SW downwelling fluxes to cloud microphysics in a warming climate.

6.6 Discussion

Partitioning the SEB and comparing two distinctly different GrIS circulation scenarios enables us to show that major uncertainties in future GrIS sea level contribution arise from two different pathways. First, anticyclonic circulation anomalies can add additional +311 Gt/yr (+0.86 mm/yr SLE) in a +2 °C warmer climate in addition to the increase in melt by increased temperature alone, by increasing both shortwave fluxes (via reduced clouds in the South) and longwave fluxes (via enhanced temperature/humidity advection and more clouds in the North). However, it is unclear whether recent anticyclonic circulation anomalies will persist during the 21^{st} century. Second, in a more neutral Greenland circulation state, significant uncertainties arise from differences in modelled cloud microphysics and downwelling longwave fluxes, with the potential to contribute +378 Gt/yr (+1.04 mm/yr SLE) at +2 °C, in addition to the melt increase due to tropospheric warming. These melt anomalies are closely linked to the LW Cloud Radiative Effect (CRE), which is currently highly sensitive to an increase in COD. Our results indicate that uncertainties due to cloud processes depend on the specific circulation pathway and that the CRE shows a transient response in a warming climate (See discussion of the cloud radiative effect in section 6.6.1). In conclusion, our study highlights two key areas that should be addressed to significantly reduce GrIS melt uncertainties, (1) improvement of cloud microphysics and radiative schemes in climate models based on higher density of in-situ observations of cloud water phase, and (2) understanding the drivers of current GrIS circulation anomalies to assess the likelihood of them persisting in the future.

6.6.1 Discussion - Implications for GrIS cloud radiative effect

The analysis presented here has potential consequences on the topic of how much clouds influence current and future melt (Hofer et al. 2017; Van Tricht et al. 2016; Wang et al. 2018), specifically on how we discuss the GrIS cloud radiative effect (CRE).

First, in a neutral circulation state and corresponding climate the changes and uncertainties in the surface energy budget are mostly due to a "pure" cloud effect, with competing downwelling fluxes in the SW and LW part of the spectrum. Here, "pure" means that the response in the surface energy budget is controlled by changes in cloud cover or microphysics only. "Pure" cloud effects can only ever enhance one of the two fluxes while the other part is reduced, and therefore the exact value of the CRE is really important. However, our analysis combined with previous results (Fig.6.3 bottom and (Shupe et al. 2004)) show that the impact of clouds on the surface energy budget is far from constant over time in a changing climate. In the LW part, the GrIS is currently extremely sensitive to any increase in COD, however, the response flattens as the cloud LW emissivity ϵ reaches unity. Conversely, the reductions in the SW part are less sensitive to an increase in COD, leading to a transient CRE that is being dominated by downwelling LW fluxes. However, because in a warming climate the SW impact doesn't saturate as quickly as in the LW, with further warming the CRE influence could become SW dominated (again). It is therefore essential to consider, especially with rising temperature levels due to GHG emissions, that the GrIS CRE is not constant over time and is also showing a transient response. Any value attributed to it is only valid for the specific time period considered and not as a general constant.

Second, anticyclonic circulation anomalies over Greenland during the last 20 years have increased both shortwave and longwave fluxes, with SW fluxes being the dominant contribution over this period (Hofer et al. 2017). However, there are two potential mechanisms that could have led to this signal which need further investigation. First, increases in LW and SW fluxes over the same geographical areas could be due to a "mixed" response from decreases in cloud cover (more SW) and a higher frequency of warm air and moisture advection (more LW). In this case the exact quantification of the CRE might be of lower importance because it is theoretically possible to have positive SW and LW anomalies under cloud cover reductions in areas where clouds would usually warm the surface. Second, the positive SW and LW flux anomalies could be because recent studies ((Hofer et al. 2017)) have focused on a GrIS-wide aggregation of anomalies. This could mask the importance of the observed differences in cloud cover trends over geographically and climatologically separate areas of the GrIS, with increases in clouds over the cold and dry North and decreases in cloud cover over the South where clouds over the ablation zone have been found to cool the surface in summer (Wang et al. 2018; Wang et al. 2019). Therefore, we think that additional studies on the effect of clouds on the Greenland SEB and SMB (in hindcast simulations) should take a basin-scale approach when discussing recent trends in cloud characteristics.

Chapter 7

Discussion

7.1 Summary of Results

Validation of regional climate models

In Chapter 4 we explored the ability of regional climate models to reproduce observations of melt season changes in cloud cover, the radiative surface energy budget components and the atmospheric water vapour content. In hindcast mode, I found that two of the most commonly used regional climate models for the Greenland Ice Sheet – MAR and RACMO – can reproduce the recently observed reductions in summertime cloud cover. Furthermore, both regional climate models also show that over the last two decades, downwelling solar radiation has been the most significant contributor to changes in the surface energy budget, overlapping with an increase in anticyclone frequency over the Greenland Ice Sheet (Hanna et al. 2016; Hanna et al. 2018; Delhasse et al. 2018; Fettweis et al. 2013a).

Decreasing cloud cover drives the recent mass loss on the Greenland Ice Sheet

In Chapter 5 we explored the impact of recently observed circulation anomalies on the Greenland Ice Sheet surface energy budget and melt, discovering an unreported decrease in summer cloud cover and conclude that an increase in solar radiation has been the main driver of the recent mass loss on the Greenland Ice Sheet (Hofer et al. 2017). We show that MAR can accurately reproduce satellite observations of the decrease in summer cloud cover. Furthermore, in slight contrast to most of the recent literature, the temperature increase due to the Arctic amplification has contributed less in longwave energy than the decrease in summer cloud cover in the shortwave spectrum. Depending on the source of the anti-cyclonic circulation anomalies there are two potential mechanisms that explain the recent acceleration in GrIS mass loss; (1) Natural variability in the North Atlantic Oscillation or (2) An indirect link to global warming, e.g. a reduction in sea ice cover leads to circulation

anomalies which in turn lead to a decrease in clouds and an increase in mass loss via more solar radiation.

Cloud microphysics and circulation anomalies control differences in future Greenland Ice Sheet melt

In Chapter 6 we explored the main drivers behind differences in future Greenland Ice Sheet melt and sea level rise projections (Hofer et al. 2019). We forced the regional climate model MAR with three different GCMs from the CMIP5 project, chosen based on their performance against reanalysis data (ERA-Interim) (Hofer et al. 2019). Our findings indicate that differences in cloud microphysics can lead to a difference of a factor of two in Greenland sea level contribution (i.e. doubling surface melt) (Hofer et al. 2019). The difference between different melt projections due to cloud microphysics introduces larger uncertainties than between emission scenarios RCP2.6 and RCP 8.5 (Church et al. 2013; Hofer et al. 2019). Furthermore, we also find that the longwave cloud radiative effect is not constant over time in a warming climate, indicating a transient response (Hofer et al. 2019). The longwave cloud radiative effect is furthermore highly sensitive to any increase in cloud optical depth in the current climate, but this effect will saturate the more the Greenland climate warms, because the cloud emissivity approaches unity (Hofer et al. 2019).

7.2 Implications

Our results show that clouds are likely the most important atmospheric control of the Greenland Ice Sheet melt. In the current climate our results indicate that an increase in incoming solar radiation, due to a decrease in cloud cover, has contributed more energy to the Greenland Ice Sheet than the increase in downwelling longwave radiation due to global warming. In future projections, differences in cloud microphysics lead to similar or larger uncertainties than the uncertainty attached to the choice of our future greenhouse gas emissions and temperature increase. Additionally, we also find that the influence of cloud properties on the surface energy budget is highly sensitive to an increase in temperature in a warming world, indicating that it is highly important to consider the transient cloud radiative effect in context with its background climate. This thesis provides an addition to the growing literature on the effect of clouds on polar climates and will hopefully aid in creating additional and more in-depth studies of the sea level contribution of polar ice sheets and their connection to cloud properties.

7.2.1 Contemporary cloud radiative effect

The importance of the "cloud paradaxon" over the Greenland Ice Sheet, indicating that clouds warm the surface of the ice sheet, might be overstated or more complex than previously thought. Our results clearly show that the main external contributor to the increase in melt over the Greenland Ice Sheet has been an increase in downwelling shortwave radiation during June, July and August (Hofer et al. 2017). We also use an independent regional climate model RACMO, which also highlights the solar radiation anomalies during melt season as the main contributor to the surface energy budget. This increase in solar radiation reaching the surface has been driven by a reduction summer cloud cover, controlled by a highly anomalous state of the North Atlantic Oscillation leading to drier, warmer and sunnier summers. The increase in solar radiation mainly impacts the darker ablation zone, where the impacts of solar radiation are amplified by the low albedo and bare ice exposure during summer.

Our results are therefore contrary to the general statement that clouds warm the surface of Greenland all year, expressed for example in Van Tricht et al. (2016). However, in this study the authors use a model that has a too coarse spatial resolution to resolve the ablation zone (Van Tricht et al. 2016). Van Tricht et al. (2016) use a model with a grid spacing of 2° x 2°. This resolution converts to approximately 110 km (E-W) x 220 km (N-S) in the South of Greenland (60°N), 75 km x 220 km (70°N) and 40 km x 220 km (80°N). Because the ablation zone is only 100 km at its widest point in the southwest, but signficantly narrower in most other parts, this resolution does not resolve the ablation zone dynamics over the Greenland Ice Sheet.

Furthermore, Van Tricht et al. (2016) also upscale their annual CRE, which is dominated by the greenhouse effect during nine months of the year with little or no solar radiation, to the overall cloud impact upon GrIS melt which is confined to JJA.

> The annual mean CRE of 29.5W/m^2 provides enough energy to melt 90 Gt of ice in the GrIS ablation area during July and August (Van Tricht et al. 2016).

This study neglects the seasonal variability in solar radiation, the spatial differences in GrIS albedo during melt season, uses a model with a resolution that can't resolve the ablation zone (200 km x 110 km at 60° N) and bases it main conclusions on only three ablation years without any comparison to the long-term climatic mean.

Our research challenges the generally accepted consensus on the warming effect of clouds for two reasons: **(1)** Most of Greenland melt happens only during the three summer months June, July and August when the Arctic receives perpetual solar radiation. Using annual means of the cloud radiative effect as a proxy for clouds' impact upon melt season dynamics

is therefore highly questionable, because the annual mean cloud radiative effect is defined by their longwave effect during nine months of the year with little melt and almost no solar radiation.

(2) The effect of clouds during melt season in itself needs to be spatially separated into their effect on the dark ablation zone, where up to 80% of incoming solar radiation can be absorbed, against their impact on the highly reflective interior of the Greenland Ice Sheet, where only approximately 30% of all incoming solar radiation is usually absorbed. The warming ascribed to clouds over Greenland stems from their ability to act like a blanket, especially during 9 months of the year with little solar radiation, which is not representative of their impact during the short but intense Greenland melt season (Box et al. 2012; Fettweis et al. 2017). But more importantly, spatially aggregated means of the cloud radiative effect are also very likely not representative of the impact of clouds on the narrow ablation zone where most of the Greenland Ice Sheet melt occurs.

This spatial and temporal inhomogeneity in the Greenland cloud radiative effect has now been confirmed by Wang et al. (2018) and Wang et al. (2019) who find that clouds can cool the surface of the Greenland during summer over the ablation zone. Furthermore, these results have also been confirmed very recently by Ruan et al. (2019) and Niwano et al. (2019). Niwano et al. (2019) find, using regional climate model sensitivity tests, that under sunny conditions more melt occurs than under cloudy conditions. This higher total melt amount is mainly due to a greater absorption of solar radiation, in line with the results presented in Chapter 5 of this thesis. Additionally, Ruan et al. (2019) show, that since 2013, an increase in cloud cover over Greenland has led to an intermediate slowing of the GrIS melt increase, which is in line with our results that show that clouds can cool the surface over the dark ablation zone (Hofer et al. 2017). Overall, the most recent literature on the effect of clouds on the recent GrIS melt agrees with the presented results of this thesis.

7.2.2 Future projections

Connection between cloud microphysics and sea ice projections

Future projections are greatly impacted by cloud microphysics. Our results show that the cloud microphysical properties are equally important as the choice of greenhouse gas emission scenario for projecting Greenland's sea level contribution. Therefore, cloud microphysics are also as important as the increase in 21st century temperature. However, the cloud microphysical response in the forcing GCM fields and water vapour availability could be directly connected to sea ice projections in the Arctic, and not only be related to the cloud microphysics of models themselves.

In our model simulations, MAR forced by CanESM2 RCP8.5 future projections leads to almost double of the melt amount than MIROC5 and NorESM1 forcing. One of the most likely reasons for this is that CanESM2 is known to model the earliest ice-free Arctic Ocean during summer. In CanESM2, the sea ice might be gone as early as 2050, with one ensemble member even suggesting a first ice free Arctic summer in 2016 (Stroeve et al. 2012). The vast amount of open sea water in the CanESM2 forcing fields likely leads to the advection of airmasses into our regional climate model domain containing significantly more water vapour. Over our Greenland domain, this leads to the highest cloud optical thickness and the greatest melt amounts during the 21st century in the high-emission scenario.

However, thicker clouds might also be a precursor for the significantly earlier sea ice loss in CanESM2. We think that thicker clouds during spring in CanESM2 melt more bright sea ice, leading to an earlier ice-free Arctic and making more water vapour available. This presents a positive feedback loop in the GCM. While the thicker clouds in the highest melt simulation in our regional climate model might at first-order be due to faster sea ice loss in CanESM2, the sea-ice loss in itself might be due to a positive cloud feedback and a different cloud microphysics scheme in CanESM2 than in MIROC5 and NorESM1. Therefore, future analysis should focus on the representation of cloud microphysics in GCMs and their connection to the timing of an ice-free Arctic ocean in the 21st century.

Connection between circulation anomalies and cloud microphysics

Our results also indicate that the importance of the missing anticyclonic circulation anomalies in CMIP5 GCMs (Hanna et al. 2018) for GrIS melt highly depends on the future warming amount (Hofer et al. 2019). We show that in the current climate, anticyclonic circulation anomalies are more efficient in enhancing melt, directly contributing 218 Gt/yr of extra surface melt. However, cloud microphysical properties could potentially contribute 21% more melt (378 Gt/yr vs 311 Gt/yr) in a +2°C warmer climate (Hofer et al. 2019).

Conversely, so far it has not been tested if it would be theoretically possible that these two effects, anticyclonic circulation anomalies in future scenarios and cloud microphysics (i.e. thicker clouds), could also occur at the same time. Speculatively, there might be two different scenarios. Anticyclonic circulation anomalies mainly contribute to the surface energy budget by enhancing longwave radiation anomalies due to the advection of warm and moist airmasses towards the ice sheet, as well as by dissipating clouds, leading to enhanced solar radiation at the same time.

The first theoretical scenario is one in which optically thicker clouds in an anticyclonic future Greenland climate would counterbalance some of the increases in solar radiation, leading to a lower impact on the surface energy budget and subsequent melt. The second potential scenario could enhance surface melt, because optically thicker clouds would occur more

frequently in areas with warm-air advection upstream of an upper-air ridge, an area where longwave radiation anomalies have been shown to be more pronounced. Therefore, in this scenario, longwave radiation anomalies over these parts would be even further enhanced. Furthermore, downstream of the upper-atmospheric ridge where large-scale sinking motion prevails and prevents cloud formation, clouds occur a lot less frequent and therefore solar radiation potentially would be the main driver of the surface melt downstream of the upper level ridge. Therefore, through these spatially separate effects, this scenario would lead to more melt and an enhanced surface energy budget. In conclusion, future studies could design sensitivity experiments to test if it is possible that circulation anomalies and cloud microphysical anomalies could overlap and if they would dampen or amplify future Greenland Ice Sheet melt.

Longwave and shortwave cloud radiative effect in a warming climate

This thesis also highlights the sensitivity of the Greenland longwave cloud radiative effect to future warming, shifting the impact of clouds on the surface energy budget more towards a longwave warming of the surface (Hofer et al. 2019), with a strong sensitivity to rising temperatures. Therefore, the debate whether clouds increase or decrease Greenland melt will be highly dependent on our future emission pathway, because the longwave cloud radiative effect is extremely sensitive to any increase in temperature and cloud optical thickness (Hofer et al. 2019). Our results indicate that the longwave effect of clouds will soon be the main driver of the surface energy budget during summer in a warming climate.

Higher greenhouse gas emissions and temperature rise will very likely lead to a more longwave controlled surface energy budget, while effective mitigation scenarios would very likely also limit the shift towards a longwave warming dominated effect. While the longwave cloud radiative effect is currently very sensitive to any increase in cloud optical thickness and temperature, we also find that this effect will saturate during the 21st century (Hofer et al. 2019).

On the other hand, the shortwave effect of clouds does not saturate as quickly, because the albedo of clouds keeps increasing when clouds get thicker, even after their longwave emissivity reaches unity (Shupe et al. 2004; Hofer et al. 2019). One slight uncertainty in the treatment of the cloud radiative effect in future projections comes from the missing feedback of biological darkening over the two major ice sheets. With higher liquid water availability, more microbes will grow on the Greenland Ice Sheet, darkening the surface and leading to a higher fraction of absorbed shortwave radiation (Tedstone et al. 2017; Cook et al. 2017; Ryan et al. 2018) . However, this positive feedback loop is currently not parameterized in regional climate models, likely leading to an underestimation of the impact of absorbed shortwave radiation in future projections (Tedstone et al. 2017). Therefore, while our results

are clear that the external driver of the surface energy budget will become more longwave dominated, missing biological feedbacks on the ice sheet albedo might slightly shift this balance when considering the absorption of radiation at the surface.

7.2.3 Validation of regional climate models

The progression of Greenland Ice Sheet studies so far has mainly been to (1) partition the mass balance into surface mass balance and ice calving fluxes (Mouginot et al. 2019; Enderlin et al. 2014; Van den Broeke et al. 2016; Hanna et al. 2013) and to (2) partition the surface mass balance into its contributing factors (runoff, precipitation, sublimation) (Van den Broeke et al. 2009; Van den Broeke et al. 2016) and also to (3) partition the liquid water balance (Van den Broeke et al. 2016) (melt, rain, refreezing, retention, runoff). However, before this thesis, not many studies tried to identify the main energy budget components that drive the recent melt over the Greenland Ice Sheet, and even less literature exists for future projections (e.g. Franco et al. (2013)).

However, the question whether it is more important for models to reproduce changes in the surface energy budget, rather than the absolute values of the surface energy budget components has been largely unanswered. The main purpose of regional climate models over Greenland has been to accurately model the surface mass balance of the ice sheet. Therefore, a lot of emphasis has been put into developing models that accurately reproduce precipitation, melt and the surface albedo and atmospheric temperature patterns, because these are some of the variables that most directly influence the surface mass balance by enhancing or decreasing melt.

Importance of the representation of temporal trends

Our validation of two independent regional climate models (MARv3.9 and RACMO2p3) between 1979-2017 shows that both models simulate the recent surface mass balance and the contributing radiation anomalies (i.e. changes in the surface energy budget) very similarly. Conversely, when compared to daily atmospheric in-situ observations, MAR and RACMO disagree quite significantly on the absolute values of the radiative components of the energy budget. MAR for example underestimates the absolute values of the downwelling shortwave fluxes by about -12 W/m^2, while RACMO overestimates reflected (outgoing) shortwave radiation by about 5.5 W/m^2. Given that the radiative forcing from increasing greenhouse gas concentrations compared to pre-industrial levels is currently around 1.5 W/m^2 (Church et al. 2013), these biases in the radiative fluxes seem to be significant.

However, when looking at the changes in the surface energy budget over the last two

decades, both models show a very similar spatial response. Furthermore, they also both agree very well on the cumulative melt anomalies since the mid-1990s, which are largely driven by changes in the surface energy budget (Hofer et al. 2017). Therefore, the most likely explanation is that absolute biases in daily radiative energy fluxes in the regional climate models are very likely not as significant as their magnitude might suggest. Usually these models are tuned to match in-situ surface mass balance observations very accurately. Therefore, the user artificially creates a compensating bias in a different variable to counterbalance the lack or surplus of radiation in a different energy source or sink, in order to create a realistic melt response.

For the end user of the model outputs these tunings and compensating biases are often hard to track, as they can be manifested in a multitude of ways. These include changing the meltwater retention, albedo, precipitation efficiency of clouds or simply changing the amount radiation that reaches the surface in the radiative scheme. Nevertheless, given that both regional climate models are able to accurately reproduce changes in the surface energy budget and meltwater runoff from the Greenland Ice Sheet, there is a case to be made that it is potentially more important that regional climate models are able to reproduce the temporal trends, rather than the absolute values of the surface energy fluxes and melt.

Regional climate models in a transient climate

Regional climate models are rarely tested to model a transient climate response in the same way as General Circulation Models. In GCMs, one standard experiment is done by increasing the CO2 concentration until a doubling of carbon dioxide is reached. The increase in temperature at the time of CO_2 doubling is called the transient climate response and can be compared to the transient climate response of other models. However, similar tests in regional climate models are not done. One of the reasons for the lack of transient simulations is that a regional climate model is a dynamical downscaling toolbox, which heavily relies on the model forcing fields which are usually prescribed every 6 hours at the lateral boundaries (Rummukainen 2010).

Different regional climate models could potentially be validated for their transient climate response (or equilibrium climate sensitivity) when forced by a GCM simulation which incorporates a doubling of CO_2. However, this approach would be systematically different to the one used in General Circulation Models, because regional climate models are constrained by their lateral forcing fields and therefore are not able to simulate their own independent climate, especially over a spatially confined domain such as the Greenland Ice Sheet. However, it would enable the isolation of differences in the projected climate due to the RCM's model physics alone.

However, we are now seeing an increase in temperature over almost the entire planet and an

Arctic Amplification signal on top of the long-term temperature increase in high latitudes. Between 1880 and 2012, the Earth has warmed by +0.85°C, while temperatures in parts of the Arctic are now more than 2°C above pre-industrial levels (IPCC 2014). Therefore, it would be interesting to define standardised transient climate tests for polar regional climate models, rather than just a pure validation against daily meteorological observations in absolute terms. For example, one approach could be to define a common domain (e.g. Greenland) and use reanalysis data (e.g. Era-Interim (Dee et al. 2011)) and slowly increase the temperature of the lateral forcing fields. Therefore, one could evaluate the regional climate response to an increase of temperature (and humidity) at the boundaries.

A diametrically opposed approach would be to validate the regional climate models during a period where the Greenland Ice Sheet was stable (Fettweis et al. 2017; Van den Broeke et al. 2016), because today the Greenland Ice Sheet has already started to respond to an external forcing and therefore is showing a strong melting signal on top of the natural variability inherent to the Greenland climate system (Fettweis et al. 2017; Van den Broeke et al. 2016; Van den Broeke et al. 2017; Hofer et al. 2017; Delhasse et al. 2018). Potentially, it would therefore be more interesting to test if regional climate models are able to simulate this natural variability during periods without external climate forcing. However, there might be a feasibility problem, given that most of the Greenland Ice Sheet in-situ observations span a very short observational record, and most of the in-situ weather stations that record the surface energy budget fluxes have been installed since Greenland started to develop a strong melting signal (As et al. 2011). Subsequently, the strong melting signal observed over Greenland during the last two decades might hide some of the shortcomings of the ability of RCMs to reproduce fluctuations in SMB driven by natural climatic variability.

Complexity versus computational efficiency

This thesis also highlights another point of interest concerned with weighting the importance of computational efficiency versus more sophisticated climate model physics. In Chapter 4 (validation study) I use the regional climate model RACMO, where the cloud microphysical scheme is based on the ECMWF-IFS model's cloud microphysics scheme. The IFS microphysics scheme itself is a prognostic scheme for two variables, cloud cover and water mixing ratio, and therefore considered to be a two-moment scheme (Tiedtke 1993). On the other hand, the cloud microphysical scheme in MAR only uses prognostic equations for one variable, the water mixing ratio (solid, liquid and ice) and is therefore considered to be a slightly less sophisticated, yet very likely a more computationally efficient cloud scheme.

However, when looking at Greenland Ice Sheet wide anomalies of radiation, melt, surface mass balance and sea level contribution between 1979 and 2017, both models perform very similarly. This similarity raises the questions, whether more sophisticated microphysics are

really needed, or if the additional computational load of the two-moment scheme could be used more effectively elsewhere, e.g. for a higher spatial resolution in Greenland Ice Sheet regional climate simulations.

Given that the regional climate models are so frequently forced at the boundaries, in the usual case every 6 hours, do regional climate models even have enough "freedom" to produce their own climate, also related to cloud properties? Both models use atmospheric water vapour (specific humidity) at the boundaries as a lateral forcing field, which gets advected onto the domain by the also prescribed atmospheric circulation. Therefore, clouds most likely form due to the interaction of synoptic scale weather systems that are moving over the domain, with prognostic water vapour also prescribed at the lateral boundaries.

Potentially it might be better to use the computational power more efficiently to increase the spatial resolution of the models. Thereby, the models would theoretically be able to simulate a more realistic topography and synoptic-scale flow interaction, potentially also leading to an increased precision in precipitation and cloud patterns. However, these questions about how much complexity is needed in regional climate models, while still maintaining a scientific purpose and novelty, certainly go far beyond the topic of this thesis. However, it is likely that the future of Greenland Ice Sheet climate modelling at high resolutions will have to consider Greenland not as one entity but separate the impacts of changes in radiation and clouds on the surface mass balance at climatologically different sub-regions, for which a higher spatial resolution might prove advantageous.

7.3 Future research

The aim of this thesis was to create a new partitioning of the overall drivers of the Greenland Ice Sheet surface energy budget, melt and sea level rise contribution. We mainly focused on the contribution of clouds, because of their ability to significantly amend the radiative fluxes in the shortwave and longwave part of the spectrum. However, this research is far from completed and therefore this sub-section seeks to establish some ideas about the future direction of Greenland Ice Sheet clouds and surface energy budget research.

Our study highlights the spatially and temporally dynamic nature of the Greenland cloud radiative effect and therefore a spatially refined version of our approach might be needed in future research. While our partitioning of the surface energy budget presents a new step forward in Greenland climate research, our analysis heavily relies on Greenland Ice Sheet wide aggregated cumulative anomalies of surface energy budget, melt and the connection to changes in cloud properties. Therefore, one logical next step would be to define climatologically separate regions over Greenland and establish the influence of clouds for each distinct sub-region separately. For example, the south-eastern part of the Greenland Ice Sheet re-

ceives ample precipitation all year round and is relatively "warm". Conversely, the northern half of the Greenland Ice Sheet is very cold and dry when compared to the southeast, and therefore we assume that the cloud radiative effect and the ratio between water and ice content in the clouds might be significantly different. Therefore, a reduction in clouds, as observed over the last two decades, might have different impacts on different parts of the Greenland Ice Sheet, when analysed at the regional scale compared to the ice sheet scale.

Our research has established that the intra-annual variability of the cloud radiative effect is highly important, and that for melt season impacts of clouds over the Greenland Ice Sheet changes in cloud cover are almost exclusively relevant during June, July and August (i.e. summer). However, also with our temporal partitioning, further temporal refinements of the impact of clouds on the surface energy budget might lead to additional insights into the topic of how much changes in cloud cover have contributed to the recent- and will contribute to the future Greenland Ice Sheet melt.

Our regional climate model outputs have a daily timestep, therefore the large diurnal variability in shortwave and longwave radiation is not depicted in the model outputs. MAR has the capability to deliver hourly outputs for analysis, but this capability has only started to be utilised more recently. Therefore, hourly outputs were not available while undertaking the research in this thesis. It would certainly be interesting to test during which time of the day clouds cool/warm the surface the most, and during which time they could most efficiently enhance/decrease meltwater production and surface runoff.

This diurnal cycle analysis of the cloud-surface energy budget interaction might also highlight if melt peaks during the day, due to an increase in solar radiation, or the lack of refreezing of the ice surface during cloudy nights with longwave warming, might be more important for meltwater runoff. However, also in the diurnal cycle analysis, future research still needs to take into the account the spatial variability of the cloud radiative effect, because the diurnal peaks and throughs of melt and refreezing might behave very differently over bare ice (low albedo) than over snow or firn (high albedo). In conclusion, future research on the diurnal cycle of the clouds radiative effect and the different impacts of clouds during different times of the day will likely produce more insight into the Greenland Ice Sheet melt dynamics.

Additionally, it might be plausible that the interaction of the anomalous flow pattern over the Greenland Ice Sheet with the complex topography surrounding the ice sheet needs further research. The presented results suggest that the increased frequency of anticyclonic weather patterns over Greenland has led to cloud dissipation via large scale atmospheric subsidence. However, the flow pattern and the spatial distribution of cloud cover changes with increases in the north and decrease in the south of Greenland indicates that the Greenland topography might have a role to play too.

The presented results show that cloud cover during the melt season has increased over the north, where the altered flow patterns now favour onshore flow. This flow is likely lifted upwards and adiabatically cooled, resulting in the condensation of water vapour and subsequently a greater amount of clouds. Conversely, in the southern half of the Greenland Ice Sheet, the anticyclonic circulation pattern leads to anomalously strong downslope flow and katabatic winds. Therefore, the cloud cover reduction over the southern half of Greenland might not only be due to synoptic-scale subsidence, but also due to the increased downslope flow of air, resulting in adiabatic warming and subsequently drying of the airmasses and cloud dissipation.

However, currently it is not known which of the two proposed mechanisms, large-scale sinking motion or forced ascent and descent is more important for the observed spatial patterns of melt and cloud cover changes during the last two decades. Additionally, current regional climate models over Greenland use a spatial resolution between 7.5 km and 25 km. Therefore, many of the steep mountain-valley system surrounding the Greenland Ice Sheet are not accurately represented. We therefore think that testing the sensitivity of the interaction of flow and topography to increased model resolution might be an interesting research question resulting from this thesis. This proposed increase in accuracy of the representation of topography might also lead to further insight in the role that the Greenland Ice Sheet topography has had on the recent melt increase via its interaction with the observed anomalies in synoptic-scale circulation.

7.4 Concluding remarks

The research presented in this thesis (Chapters 4-6) has shown the profound impacts of clouds on the Greenland Ice Sheet climate system. This thesis also provides evidence for the importance of cloud microphysics and the representation of synoptic-scale circulation for accurate projections of the Greenland Ice Sheet sea level contribution during the 21st century. The results in this thesis additionally highlight the need for a denser network of in-situ cloud microphysical observation platforms to constrain the uncertainties in Greenland climate projections. Therefore, it is hoped that this thesis will provide a valuable perspective on clouds in the Arctic climate system and will therefore provide a guideline to improve our ability to model the impacts of global warming on future sea level rise.

Bibliography

Ackerman, A. S. et al. (2000). “Effects of aerosols on cloud albedo: Evaluation of Twomey’s parameterization of cloud susceptibility using measurements of ship tracks”. In: *Journal of the Atmospheric Sciences* 57.16, pp. 2684–2695.

Ackerman, S. A. et al. (1998). “Discriminating clear sky from clouds with MODIS”. In: *Journal of Geophysical Research: Atmospheres* 103.D24, pp. 32141–32157.

Agosta, C. et al. (2019). “Estimation of the Antarctic surface mass balance using the regional climate model MAR (1979-2015) and identification of dominant processes”. In: *The Cryosphere* 13.1, pp. 281–296.

Ahlstrøm, A. P. et al. (2009). “Monitoring the mass loss of the Greenland ice sheet”. In: *IOP Conference Series: Earth and Environmental Science*. Vol. 6. 1, p. 012003.

Alexander, P. M. et al. (2014). “Assessing spatio-temporal variability and trends in modelled and measured Greenland Ice Sheet albedo (2000–2013)”. In: *The Cryosphere* 8.6, pp. 2293–2312.

As, D. van and R. S. Fausto (2011). “Programme for Monitoring of the Greenland Ice Sheet (PROMICE): first temperature and ablation records”. In: *Geological Survey of Denmark and Greenland Bulletin* 23, pp. 73–76.

Bamber, J. et al. (2018). “Land ice freshwater budget of the Arctic and North Atlantic Oceans: 1. Data, methods, and results”. In: *Journal of Geophysical Research: Oceans* 123.3, pp. 1827–1837.

Bamber, J. et al. (2012). “Recent large increases in freshwater fluxes from Greenland into the North Atlantic”. In: *Geophysical Research Letters* 39.19.

Barnston, A. G. and R. E. Livezey (1987). “Classification, Seasonality and Persistence of Low-Frequency Atmospheric Circulation Patterns”. In: *Monthly Weather Review* 115.6, pp. 1083–1126. arXiv: 9605103 [cs].

Bennartz, R. et al. (2013). “July 2012 Greenland melt extent enhanced by low-level liquid clouds”. In: *Nature* 496.7443, pp. 83–86.

Bintanja, R. and M. R. Van Den Broeke (1996). “The influence of clouds on the radiation budget of ice and snow surfaces in Antarctica and Greenland in summer”. In: *International Journal of Climatology* 16.11, pp. 1281–1296.

Bony, S. et al. (2011). “CFMIP: Towards a better evaluation and understanding of clouds and cloud feedbacks in CMIP5 models”. In: *Clivar Exchanges* 16.56, pp. 20–24.

Box, J. E. et al. (2012). “Greenland ice sheet albedo feedback: thermodynamics and atmospheric drivers”. In: *The Cryosphere* 6.4, pp. 821–839.

Brun, E. et al. (1992). “A numerical model to simulate snow-cover stratigraphy for operational avalanche forecasting”. In: *Journal of Glaciology* 38.128, pp. 13–22.

Caesar, L. et al. (2018). “Observed fingerprint of a weakening Atlantic Ocean overturning circulation”. In: *Nature* 556.7700, pp. 191–196. arXiv: NIHMS150003.

Cesana, G. and T. Storelvmo (2017). “Improving climate projections by understanding how cloud phase affects radiation”. In: *Journal of Geophysical Research: Atmospheres* 122.8, pp. 4594–4599.

Church, J. et al. (2013). “Sea level change”. In: *Climate Change 2013: The Physical Science Basis. Contribution of Working Group I to the Fifth Assessment Report of the Intergovernmental Panel on Climate Change*, pp. 1137–1216.

Cook, J. M. et al. (2017). “Quantifying bioalbedo: a new physically based model and discussion of empirical methods for characterising biological influence on ice and snow albedo”. In: *The Cryosphere* 11.6, pp. 2611–2632.

Curry, J. A. and E. E. Ebert (1992). “Annual Cycle of Radiation Fluxes over the Arctic Ocean: Sensitivity to Cloud Optical Properties”. In: *Journal of Climate* 5.11, pp. 1267–1280.

Datt, P. (2011). “Latent Heat of Sublimation”. In: *Encyclopedia of Snow, Ice and Glaciers*. Ed. by V. P. Singh, P. Singh, and U. K. Haritashya. Dordrecht: Springer Netherlands, p. 703.

De Ridder, K. and H. Gallée (1998). “Land Surface–Induced Regional Climate Change in Southern Israel”. In: *Journal of Applied Meteorology* 37.11, pp. 1470–1485.

Dee, D. P. et al. (2011). “The ERA-Interim reanalysis: configuration and performance of the data assimilation system”. In: *Quarterly Journal of the Royal Meteorological Society* 137.656, pp. 553–597.

Delhasse, A. et al. (2018). “Brief communication: Impact of the recent atmospheric circulation change in summer on the future surface mass balance of the Greenland Ice Sheet”. In: *The Cryosphere* 12.11, pp. 3409–3418.

Dickinson, R. E. et al. (1989). “A regional climate model for the western United States”. In: *Climatic change* 15.3, pp. 383–422.

Ding, Q. et al. (2014). “Tropical forcing of the recent rapid Arctic warming in northeastern Canada and Greenland”. In: *Nature* 509.7499, p. 209.

Dumont, M. et al. (2014). “Contribution of light-absorbing impurities in snow to Greenland’s darkening since 2009”. In: *Nature Geoscience* 7.7, pp. 509–512.

Duynkerke, P. G. (1988). “Application of the E – e Turbulence Closure Model to the Neutral and Stable Atmospheric Boundary Layer”. In: *Journal of the Atmospheric Sciences* 45.5, pp. 865–880.

Dybbroe, A., K.-G. Karlsson, and A. Thoss (2005a). “NWCSAF AVHRR cloud detection and analysis using dynamic thresholds and radiative transfer modeling. Part 2: Tuning and Validation”. In: *Journal of Applied Meteorology* 44.1, pp. 55–71.

– (2005b). “NWCSAF AVHRR Cloud Detection and Analysis Using Dynamic Thresholds and Radiative Transfer Modeling. Part I: Algorithm Description”. In: *Journal of Applied Meteorology* 44.1, pp. 39–54.

Ebert, E. E. (2001). “Ability of a poor man’s ensemble to predict the probability and distribution of precipitation”. In: *Monthly Weather Review* 129.10, pp. 2461–2480.

ECMWF (2009). “Part IV: Physical Processes”. In: *IFS Documentation CY33R1*. IFS Documentation 4. ECMWF.

Enderlin, E. M. et al. (2014). “An improved mass budget for the Greenland ice sheet”. In: *Geophysical Research Letters* 41.3, pp. 866–872.

Ettema, J. (2010). “The present-day climate of Greenland A study with a regional climate model”. PhD thesis. Utrecht University.

Fausto, R. S. et al. (2016). “The implication of nonradiative energy fluxes dominating Greenland ice sheet exceptional ablation area surface melt in 2012”. In: *Geophysical Research Letters* 43.6, pp. 2649–2658.

Fettweis, X. (2007). “Reconstruction of the 1979-2006 Greenland ice sheet surface mass balance using the regional climate model MAR”. In: *The Cryosphere* 1.1, pp. 21–40.

– (2018). “SMB Model Intercomparison Project (SMBMIP) - First results”. In: *AGU Fall Meeting (Abstract)*, pp. 1–12.

Fettweis, X. et al. (2013a). “Brief communication: Important role of the mid-tropospheric atmospheric circulation in the recent surface melt increase over the Greenland ice sheet”. In: *The Cryosphere* 7.1, pp. 241–248.

Fettweis, X. et al. (2011). “Melting trends over the Greenland ice sheet (1958–2009) from spaceborne microwave data and regional climate models”. In: *The Cryosphere* 5, pp. 359–375.

Fettweis, X. et al. (2017). “Reconstructions of the 1900–2015 Greenland ice sheet surface mass balance using the regional climate MAR model”. In: *Cryosphere (The)* 11, pp. 1015–1033.

Fettweis, X. et al. (2013b). “Estimating the Greenland ice sheet surface mass balance contribution to future sea level rise using the regional atmospheric climate model MAR”. In: *Cryosphere* 7.2, pp. 469–489.

Franco, B., X. Fettweis, and M. Erpicum (2013). “Future projections of the Greenland ice sheet energy balance driving the surface melt”. In: *The Cryosphere* 7.1, pp. 1–18.

Frey, R. A. et al. (2008). “Cloud detection with MODIS. Part I: Improvements in the MODIS cloud mask for Collection 5”. In: *Journal of Atmospheric and Oceanic Technology* 25.7, pp. 1057–1072.

Fridlind, A. M. et al. (2007). “Ice properties of single-layer stratocumulus during the Mixed-Phase Arctic Cloud Experiment: 2. Model results”. In: *Journal of Geophysical Research Atmospheres* 112.24, pp. 1–25.

Gallée, H. (1995). “Simulation of the mesocyclonic activity in the Ross Sea, Antarctica”. In: *Monthly Weather Review* 123.7, pp. 2051–2069.

Gallée, H., G. Guyomarc'h, and E. Brun (2001). "Impact Of Snow Drift On The Antarctic Ice Sheet Surface Mass Balance: Possible Sensitivity To Snow-Surface Properties". In: *Boundary-Layer Meteorology* 99.1, pp. 1–19.

Gallée, H. and G. Schayes (1994). "Development of a Three-Dimensional Meso-γ Primitive Equation Model: Katabatic Winds Simulation in the Area of Terra Nova Bay, Antarctica". In: *Monthly Weather Review* 122.4, pp. 671–685.

Gallée, H. et al. (2014). "Simulations of blowing snow over Antarctica". In: *International Snow Science Workshop (ISSW)*, p. 120–p. 125.

Giorgi, F. and G. T. Bates (1989). "The Climatological Skill of a Regional Model over Complex Terrain". In: *Monthly Weather Review* 117.11, pp. 2325–2347.

Goelzer, H. et al. (2018). "Design and results of the ice sheet model initialisation initMIP-Greenland: An ISMIP6 intercomparison". In: *The Cryosphere* 12.4, pp. 1433–1460.

Goosse, H. et al. (2018). "Quantifying climate feedbacks in polar regions". In: *Nature communications* 9.1, p. 1919.

Hahn, L., C. C. Ummenhofer, and Y. O. Kwon (2018). "North Atlantic Natural Variability Modulates Emergence of Widespread Greenland Melt in a Warming Climate". In: *Geophysical Research Letters* 45.17, pp. 9171–9178.

Hanna, E., X. Fettweis, and R. J. Hall (2018). "Brief communication: Recent changes in summer Greenland blocking captured by none of the CMIP5 models". In: *The Cryosphere* 12.10, pp. 3287–3292.

Hanna, E. et al. (2008). "Increased runoff from melt from the Greenland Ice Sheet: a response to global warming". In: *Journal of Climate* 21.2, pp. 331–341.

Hanna, E. et al. (2012). "Recent warming in Greenland in a long-term instrumental (1881–2012) climatic context: I. Evaluation of surface air temperature records". In: *Environmental Research Letters* 7.4, p. 045404.

Hanna, E. et al. (2013). "Ice-sheet mass balance and climate change." In: *Nature* 498.7452, pp. 51–9.

Hanna, E. et al. (2014). "Atmospheric and oceanic climate forcing of the exceptional Greenland ice sheet surface melt in summer 2012". In: *International Journal of Climatology* 34.4, pp. 1022–1037.

Hanna, E. et al. (2015). "Recent seasonal asymmetric changes in the NAO (a marked summer decline and increased winter variability) and associated changes in the AO and Greenland Blocking Index". In: *International Journal of Climatology* 35.9, pp. 2540–2554.

Hanna, E. et al. (2016). "Greenland Blocking Index 1851 – 2015 : a regional climate change signal". In: *International Journal of Climatology* 4861.May, pp. 4847–4861.

Hines, K. M. and D. H. Bromwich (2008). "Development and testing of Polar Weather Research and Forecasting (WRF) model. Part I: Greenland ice sheet meteorology". In: *Monthly Weather Review* 136.6, pp. 1971–1989.

Hofer, S. et al. (2017). "Decreasing cloud cover drives the recent mass loss on the Greenland Ice Sheet". In: *Science Advances* 3.6, e1700584.

– (2019). “Cloud microphysics and circulation anomalies control differences in future Greenland melt”. In: *Nature Climate Change* 9.7, pp. 523–528.

Holz, R. E. et al. (2009). “Global Moderate Resolution Imaging Spectroradiometer (MODIS) cloud detection and height evaluation using CALIOP”. In: *Journal of Geophysical Research Atmospheres* 114.8, pp. 1–17.

Howat, I. M., I. Joughin, and T. A. Scambos (2007). “Rapid changes in ice discharge from Greenland outlet glaciers”. In: *Science* 315.5818, pp. 1559–1561.

Hubanks, P. et al. (2008). *MODIS Atmosphere L3 Gridded Product Algorithm Theoretical Basis Document*. Tech. rep., pp. 1–88.

IPCC (2014). “Climate Change 2014 Synthesis Report Summary Chapter for Policymakers”. In: *IPCC*, p. 31. arXiv: `arXiv:1011.1669v3`.

Karlsson, K.-G. et al. (2013). “CLARA-A1: a cloud, albedo, and radiation dataset from 28 yr of global AVHRR data”. In: *Atmospheric Chemistry and Physics* 13.10, pp. 5351–5367.

Karlsson, K.-G. et al. (2017). “CLARA-A2: the second edition of the CM SAF cloud and radiation data record from 34 years of global AVHRR data”. In: *Atmospheric Chemistry and Physics* 17.9, pp. 5809–5828.

Karlsson, K.-G. et al. (2016). *Algorithm Theoretical Basis Document - CM SAF Cloud, Albedo, Radiation data record, AVHRR-based, Edition 2 (CLARA-A2)*. Tech. rep., pp. 1–19.

Karlsson, K. (2014). *CM SAF cloud, albedo, radiation dataset, AVHRR-based, Edition 1 (CLARA-A1), Cloud products validation report*. Tech. rep. SAF/CM/SMHI/VAL/Gac/CLD.

Kay, J. E. et al. (2008). “The contribution of cloud and radiation anomalies to the 2007 Arctic sea ice extent minimum”. In: *Geophysical Research Letters* 35.8, pp. 1–5.

Kessler, E. (1995). “On the continuity and distribution of water substance in atmospheric circulations”. In: *Atmospheric Research* 38.1-4, pp. 109–145.

King, M. D. et al. (2013). “Spatial and temporal distribution of clouds observed by MODIS onboard the Terra and Aqua satellites”. In: *IEEE Transactions on Geoscience and remote sensing* 51.7, pp. 3826–3852.

Kittel, C. et al. (2018). “Sensitivity of the current Antarctic surface mass balance to sea surface conditions using MAR”. In: *The Cryosphere* 12.12, pp. 3827–3839.

Knutti, R. and J. Sedláček (2013). “Robustness and uncertainties in the new CMIP5 climate model projections”. In: *Nature Climate Change* 3.4, pp. 369–373.

Lang, C., X. Fettweis, and M. Erpicum (2015). “Stable climate and surface mass balance in Svalbard over 1979-2013 despite the Arctic warming”. In: *The Cryosphere* 9.1, pp. 83–101.

Laprise, R. (2008). “Regional climate modelling”. In: *Journal of Computational Physics* 227.7, pp. 3641–3666.

Leduc, M. and R. Laprise (2009). “Regional climate model sensitivity to domain size”. In: *Climate Dynamics* 32.6, pp. 833–854.

Lee, H. and J.-J. Baik (2018). “A Comparative Study of Bin and Bulk Cloud Microphysics Schemes in Simulating a Heavy Precipitation Case”. In: *Atmosphere* 9.12, p. 475.

Levkov, L. et al. (1992). “3D mesoscale numerical studies of cirrus and stratus clouds by their time and space evolution”. In: *Contributions to atmospheric physics* 65.1, pp. 35–58.

Lin, Y.-L., R. D. Farley, and H. D. Orville (1983). “Bulk parameterization of snow dield in a cloud model”. In: *American Meteorological Society* 22, pp. 1065–1092.

Machguth, H. et al. (2016). “Greenland surface mass-balance observations from the ice-sheet ablation area and local glaciers”. In: *Journal of Glaciology* 62.235, pp. 861–887.

Madec, G. et al. (2015). *NEMO ocean engine*. Tech. rep.

Marbaix, P. et al. (2003). “Lateral boundary conditions in regional climate models: a detailed study of the relaxation procedure”. In: *Monthly weather review* 131.3, pp. 461–479.

Mattingly, K., T. Mote, and X. Fettweis (2018). “Atmospheric river impacts on Greenland Ice Sheet surface mass balance”. In: *Journal of Geophysical Research: Atmospheres* 123.16, pp. 8538–8560.

Meijgaard, E. van et al. (2008). “The KNMI regional atmospheric climate model RACMO version 2.1”. In: *Technical report; TR - 302*, p. 43.

Meyers, M. P., P. J. DeMott, and W. R. Cotton (1992). “New Primary Ice-Nucleation Parameterizations in an Explicit Cloud Model”. In: *Journal of Applied Meteorology* 31.7, pp. 708–721.

Milbrandt, J. and H. Morrison (2015). “The Representation of Cloud Microphysical Processes in NWP Models”. In: *ECMWF - Annual seminar*.

Miller, N. B. et al. (2015). “Cloud Radiative Forcing at Summit, Greenland”. In: *Journal of Climate* 28.15, pp. 6267–6280.

Miller, N. B. et al. (2017). “Surface energy budget responses to radiative forcing at Summit, Greenland”. In: *The Cryosphere* 11.1, pp. 497–516.

Morcrette, J.-J. (2002). “The surface downward longwave radiation in the ECMWF forecast system”. In: *Journal of climate* 15.14, pp. 1875–1892.

Morlighem, M. et al. (2017). “BedMachine v3: Complete bed topography and ocean bathymetry mapping of Greenland from multibeam echo sounding combined with mass conservation”. In: *Geophysical Research Letters* 44.21, pp. 11–051.

Morrison, H., J. A. Curry, and V. I. Khvorostyanov (2005a). “A New Double-Moment Microphysics Parameterization for Application in Cloud and Climate Models. Part I: Description”. In: *Journal of the Atmospheric Sciences* 62.6, pp. 1665–1677.

Morrison, H. and J. Pinto (2005b). “Mesoscale modeling of springtime Arctic mixed-phase stratiform clouds using a new two-moment bulk microphysics scheme”. In: *Journal of the atmospheric sciences* 62.10, pp. 3683–3704.

Morrison, H. et al. (2011). “Intercomparison of cloud model simulations of Arctic mixed-phase boundary layer clouds observed during SHEBA/FIRE-ACE”. In: *Journal of Advances in Modeling Earth Systems* 3.2.

Morrison, H., G. Thompson, and V. Tatarskii (2009). “Impact of cloud microphysics on the development of trailing stratiform precipitation in a simulated squall line: Comparison of one-and two-moment schemes”. In: *Monthly weather review* 137.3, pp. 991–1007.

Mottram, R. et al. (2017). “Surface mass balance of the Greenland ice sheet in the regional climate model HIRHAM5: Present state and future prospects”. In: *Low Temperature Science* 75.March, pp. 105–115.

Mouginot, J. et al. (2019). “Forty-six years of Greenland Ice Sheet mass balance from 1972 to 2018”. In: *Proceedings of the National Academy of Sciences* 116.19, pp. 9239–9244.

Nghiem, S. et al. (2012). “The extreme melt across the Greenland ice sheet in 2012”. In: *Geophysical Research Letters* 39.20.

Niwano, M., A. Hashimoto, and T. Aoki (2019). “Cloud-driven modulations of Greenland ice sheet surface melt”. In: *Scientific Reports* 9.1, p. 10380.

Noël, B. et al. (2016). “A daily, 1 km resolution data set of downscaled Greenland ice sheet surface mass balance (1958-2015)”. In: *The Cryosphere* 10.5, pp. 2361–2377.

Noël, B. et al. (2018). “Modelling the climate and surface mass balance of polar ice sheets using RACMO2 – Part 1: Greenland (1958–2016)”. In: *The Cryosphere* 12.3, pp. 811–831.

Norris, J. R. et al. (2016). “Evidence for climate change in the satellite cloud record”. In: *Nature* 536.7614, pp. 72–75.

Perovich, D. K. (2018). “Sunlight, clouds, sea ice, albedo, and the radiative budget: The umbrella versus the blanket”. In: *Cryosphere* 12.6, pp. 2159–2165.

Planton, S. (2013). “Annex III: Glossary, In: Climate Change 2013: The Physical Science Basis. Contribution of Working Group I to the Fifth Assessment Report of the Intergovernmental Panel on Climate Change”. In: *Climate Change 2013: The Physical Science Basis. Contribution of Working Group I to the Fifth Assessment Report of the Intergovernmental Panel on Climate Change*, pp. 1447–1466.

Platnick, S. et al. (2015). *MODIS Atmosphere L3 Monthly Product*.

PROMICE (2019). *Programme for Monitoring of the Greenland Ice Sheet*. URL: `https://www.promice.dk/CurrentWeatherMap.html` (visited on 09/06/2019).

Rahmstorf, S. et al. (2015). “Exceptional twentieth-century slowdown in Atlantic Ocean overturning circulation”. In: *Nature Climate Change* 5.5, pp. 475–480.

Ramanathan, V. et al. (1989). “Cloud-Radiative Forcing and Climate: Results from the Earth Radiation Budget Experiment”. In: *Science* 243.4887, pp. 57–63.

Rignot, E. et al. (2008). “Mass balance of the Greenland ice sheet from 1958 to 2007”. In: *Geophysical Research Letters* 35.20, p. L20502.

Rignot, E. et al. (2011). “Acceleration of the contribution of the Greenland and Antarctic ice sheets to sea level rise”. In: *Geophysical Research Letters* 38.5.

Rogers, J. C. (1997). “North Atlantic storm track variability and its association to the North Atlantic oscillation and climate variability of Northern Europe”. In: *Journal of Climate* 10.7, pp. 1635–1647.

Ruan, R. et al. (2019). “Decelerated Greenland Ice Sheet melt driven by positive summer North Atlantic Oscillation”. In: *Journal of Geophysical Research: Atmospheres* 124, pp. 7633–7646.

Rummukainen, M. (2010). “State-of-the-art with regional climate models”. In: *Clim Change* 1, pp. 82–96.

Ryan, J. et al. (2017). “How robust are in situ observations for validating satellite-derived albedo over the dark zone of the Greenland Ice Sheet?” In: *Geophysical Research Letters* 44.12, pp. 6218–6225.

Ryan, J. et al. (2018). “Dark zone of the Greenland Ice Sheet controlled by distributed biologically-active impurities”. In: *Nature Communications* 9.1, pp. 1–10.

Schmidt, R. A. (1982). “Properties of blowing snow”. In: *Reviews of Geophysics* 20.1, p. 39.

Screen, J. A. et al. (2013). “The Atmospheric Response to Three Decades of Observed Arctic Sea Ice Loss”. In: *Journal of Climate* 26.4, pp. 1230–1248.

Screen, J. A. and I. Simmonds (2010). “The central role of diminishing sea ice in recent Arctic temperature amplification”. In: *Nature* 464.7293, pp. 1334–1337.

Shupe, M. D. and J. M. Intrieri (2004). “Cloud Radiative Forcing of the Arctic Surface: The Influence of Cloud Properties, Surface Albedo, and Solar Zenith Angle”. In: *Journal of Climate* 17.3, pp. 616–628.

Shupe, M. D. et al. (2013). “High and dry: New observations of tropospheric and cloud properties above the Greenland Ice Sheet”. In: *Bulletin of the American Meteorological Society* 94.2, pp. 169–186.

Skamarock, W. C. et al. (2008). *2005: A Description of the Advanced Research WRF Version 3*. Tech. rep.

Stevens, B. and G. Feingold (2009). *Untangling aerosol effects on clouds and precipitation in a buffered system*.

Storch, H. von, H. Langenberg, and F. Feser (2000). “A spectral nudging technique for dynamical downscaling purposes”. In: *Monthly weather review* 128.10, pp. 3664–3673.

Storelvmo, T. (2017). “Aerosol Effects on Climate via Mixed-Phase and Ice Clouds”. In: *Annual Review of Earth and Planetary Sciences* 45.1, pp. 199–222.

Stroeve, J. C. et al. (2012). “Trends in Arctic sea ice extent from CMIP5, CMIP3 and observations”. In: *Geophysical Research Letters* 39.16.

Tan, I. and T. Storelvmo (2019). “Evidence of Strong Contributions From Mixed-Phase Clouds to Arctic Climate Change”. In: *Geophysical Research Letters* 46.5, pp. 2894–2902.

Tan, I., T. Storelvmo, and M. D. Zelinka (2016). “Observational constraints on mixed-phase clouds imply higher climate sensitivity”. In: *Science* 352.6282, pp. 224–227. arXiv: 9809069v1 [arXiv:gr-qc].

Taylor, K. E., R. J. Stouffer, and G. A. Meehl (2012). “An Overview of CMIP5 and the Experiment Design”. In: *Bulletin of the American Meteorological Society* 93.4, pp. 485–498. arXiv: arXiv:1011.1669v3.

Tedesco, M. et al. (2013). “Evidence and analysis of 2012 Greenland records from spaceborne observations, a regional climate model and reanalysis data”. In: *The Cryosphere* 7.2, pp. 615–630.

Tedesco, M. et al. (2011). “The role of albedo and accumulation in the 2010 melting record in Greenland”. In: *Environmental Research Letters* 6.1, p. 014005.

Tedesco, M. et al. (2016). “The darkening of the Greenland ice sheet: trends, drivers, and projections (1981-2100)”. In: *The Cryosphere* 10.2, pp. 477–496.

Tedstone, A. J. et al. (2017). “Dark ice dynamics of the south-west Greenland Ice Sheet”. In: *The Cryosphere* 11.6, pp. 2491–2506.

Tegen, I. et al. (1997). “Contribution of different aerosol species to the global aerosol extinction optical thickness: Estimates from model results”. In: *Journal of Geophysical Research: Atmospheres* 102.D20, pp. 23895–23915.

Tiedtke, M. (1993). “Representation of clouds in large-scale models”. In: *Monthly Weather Review* 121.11, pp. 3040–3061.

Trenberth, K. E. et al. (2014). “Seasonal aspects of the recent pause in surface warming”. In: *Nature Climate Change* 4.10, p. 911.

Tsay, S.-C., K. Stamnes, and K. Jayaweera (1989). “Radiative energy budget in the cloudy and hazy Arctic”. In: *Journal of the atmospheric sciences* 46.7, pp. 1002–1018.

Undén, P. et al. (2002). *HIRLAM-5 scientific documentation*. Tech. rep.

Uppala, S. M. et al. (2005). “The ERA-40 re-analysis”. In: *Quarterly Journal of the Royal Meteorological Society: A journal of the atmospheric sciences, applied meteorology and physical oceanography* 131.612, pp. 2961–3012.

Van de Wal, R. et al. (2012). “Twenty-one years of mass balance observations along the K-transect, West Greenland”. In: *Earth System Science Data* 4.1, pp. 31–35.

Van de Wal, R. et al. (2005). “Surface mass-balance observations and automatic weather station data along a transect near Kangerlussuaq, West Greenland”. In: *Annals of Glaciology* 42, pp. 311–316.

Van den Broeke, M., C. J. P. P. Smeets, and R. S. W. van de Wal (2011). “The seasonal cycle and interannual variability of surface energy balance and melt in the ablation zone of the west Greenland ice sheet”. In: *The Cryosphere* 5.2, pp. 377–390.

Van den Broeke, M. et al. (2009). “Partitioning Recent Greenland Mass Loss”. In: *Science* 326.5955, pp. 984–986. arXiv: `arXiv:1011.1669v3`.

Van den Broeke, M. et al. (2016). “On the recent contribution of the Greenland ice sheet to sea level change”. In: *Cryosphere* 10.5, pp. 1933–1946.

Van den Broeke, M. et al. (2017). “Greenland Ice Sheet Surface Mass Loss: Recent Developments in Observation and Modeling”. In: *Current Climate Change Reports* 3.4, pp. 345–356.

Van Kampenhout, L. et al. (2019). “Regional grid refinement in an Earth system model: Impacts on the simulated Greenland surface mass balance”. In: *The Cryosphere* 13.6, pp. 1547–1564.

Van Tricht, K. et al. (2016). “Clouds enhance Greenland ice sheet meltwater runoff”. In: *Nature communications* 7, p. 10266.

Vionnet, V. et al. (2012). “The detailed snowpack scheme Crocus and its implementation in SURFEX v7.2”. In: *Geoscientific Model Development* 5.3, pp. 773–791.

Wahr, J., S. Swenson, and I. Velicogna (2006). “Accuracy of GRACE mass estimates”. In: *Geophysical Research Letters* 33.6.

Wang, W., C. S. Zender, and D. van As (2018). “Temporal Characteristics of Cloud Radiative Effects on the Greenland Ice Sheet: Discoveries From Multiyear Automatic Weather Station Measurements”. In: *Journal of Geophysical Research: Atmospheres* 123.20, pp. 11, 348–11, 361.

Wang, W. et al. (2016). “A Retrospective, Iterative, Geometry-Based (RIGB) tilt-correction method for radiation observed by automatic weather stations on snow-covered surfaces: application to Greenland”. In: *The Cryosphere* 10.2, pp. 727–741.

Wang, W. et al. (2019). “Spatial Distribution of Melt Season Cloud Radiative Effects Over Greenland: Evaluating Satellite Observations, Reanalyses, and Model Simulations Against In Situ Measurements”. In: *Journal of Geophysical Research: Atmospheres* 124.1, pp. 57–71.

Wang, X. and J. R. Key (2005). “Arctic surface, cloud, and radiation properties based on the AVHRR polar pathfinder dataset. Part I: Spatial and temporal characteristics”. In: *Journal of Climate* 18.14, pp. 2558–2574.

Warren, S. G. (1982). “Optical properties of snow”. In: *Reviews of Geophysics* 20.1, p. 67.

Winker, D. M., W. H. Hunt, and M. J. McGill (2007). “Initial performance assessment of CALIOP”. In: *Geophysical Research Letters*.

Wouters, B. et al. (2013). “Limits in detecting acceleration of ice sheet mass loss due to climate variability”. In: *Nature Geoscience* 6.8, pp. 613–616.

Wyard, C. et al. (2018). “Global Radiative Flux and Cloudiness Variability for the Period 1959–2010 in Belgium: A Comparison between Reanalyses and the Regional Climate Model MAR”. In: *Atmosphere* 9.7, p. 262.